ACCEPTED
FACULTY OF GRADUATE STUDIES

DEAN
DATE 9 Feb 94

SIGNAL PROCESSING TECHNIQUES FOR AIRBORNE LASER BATHYMETRY

by

HENRY WONG

B.A.Sc., University of Windsor, 1987

A DISSERTATION SUBMITTED IN PARTIAL FULFILLMENT OF THE
REQUIREMENTS FOR THE DEGREE OF

DOCTOR OF PHILOSOPHY

in the Department of
Electrical and Computer Engineering

We accept this dissertation as conforming
to the required standard

Dr. A. Antoniou, Supervisor, Dept. of Electrical and Computer Engineering

---

Dr. R. L. Kirlin, Departmental Member, Dept. of Electrical and Computer Engineering

---

Dr. W.-S. Lu, Departmental Member, Dept. of Electrical and Computer Engineering

---

Dr. M. Serra, Outside Member, Dept. of Computer Science

Mr. T. A. Curran, Additional Member, Institute of Ocean Sciences

---

Dr. J. F. R. Gower, External Examiner, Institute of Ocean Sciences

© HENRY WONG, 1993
UNIVERSITY OF VICTORIA

All rights reserved. This dissertation may not be reproduced in whole or in part, by mimeograph or other means, without the permission of the author.

Name HENRY WONG

Dissertation Abstracts International is arranged by broad, general subject categories. Please select the one subject which most nearly describes the content of your dissertation. Enter the corresponding four-digit code in the spaces provided.

ELECTRICAL ENGINEERING
SUBJECT TERM

0544
SUBJECT CODE

U·M·I

Subject Categories

THE HUMANITIES AND SOCIAL SCIENCES

COMMUNICATIONS AND THE ARTS
Architecture 0729
Art History 0377
Cinema 0900
Dance 0378
Fine Arts 0357
Information Science 0723
Journalism 0391
Library Science 0399
Mass Communications 0708
Music 0413
Speech Communication 0459
Theater 0465

EDUCATION
General 0515
Administration 0514
Adult and Continuing 0516
Agricultural 0517
Art 0273
Bilingual and Multicultural 0282
Business 0688
Community College 0275
Curriculum and Instruction 0727
Early Childhood 0518
Elementary 0524
Finance 0277
Guidance and Counseling 0519
Health 0680
Higher 0745
History of 0520
Home Economics 0278
Industrial 0521
Language and Literature 0279
Mathematics 0280
Music 0522
Philosophy of 0998
Physical 0523
Psychology 0525
Reading 0535
Religious 0527
Sciences 0714
Secondary 0533
Social Sciences 0534
Sociology of 0340
Special 0529
Teacher Training 0530
Technology 0710
Tests and Measurements 0288
Vocational 0747

LANGUAGE, LITERATURE AND LINGUISTICS
Language
- General 0679
- Ancient 0289
- Linguistics 0290
- Modern 0291

Literature
- General 0401
- Classical 0294
- Comparative 0295
- Medieval 0297
- Modern 0298
- African 0316
- American 0591
- Asian 0305
- Canadian (English) 0352
- Canadian (French) 0355
- English 0593
- Germanic 0311
- Latin American 0312
- Middle Eastern 0315
- Romance 0313
- Slavic and East European 0314

PHILOSOPHY, RELIGION AND THEOLOGY
Philosophy 0422
Religion
- General 0318
- Biblical Studies 0321
- Clergy 0319
- History of 0320
- Philosophy of 0322

Theology 0469

SOCIAL SCIENCES
American Studies 0323
Anthropology
- Archaeology 0324
- Cultural 0326
- Physical 0327

Business Administration
- General 0310
- Accounting 0272
- Banking 0770
- Management 0454
- Marketing 0338

Canadian Studies 0385
Economics
- General 0501
- Agricultural 0503
- Commerce-Business 0505
- Finance 0508
- History 0509
- Labor 0510
- Theory 0511

Folklore 0358
Geography 0366
Gerontology 0351
History
- General 0578
- Ancient 0579
- Medieval 0581
- Modern 0582
- Black 0328
- African 0331
- Asia, Australia and Oceania 0332
- Canadian 0334
- European 0335
- Latin American 0336
- Middle Eastern 0333
- United States 0337

History of Science 0585
Law 0398
Political Science
- General 0615
- International Law and Relations 0616
- Public Administration 0617

Recreation 0814
Social Work 0452
Sociology
- General 0626
- Criminology and Penology 0627
- Demography 0938
- Ethnic and Racial Studies 0631
- Individual and Family Studies 0628
- Industrial and Labor Relations 0629
- Public and Social Welfare 0630
- Social Structure and Development 0700
- Theory and Methods 0344

Transportation 0709
Urban and Regional Planning 0999
Women's Studies 0453

THE SCIENCES AND ENGINEERING

BIOLOGICAL SCIENCES
Agriculture
- General 0473
- Agronomy 0285
- Animal Culture and Nutrition 0475
- Animal Pathology 0476
- Food Science and Technology 0359
- Forestry and Wildlife 0478
- Plant Culture 0479
- Plant Pathology 0480
- Plant Physiology 0817
- Range Management 0777
- Wood Technology 0746

Biology
- General 0306
- Anatomy 0287
- Biostatistics 0308
- Botany 0309
- Cell 0379
- Ecology 0329
- Entomology 0353
- Genetics 0369
- Limnology 0793
- Microbiology 0410
- Molecular 0307
- Neuroscience 0317
- Oceanography 0416
- Physiology 0433
- Radiation 0821
- Veterinary Science 0778
- Zoology 0472

Biophysics
- General 0786
- Medical 0760

EARTH SCIENCES
Biogeochemistry 0425
Geochemistry 0996
Geodesy 0370
Geology 0372
Geophysics 0373
Hydrology 0388
Mineralogy 0411
Paleobotany 0345
Paleoecology 0426
Paleontology 0418
Paleozoology 0985
Palynology 0427
Physical Geography 0368
Physical Oceanography 0415

HEALTH AND ENVIRONMENTAL SCIENCES
Environmental Sciences 0768
Health Sciences
- General 0566
- Audiology 0300
- Chemotherapy 0992
- Dentistry 0567
- Education 0350
- Hospital Management 0769
- Human Development 0758
- Immunology 0982
- Medicine and Surgery 0564
- Mental Health 0347
- Nursing 0569
- Nutrition 0570
- Obstetrics and Gynecology 0380
- Occupational Health and Therapy 0354
- Ophthalmology 0381
- Pathology 0571
- Pharmacology 0419
- Pharmacy 0572
- Physical Therapy 0382
- Public Health 0573
- Radiology 0574
- Recreation 0575
- Speech Pathology 0460
- Toxicology 0383

Home Economics 0386

PHYSICAL SCIENCES
Pure Sciences
Chemistry
- General 0485
- Agricultural 0749
- Analytical 0486
- Biochemistry 0487
- Inorganic 0488
- Nuclear 0738
- Organic 0490
- Pharmaceutical 0491
- Physical 0494
- Polymer 0495
- Radiation 0754

Mathematics 0405
Physics
- General 0605
- Acoustics 0986
- Astronomy and Astrophysics 0606
- Atmospheric Science 0608
- Atomic 0748
- Electronics and Electricity 0607
- Elementary Particles and High Energy 0798
- Fluid and Plasma 0759
- Molecular 0609
- Nuclear 0610
- Optics 0752
- Radiation 0756
- Solid State 0611

Statistics 0463

Applied Sciences
Applied Mechanics 0346
Computer Science 0984
Engineering
- General 0537
- Aerospace 0538
- Agricultural 0539
- Automotive 0540
- Biomedical 0541
- Chemical 0542
- Civil 0543
- Electronics and Electrical 0544
- Heat and Thermodynamics 0348
- Hydraulic 0545
- Industrial 0546
- Marine 0547
- Materials Science 0794
- Mechanical 0548
- Metallurgy 0743
- Mining 0551
- Nuclear 0552
- Packaging 0549
- Petroleum 0765
- Sanitary and Municipal 0554
- System Science 0790

Geotechnology 0428
Operations Research 0796
Plastics Technology 0795
Textile Technology 0994

PSYCHOLOGY
General 0621
Behavioral 0384
Clinical 0622
Developmental 0620
Experimental 0623
Industrial 0624
Personality 0625
Physiological 0989
Psychobiology 0349
Psychometrics 0632
Social 0451

Supervisor: Professor A. Antoniou

ABSTRACT

Airborne laser bathymetry, a relatively new state-of-the-art technology for the mapping of sea depth by using active airborne laser ranging systems, has proved successful for charting shallow waters worldwide including Canada, Australia, and the United States. In order to improve the reliability and efficiency of using airborne laser ranging systems, in particular, the Canadian LARSEN 500 airborne system, for the estimation of sea depth, one- and two-dimensional (1-D and 2-D) signal processing algorithms are developed. The processing involved is carried out in a two-phased approach. In phase I, 1-D signal processing is explored. Specifically, 1-D digital smoothing is applied to the laser waveforms for noise reduction. Results show that this process can remove noise while preserving the important characteristics of the laser signal. In order to analyze the laser reflections quantitatively, a mathematical model function that can be used to characterize the smoothed laser waveforms received by the LARSEN 500 under diverse circumstances is established. Two algorithms are also developed for the detection of the peak of the laser pulse reflected from the sea surface and bottom. The algorithms have been implemented and tested extensively with real-world LARSEN waveforms. Tests show that the algorithms can reject noise pulses and pulses arising from turbid layers in the sea and locate the correct pulse in the presence of varying degrees of noise.

In order to separate the surface and bottom reflections independently of the degree of their overlap, a waveform-decomposition technique based on a robust optimization method is developed. An initialization scheme is also developed in conjunction with the decomposition technique which can reduce the amount of computation required in the decomposition quite significantly. Comparison results obtained from statistical analysis show that the proposed technique offers considerable potential in improving the depth estimates particularly when the resolution between the surface and bottom reflections is low. In addition, it can be used to automate the depth estimation process.

In phase II, 2-D signal processing is used to improve the reconstruction of ocean topography from individual depth estimates. A type of 2-D interpolating filter is introduced to suppress impulsive noise present in the scattered measurements. It is found that as a result of the filtering, the representation of the sea floor, which can be in the form of 2-D contour maps or 3-D surface plots, becomes a more accurate representation of the ocean bottom.

To improve the accuracy in the reconstruction, a sophisticated triangle-based 2-D interpolation technique designed using the finite-element method is applied. To increase the reliability of the reconstruction, optimal triangulated irregular networks are constructed before carrying out the interpolation. In order to assess the accuracy of the decomposition results when the resolution between the laser reflections is very low, a procedure which incorporates the 2-D interpolation technique is developed.

To further enhance the reconstructed profiles, an adaptive 2-D filtering procedure is introduced. This procedure is developed using 2-D power spectral analysis of the depth profiles. In areas where the signal characteristics of the bathymetric data vary rapidly, 2-D filtering based on minimum mean-squared error estimation is explored. It is shown that the derived filter is a 2-D space-variant filter and its application to bathymetric profiles collected by the LARSEN 500 system is also implemented. Results obtained show that these two filtering procedures are useful in reducing random noise inherent in the reconstructed profiles which is difficult to detect and eliminate in 1-D processing.

Dr. A. Antoniou, Supervisor, Dept. of Electrical and Computer Engineering

---

Dr. R. L. Kirlin, Departmental Member, Dept. of Electrical and Computer Engineering

---

Dr. W.-S. Lu, Departmental Member, Dept. of Electrical and Computer Engineering

---

Dr. M. Serra, Outside Member, Dept. of Computer Science

Mr. T. A. Curran, Additional Member, Institute of Ocean Sciences

---

Dr. J. F. R. Gower, External Examiner, Institute of Ocean Sciences

CONTENTS

LIST OF TABLES

LIST OF FIGURES

LIST OF ABBREVIATIONS

A/D	analog to digital
AL	attenuation length
CCRS	Canada Centre for Remote Sensing
CHS	Canadian Hydrographic Service
CPU	central processing unit
DFT	discrete Fourier transform
EMG	exponentially modified Gaussian function
FEM	finite-element method
FFT	fast Fourier transform
FIR	finite duration impulse response
IR	infrared
LIDAR	light detection and ranging
OSF	order-statistics filter
RMS	root mean square
SNR	signal-to-noise ratio
TIN	triangulated-irregular network
VLSI	very large scale integration

Acknowledgements

I wish to express my sincere gratitude to Dr. Andreas Antoniou for his guidance during the research and writing of this dissertation. Financial assistance received from Dr. Antoniou through Micronet, Networks of Centres of Excellence Program, and Natural Sciences and Engineering Research Council, Canada is gratefully acknowledged.

I am also grateful to Terra Surveys Ltd., B.C., Canada for supplying the LARSEN waveforms for this project. I wish to express my appreciation to Mr. Rick Quinn of Terra Surveys and Mr. Terry Curran of the Institute of Ocean Sciences in this regard.

To my wife Susan for her support and patience I am especially grateful.

To Susan

CHAPTER ONE
INTRODUCTION

Over the past fifty years, acoustic echo sounding has dominated the field of hydrography and, in particular, the field of bathymetry. The use of sound to measure water depth can be traced back to World War I [1]. One of the earliest instruments used for mapping ocean topography was the echo sounder [2]. The technology of the acoustic echo sounder has improved through the years with the introduction of more accurate and reliable equipment. Conventional echo sounding methods provide topographic data only along a single path directly beneath the track of the survey ship [3]. To achieve adequate bottom coverage, the side-scanning sonar and the multi-narrow-beam sonar methods were developed [4]. The side-scanning sonar method permits the measurement of the sea-bed topography for a wide area but the absolute depth cannot be measured. The multi-beam method has a narrower observation range but it permits measurement of the true depth. Sonar systems based on the methods mentioned above require surface vessels to carry them and thus the speed of acquisition of bathymetric data is limited by the speed of the vessels. Moreover, hydrographic survey ships cannot operate safely in shallow waters.

To increase the flexibility of operation and the rate of coverage of a given area, several remote-sensing techniques have been employed, for example, aerial photography [5] and satellite multi-spectral imaging [6]. Aerial photography has been tried with limited success since water depths exceeding 10 m are difficult to discern. In addition, the application of this technique is critically dependent on water clarity, sea state, and the amount of scattered solar radiation from either the sky or the sea. Multi-spectral imaging, though less affected by environmental variations than aerial photography, is capable of measuring depths only up to 20 m when the sky is free of clouds in the region of interest.

To increase the accuracy and depth measuring capability in shallow coastal waters, airborne laser ranging systems have been introduced. In airborne laser bathymetry, sea depth is measured using the light detection and ranging (LIDAR) system. In this system, a series of short intense pulses of blue-green laser light are projected from the aircraft into the ocean. The laser light is reflected back from the surface and bottom of the sea, and sea depth can be deduced from the time difference between the surface and bottom reflections. Backscattered radiation from the water column, carrying information on the degree of turbidity of the sea, is also received and can be analyzed.

The feasibility of using airborne laser techniques was first demonstrated with a system constructed at the Syracuse University Research Corporation in 1968 [7]. This system incorporated a pulsed blue-green laser and was carried on a Turbo-Commander aircraft. It measured depths of up to 8 m with an estimated accuracy of ± 0.5 m in Lake Ontario. The blue-green laser was chosen because the wavelengths involved permit adequate depth resolution and minimize absorption of laser light in coastal waters [8].

The first commercially built research system was the pulsed-light airborne depth sounder (PLADS) developed by Raytheon for the US Naval Oceanographic Office [9]. Flight tests were conducted over the Gulf of Mexico in 1972. During tests in turbid coastal waters with a beam attenuation length (AL) of 1 to 2 m, bottom profiles of up to 14 m were obtained. Attenuation length is a measure of water clarity and is defined as the depth over which the laser power is attenuated by a factor equal to the exponential constant e. A more recent development in the United States was an airborne oceanographic LIDAR system (AOL) built by Avco Everett Research Laboratory, Inc. for NASA [10]-[11]. The AOL is a spatially-scanning pulsed laser system which has two major areas of application, namely, airborne bathymetry and laser-induced fluorometry. As an airborne laser bathymetric system operating in turbid

waters with beam AL of 1 m, depth measurements of up to 10 m can be obtained. Another system in the United States, which is known as the airborne bathymetric survey (ABS) system, was developed by Naval Ocean Research and Development Activity (NORDA) [12]. This system combines two independent optical sensors, namely, a laser sounder and a multi-spectral scanner, into one integrated system.

In Australia, investigations into airborne laser hydrography began in 1972 by the Electronics Research Laboratory at Salisbury in response to a request from the Royal Australian Navy [13]. Initial research and development was carried out during 1974-1975 and an experimental system, the Weapons Research Establishment laser airborne depth sounder referred to as WRELADS I was built in 1976. In the following year, a series of flight trials were carried out in the waters of North Queensland including the Great Barrier reef. A maximum depth of 40 m was measured in clear waters with a diffuse AL of 10 m. The experimental nonscanning system WRELADS I was followed by the scanning system WRELADS II which not only provided positional information for the soundings but also navigational guidance for the pilot [14]. Results of the flight trials showed that water depths in the 2 to 30 m range can be measured with an accuracy of $\pm$ 1 m. A more recent development in Australia is the laser airborne depth sounder (LADS) [15]. New features in this system include the use of an all-digital airborne data acquisition system and the doubling of the laser pulse rate to 168 pulses per second.

In Canada, the use of airborne laser methods in the field of hydrography was initiated by the development of the MK I low-power neon laser bathymeter. Testing of the MK I over Kingston Harbour in Lake Ontario was carried out by the Canada Centre for Remote Sensing (CCRS) in 1976 [16]. A second generation of the system, MK II, is a nonscanning LIDAR system and initially served as a complement to aerial and satellite remote sensing techniques [17]. Results obtained from the Magdalen

Islands flight trials showed that in turbid waters with beam AL of 1.4 m, depths in the range of 0.6 to 20 m were recorded. In order to increase speed, extent of coverage and flexibility, a more advanced system, the LARSEN 500, was developed by CCRS and the Canadian Hydrographic Service (CHS) [18]-[20]. This is an advanced airborne scanning LIDAR system designed to measure water depths in shallow coastal waters and meets the standards of CHS. The LARSEN 500 can measure depths from 1.5 to 40 m to an accuracy of 0.3 m. Several flight tests of the system began in 1984 over numerous areas such as the Ottawa River, Lake Ontario, Lake Huron and Cambridge Bay [18]. In the Cambridge Bay area, water depths in the range of 35 to 40 m were measured with beam AL of 3.3 m. A maximum water depth of 10 m was measured in the highly turbid waters of the Ottawa River and more than 20 m was measured in the less turbid waters of Lake Huron (beam AL = 0.75 to 1 m). The concept and operation of this system is briefly described in the next section.

1.1 CONCEPT AND OPERATION

The laser-beam geometry for the LARSEN 500 is illustrated in Fig. 1.1 and the principles of operation are as follows. Blue-green and infrared (IR) laser pulses are projected simultaneously from the aircraft into the ocean in a quasi-circular fashion. The IR pulse is scattered by the water surface whereas the blue-green pulse is reflected back from the surface, the water column, as well as the bottom of the ocean. The surface echo is much stronger than the bottom return since signal attenuation in water is much stronger than in air. Two separate optical channels are used to detect and process the received IR and blue-green signals [21]. In the IR optical channel, a synthetic pulse is generated when the IR reflection is received in the aircraft. This pulse is combined with the output of the blue-green optical channel to yield a LARSEN waveform. This waveform is sampled at 2-ns intervals and 256 consecutive samples are digitized to 6-bit accuracy, and are then recorded. Fig. 1.2 illustrates a typical LARSEN waveform.

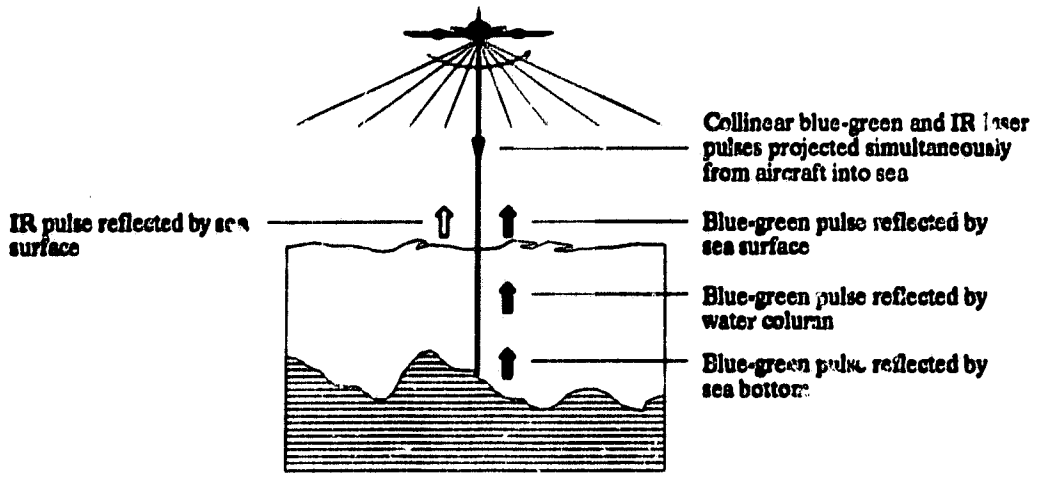

Fig. 1.1 Laser-beam geometry for the LARSEN 500.

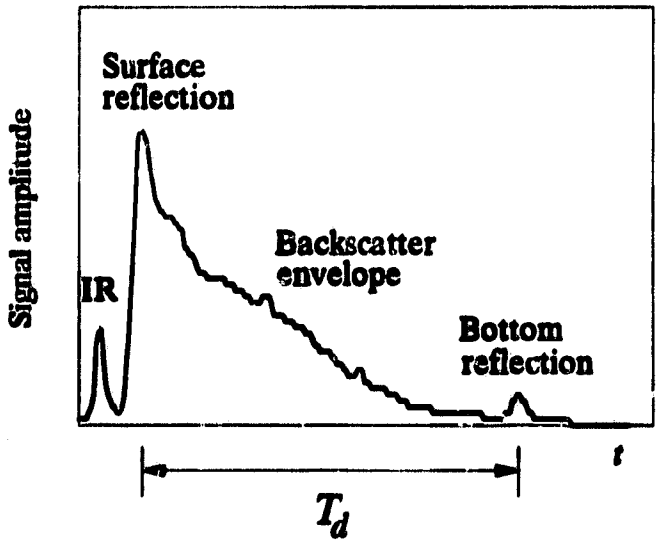

Fig. 1.2 A typical LARSEN waveform.

In Fig. 1.2, we note that a fixed amount of delay is introduced between the IR synthetic pulse and the blue-green signals to prevent their overlap. The IR pulse serves as a surface marker [21] and is used with the blue-green bottom return to estimate sea depths. However, when ocean and weather conditions are unfavorable, the IR reflection may not be received and, as a result, the synthetic pulse may be absent from the waveforms. Sea depth can be estimated by measuring the time delay between the blue-green surface and bottom reflections by using the relation

$$\text{depth} = \frac{T_d c}{2r}$$

where T_d is the time interval between the peaks of the blue-green surface and bottom reflections, c is the speed of light in air, and r is the refractive index of sea water.

The shape of the waveform varies dramatically depending on sea depth and sea turbidity. Other major factors that influence depth soundings are the shape and texture of the sea bottom, sea-surface roughness, and the angle of the laser beam with respect to the sea surface [14]. A selection of waveforms is shown in Fig. 1.3.

The quasi-circular scanning performed by the LARSEN 500 system is generated by a scanning depth sounder which produces a swath of 270 m wide and a uniform sounding density on a grid spacing of 35 m with a positioning accuracy of about 15 m. The system performs a circular scan across the track as it moves along the track. It is designed to produce a regular pattern of depth soundings on the surface of the sea as shown in Fig. 1.4. Each arc shown in the figure consists of nine laser soundings or nine blue-green laser pulses.

1.2 PROBLEMS ENCOUNTERED

Water quality is an important factor in the depth penetration of a laser pulse as it affects the range and accuracy of depth measurement. As absorption and scattering of laser light are very strong in water [22],

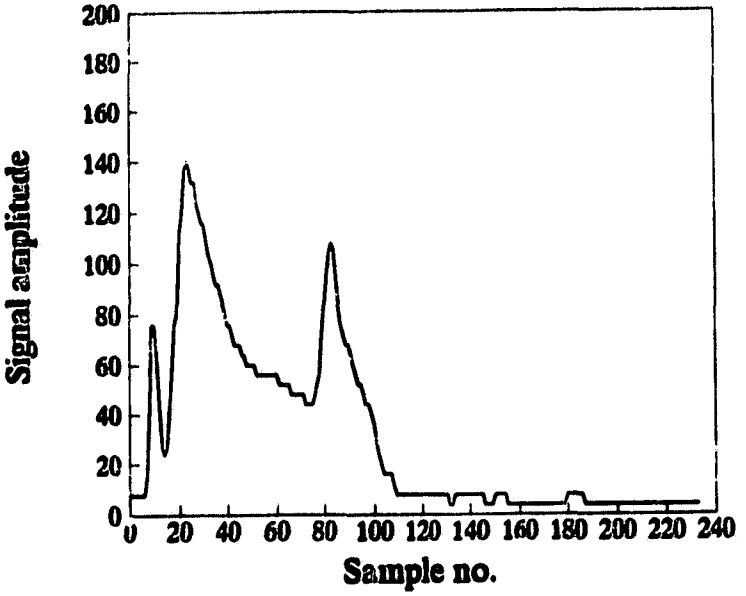

(a)

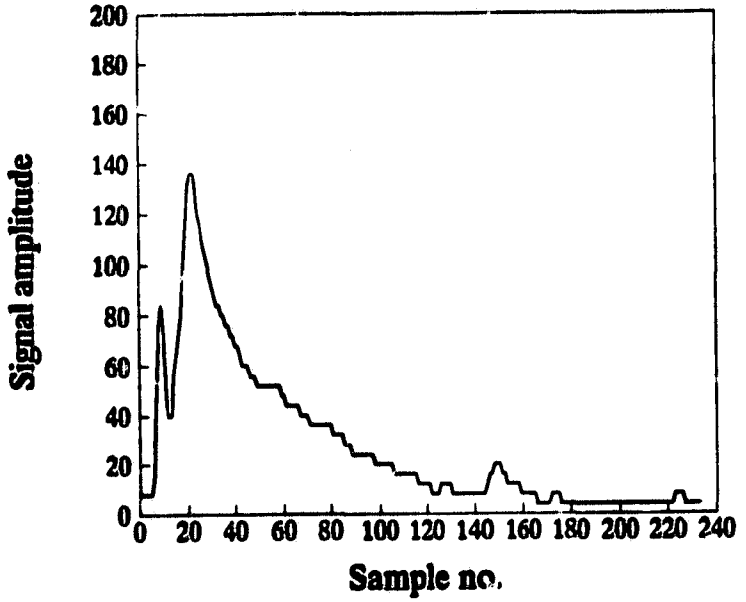

(b)

Fig. 1.3 Waveforms received in different situations: (a) moderate depth, clear water; (b) deep water, weak bottom reflection in noise.

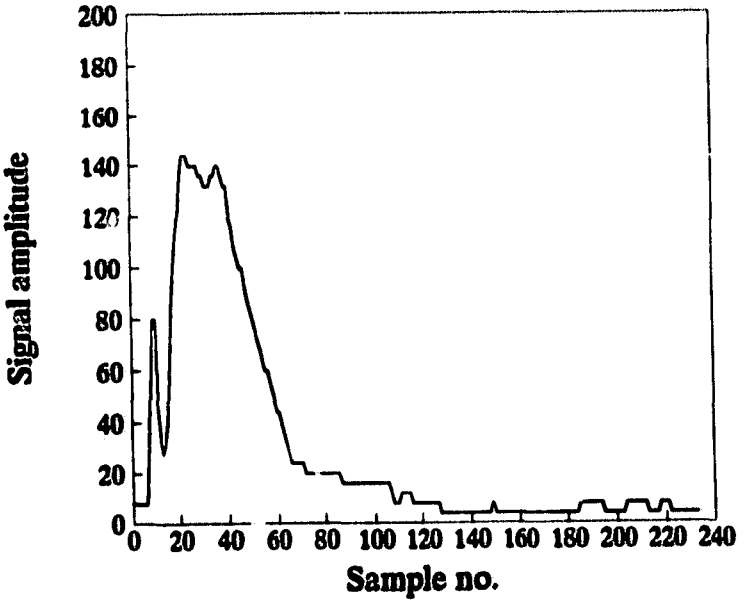

(c)

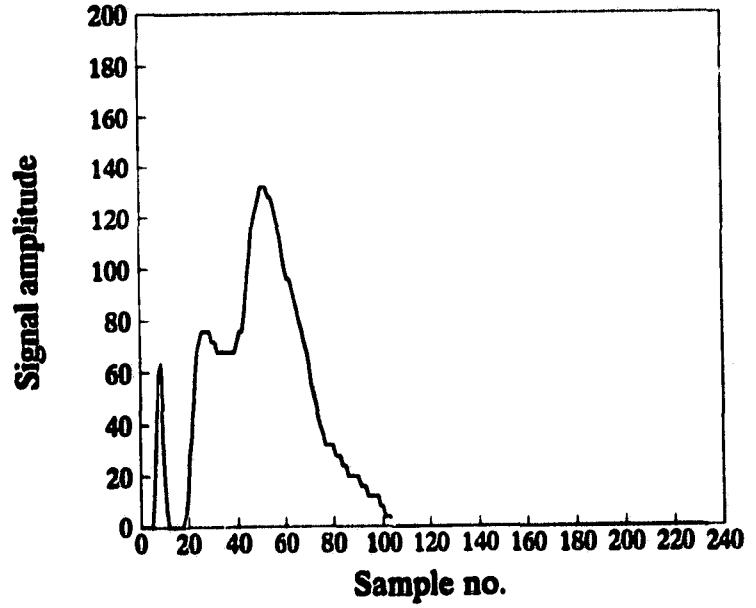

(d)

Fig. 1.3 Waveforms received in different situations: (c) very shallow water, strong bottom reflection; (d) shallow water, weak blue-green surface reflection.

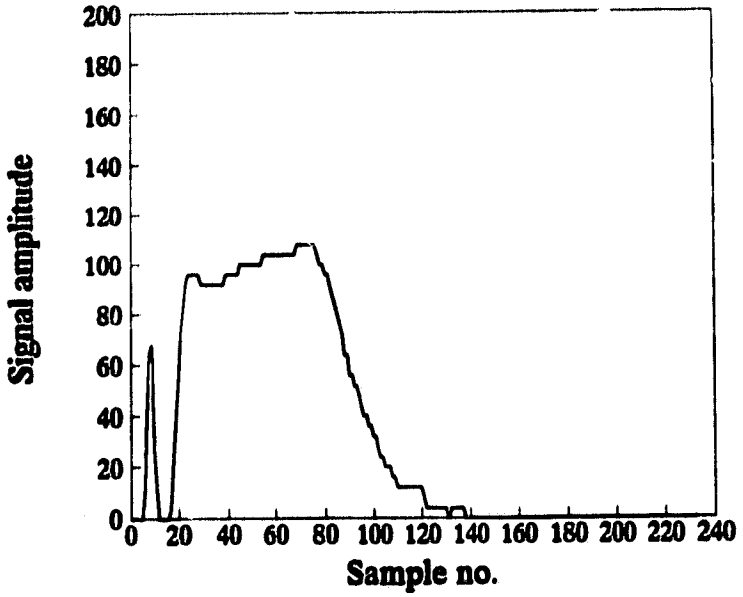

(e)

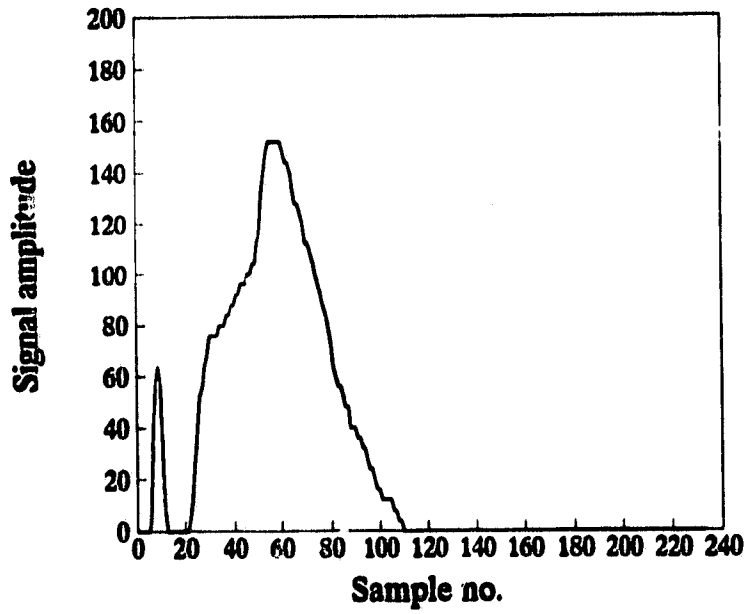

(f)

Fig. 1.3 Waveforms received in different situations: (e) shallow turbid water, turbid layers near sea surface; (f) shallow turbid water, turbid layers near sea bottom.

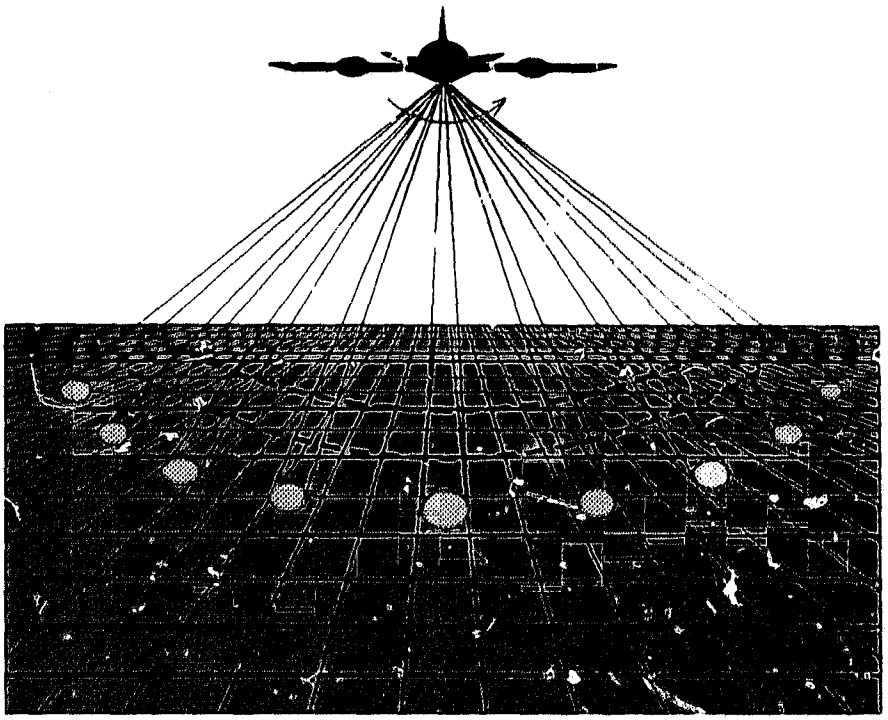

Fig. 1.4 Sounding pattern for the LARSEN 500.

particle content strongly influences the attenuation introduced. This problem is particularly serious in coastal waters, which are prime areas for laser bathymetry, since microscopic marine life is abundant in these areas. Backscatter from suspended and dissolved particles in water tends to weaken the laser-signal reflections from the sea bottom [23] whereas scattering by particles causes spatial spreading of the laser beam [24]. These effects can influence the determination of the sea depth quite significantly.

In general, different concentrations of turbid layers throughout the water column can cause different levels of beam dispersion. Minimal dispersion occurs when the concentration of turbid layers is near the sea bottom. On the other hand, dispersion is maximum when turbid layers is highly concentrated near the sea surface [25]. Besides the turbid layers in the water column, dispersion of the beam also increases with increasing depth. Dispersion tends to enlarge the footprint of the beam on the sea bottom. Different sea bottom compositions due to rocks, sea grass, bushes etc., can broaden the reflected pulse thereby influencing the estimation of the depth. Furthermore, the accuracy of depth measurement may also be affected by dense bottom vegetation, resulting in shallow depth estimates [5].

As mentioned, each waveform consists of signal reflections including a surface reflection, a volumetric backscatter from the water, and a weak bottom return. When the blue-green laser pulse travels in a water column of uniform turbidity, the backscattered energy decays exponentially with increasing depth [23]. By contrast, if the turbidity of the water column is nonuniform, distorted backscatter envelopes are obtained which have spurious peaks. Fig. 1.5 is an example of this type of waveform. Other factors that can degrade the accuracy of depth measurement include the noise generated by the electronic equipment in the aircraft such as the laser-pulse receiving system, and noise due to ambient light. Under daytime operation, radiation scattered from the sun and sky at the water surface can saturate the detector and increase the background DC noise level [26] thereby distorting the depth estimation.

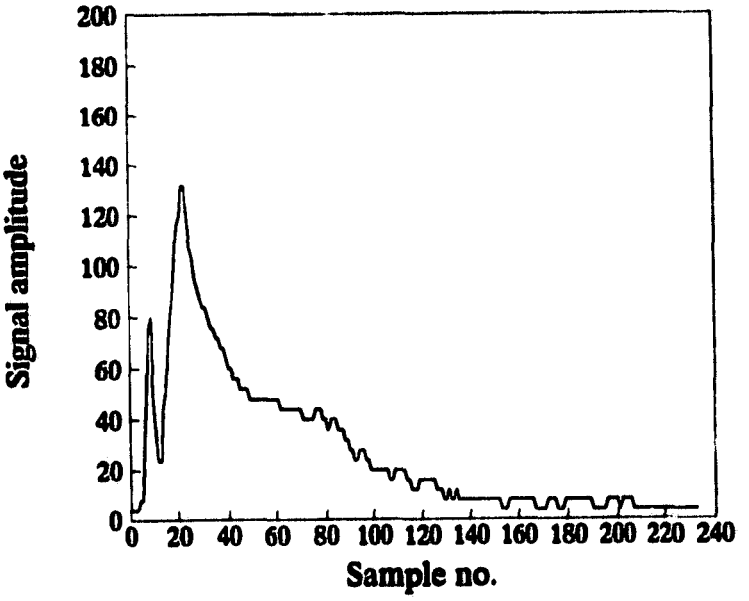

Fig. 1.5 Waveform corrupted by noise.

To enhance the sea-depth estimation process, a number of data processing techniques have been proposed in recent years. In [27], a waveform processing algorithm was described. The algorithm was developed using heuristic rules to identify surface and bottom reflections from the received waveforms. These rules involve the use of amplitude and rise-time information of the received reflections to minimize the effects of spurious signals and noise. Sea depths are estimated by using a type of threshold detector. In [28], an algorithm was proposed in which the detection of the bottom reflection in the received waveforms involves (1) the use of a highpass filter to remove low-frequency components in the received waveforms, (2) the computation of a quantity known as pulse confidence for every possible bottom return in the filtered waveform, and (3) the identification of the two pulses with the highest pulse confidence for further processing.

1.3 SCOPE OF THESIS

The objectives of the thesis are to explore the use of signal processing to (1) improve the accuracy of sea-depth estimation, (2) automate the estimation process, and (3) improve the representation of sea-bed topography in the form of 2-D contour maps and 3-D surface plots for perspective displays. To achieve these objectives, one- and two-dimensional (1-D and 2-D) digital signal processing algorithms are developed for the processing of the LARSEN waveforms in a two-phased approach. In phase I, 1-D processing algorithms are developed to process each LARSEN waveform individually to obtain the best estimates of sea-depth measurement. The depth estimates obtained in phase I are then improved further in phase II by using 2-D digital signal processing algorithms.

Chapter 2 describes a set of signal processing algorithms that can be used to preprocess the received waveforms in order to facilitate automatic sea-depth estimation. First, laser reflections received from the ocean are interpreted in terms of their moments. On the basis of this interpretation, the

application of a special class of digital smoothing filters to laser reflections for noise reduction is explored. A mathematical model function that can be used to characterize the smoothed LARSEN waveforms received under diverse circumstances is next established. With the use of this model function, two algorithms are then developed to detect the peak of the surface and bottom reflections in the waveforms. In laser bathymetry, the surface peak is usually strong but the bottom peak is difficult to identify in many cases. In order to test the performance of the bottom-peak detection algorithm under different noise and resolution conditions, simulation studies are carried out.

Sea depths estimated from the peak positions in the waveforms may be affected depending on the resolution of laser reflections in the waveform. To address the problem of resolution directly, a waveform-decomposition procedure is developed in Chapter 3 to resolve laser waveforms into separate signal components which represent the surface and bottom reflections. The procedure also includes an initialization scheme which is developed for improving the efficiency of the decomposition process, based on the results obtained from the algorithms in Chapter 2.

Depth estimates obtained through waveform decomposition are compared with corresponding estimates obtained by a local surveying company using state-of-the-art techniques. To gain insight into the depth estimation process, the comparison results are analyzed with respect to different ranges of sea depth and different ranges of resolution between laser reflections.

The depths estimated by the methods described are represented on a two-dimensional surface forming a 2-D depth profile. To improve the representation of sea bed, a type of 2-D interpolating filter is introduced in Chapter 4 to filter rogue measurements in the scattered data. A sophisticated 2-D interpolation technique is then applied to reconstruct the sea-bed topography from the processed scattered measurements. Next, through the incorporation of this interpolation technique, a procedure

is designed to assess the 1-D processing results when the resolution between the laser reflections is very low.

To enhance the reconstructed profiles, an adaptive 2-D filtering procedure which involves 2-D power spectral analysis is developed in Chapter 5. This procedure is designed to be adapted to the signal in each region of the profile on the basis of the distribution of signal power in the frequency domain. In this chapter, the application of estimation theory for the enhancement of laser bathymetric profiles is also explored. Results show that the 2-D signal processing involved can enhance the laser bathymetric profiles, thereby improving measurement accuracy in laser bathymetry.

Conclusions and directions for further research are found in Chapter 6.

CHAPTER TWO
SMOOTHING, CHARACTERIZATION, AND DETECTION OF LASER REFLECTIONS

2.1 INTRODUCTION

Noise embedded in laser waveforms can degrade the depth-measurement accuracy. In order to minimize the noise present while preserving the information content of the original signal as far as possible, a special class of smoothing digital filters is employed to preprocess the waveforms. In this chapter, we discuss the properties of these filters and illustrate their application to the LARSEN waveforms.

Sea depth is estimated by measuring the time delay between the water surface and sea bed returns. Although less than 5 % of the signal is reflected back from the water surface to the receiver [5], the bottom reflection is considerably weaker than the surface reflection because of the exponential attenuation of light in water [8]. Consequently, the detection of the surface peak is relatively simple whereas the detection of the bottom peak requires more detailed analysis of the shape of the waveform. Physical characterization of the preprocessed waveforms by specially selected mathematical functions is, therefore, first studied. An algorithm designed for the detection of the surface peak is then presented. Finally, an algorithm for the elimination of sharp spikes and high-frequency noise and the detection of the peak in the bottom reflection is presented.

2.2 DIGITAL SMOOTHING OF LASER SIGNALS

In laser bathymetry, the temporal position of the reflected laser pulses in the received waveforms is used to provide sea-depth information. Accurate estimation of the temporal position of these pulses is, therefore, necessary. Unfortunately, noise embedded in the laser waveforms, which may originate from a variety of sources such as the electronic equipment of the receiving system and the A/D quantization

process, may modify the position of the laser pulses and, therefore, can cause inaccuracies in the sea-depth estimates. Standard lowpass filtering can remove noise in the high-frequency band but it may also deform the information content of the signal if its spectrum extends into the high-frequency band. Our objective in this section is to discuss a smoothing process that can remove noise while preserving the information content of the signal up to a desired degree. To help understand such a smoothing process, we first represent a signal $f(t)$, which may represent a laser reflection from the sea, in terms of its moments. We then describe a type of smoothing digital filter that can preserve these moments up to a desired order while removing wideband noise.

2.2.1 Moment representation of signals

Assume that a signal $f(t)$ of unknown form is a piecewise-continuous, bounded function, which can be expressed in terms of a series of Hermite polynomials as

$$f(t) = \sum_{m=0}^{\infty} A_m H_m(t) \tag{2.1}$$

where $H_m(t)$ represents the Hermite polynomial of order m and

$$A_m = \frac{1}{2^m m! \sqrt{\pi}} \int_{-\infty}^{\infty} e^{-t^2} f(t) H_m(t)\, dt \tag{2.2}$$

represents its coefficient. Polynomials $H_m(t)$ for $m = 0, 1, 2, \ldots$ form an othogonal set of functions with respect to e^{-t^2} and the expression for these polynomials can be found in [29].

Coefficient A_m in Eq. (2.2) can be expressed in terms of the moments of $f(t)$ [30]. By doing this, $f(t)$ in Eq. (2.1) can be rewritten as

$$f(t) = \sum_{m=0}^{\infty} \phi_m(t) H_m\left(\frac{t - m_1}{\sqrt{\mu_2}}\right) \tag{2.3}$$

where

$$\phi_m(t) = G(t)\frac{c_m}{m!} \tag{2.4}$$

and

$$G(t) = \frac{1}{\sqrt{2\pi\mu_2}} \exp\left[\frac{-(t-m_1)^2}{2\mu_2}\right] \tag{2.5}$$

The quantities m_1 and μ_2 are the normalized first moment and normalized second central moment of $f(t)$, respectively. Except for the first three constants c_0, c_1, and c_2, the values of c_m in Eq. (2.4) are obtained from the central moments of $f(t)$. They are given by

$$c_0 = 1, \qquad c_1 = c_2 = 0, \qquad c_3 = \frac{\mu_3}{\mu_2^{3/2}}, \qquad c_4 = \frac{\mu_4}{\mu_2^2} - 3 \tag{2.6}$$

where c_3 and c_4 are the skew and excess of $f(t)$, respectively. Other values of c_m can be found in [30]. Note that each c_m is a function of the central moments of $f(t)$ which are of order m at most.

From Eqs. (2.3) to (2.6), we note that signal $f(t)$ can be completely described by its moments. Therefore, if we can preserve the moments of $f(t)$, we can preserve the information content of $f(t)$.

If the laser reflections in the waveforms are interpreted as distribution curves of photons received at each specific instant of time, then the moment representation just mentioned can be related to the important physical features of the laser reflections. For example, the first normalized moment, i.e., the mean m_1, refers to the peak position of a symmetric laser reflection. The second normalized moment, i.e., the variance μ_2, provides an indication of the width of the reflection. The skew provides a measure of the degree of asymmetry or tailing of the reflection, and the excess denotes the sharpness of the return pulse. Our requirement in smoothing is to remove noise while preserving the moments, and hence the physical features, of the signal. In this way, the structural parameters estimated from the waveform

become more precise and, therefore, can enhance the results of a number of depth-estimation algorithms including the waveform decomposition that will be discussed in Chapter 3.

2.2.2 Signal enhancement by preserving moments

The signals obtained in airborne laser bathymetry are discrete-time sequences. Suppose that we have a discrete-time signal $f(n)$ corrupted by white Gaussian noise $w(n)$ with zero mean and variance σ_w^2. The observed signal is given by

$$x(n) = f(n) + w(n)$$

where n is the sampling index. We wish to determine $f(n)$ from $x(n)$ using a linear discrete-time system in such a way that $w(n)$ can be reduced while minimizing the distortion of $f(n)$. If $y(n)$ is the response of the discrete-time system, it can be written as

$$y(n) = y_f(n) + e_w(n) \tag{2.7}$$

where $y_f(n)$ and $e_w(n)$ are components of $y(n)$ due to $f(n)$ and $w(n)$, respectively, as shown schematically in Fig. 2.1. From Eq. (2.7), the output sequence $y(n)$ can also be written as

$$\begin{aligned} y(n) &= f(n) + e_f(n) + e_w(n) \\ &= f(n) + e(n) \end{aligned}$$

where $e_f(n)$ is the error signal, $e_w(n)$ is the error due to white noise, and $e(n) = e_f(n) + e_w(n)$ is the total error.

There are many types of processing that can be used in the estimation of $f(n)$. In our case, we reduce $e_f(n)$ by preserving the moments of $f(n)$ up to a desired order, say L, i.e.,

$$M_l[y_f(n)] = M_l[f(n)], \qquad l = 0, 1, 2, \ldots, L \tag{2.8}$$

where $M_l[\cdot]$ denotes the lth moment in the discrete-time domain. We minimize $e_w(n)$ by minimizing its variance, namely, $\sigma_w^2(n)$.

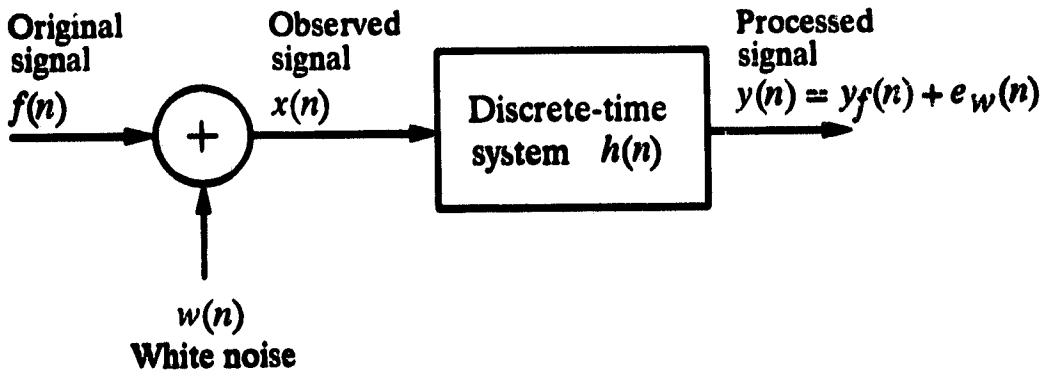

Fig. 2.1 Block diagram of discrete-time system.

A discrete-time system that yields minimum $\sigma_w^2(n)$ while satisfying Eq. (2.8) is described in [31]. This system is in the form of a finite-duration impulse response (FIR) zero-phase digital filter; the impulse response of such a filter is obtained by minimizing E_h, the energy in $h(n)$, such that

$$M_0[h(n)] = 1 \qquad \text{and} \qquad M_l[h(n)] = 0, \quad l = 1, 2, ..., L \tag{2.9}$$

When L is large, i.e., when the highest-order moment to be preserved is large, highly-detailed original signal components can be preserved at the expense of having only a small amount of noise reduction. On the other hand, when L is small or when only the fundamental features of the signal need to be preserved, noise reduction can be significant. In the processing of the LARSEN waveforms, we find that the peak position, pulse width, and the degree of tailing or skew of the laser reflections are important quantities to be preserved as they are useful not only in sea-depth estimation, but also, as will be discussed in Section 2.4 and Chapter 3, in examining the sensitivity of the sea-depth estimates to the shape of the reflections. In view of this, L was chosen to be 3.

The determination of $h(n)$ such that requirement in Eq. (2.9) is satisfied is described in detail in [31]. For the case $L = 3$, $h(n)$ can be expressed as

$$h(n) = 3\,\frac{(3K^2 + 3K - 1 - 5n^2)}{(2K-1)(2K+1)(2K+3)}, \qquad |n| \le K$$

where $2K$ is the order of the filter. For a 12th-order digital filter ($K = 6$), the impulse response is obtained as

$$h(n) = \frac{1}{143}\{-11, 0, 9, 16, 21, 24, 25, 24, 21, 16, 9, 0, -11\}$$

Extensive experimentation has shown that a filter order of 12 yields a good estimation of $f(n)$ in conjunction with excellent noise reduction. Higher filter orders can lead to more noise reduction but the improvement is not commensurate with the increase in computational complexity or cost of hardware required.

Fig. 2.2 shows typical received LARSEN waveforms and Fig. 2.3 shows the corresponding processed waveforms. By comparing the smoothed waveforms with the original waveforms, we find that the peaks of the laser reflections become more well-defined after the reduction in background noise, as illustrated in Fig. 2.3(a), (b), and (c) and, in general, the physical structure of the waveforms is preserved. Fig. 2.3(b) shows that the general shape of the bottom reflection is maintained after smoothing even when the bottom return is very weak. Fig. 2.2(c) shows that the bottom reflection lies very close to the surface reflection. After smoothing, the peak of the bottom return continues to be consistent with the one in the original waveform but with the background noise removed, as depicted in Fig. 2.3(c). We conclude, therefore, that preprocessing by an FIR filter of the type described can bring about a significant improvement in the sea-depth estimation.

2.3 CHARACTERIZATION OF WAVEFORMS

The reflections of the laser pulse from the sea can be analyzed quantitatively by representing the received waveforms by mathematical functions. The purpose here is to reduce a complicated process that depends on many parameters to a simpler one involving a small number of parameters. This data reduction requires approximation and, therefore, some degree of error may be involved. However, if the characterization of the waveforms facilitates the data processing and, further, if the parameters of the functions turn out to be physically meaningful, then by understanding the influence of each parameter, one can gain insight into the behavior of the process.

In characterizing the LARSEN waveforms, we have three requirements in the formulation of the mathematical functions. They include (1) mathematical functions should not be limited to characterizing waveforms received from specific areas of the sea with specific optical characteristics, (2) mathematical

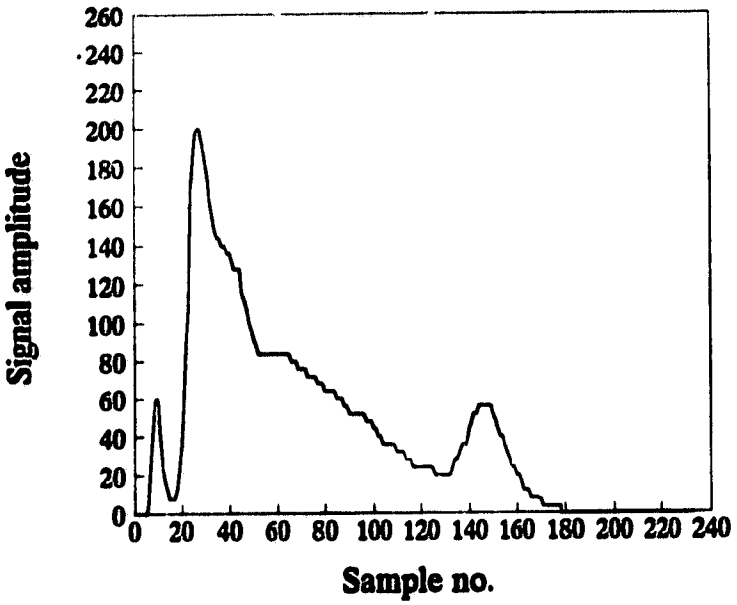

(a)

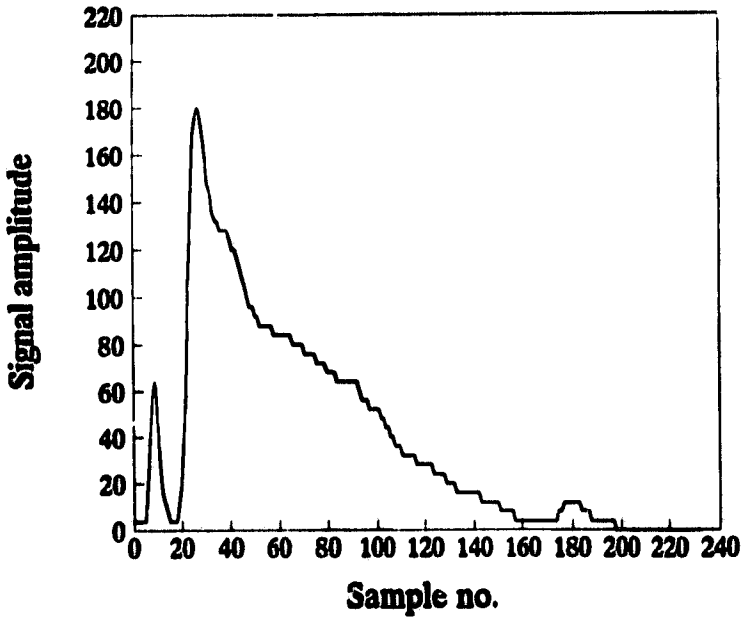

(b)

Fig. 2.2 Raw LARSEN waveforms received in different situations: (a) moderate depth; (b) deep water, weak bottom reflection buried in noise.

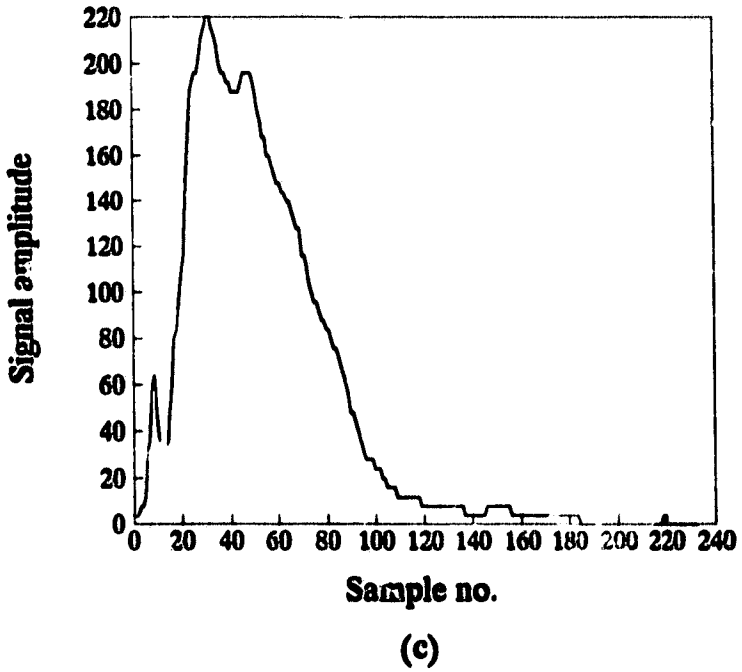

Fig. 2.2 Raw LARSEN waveforms received in different situations: (c) very shallow water, strong bottom reflection.

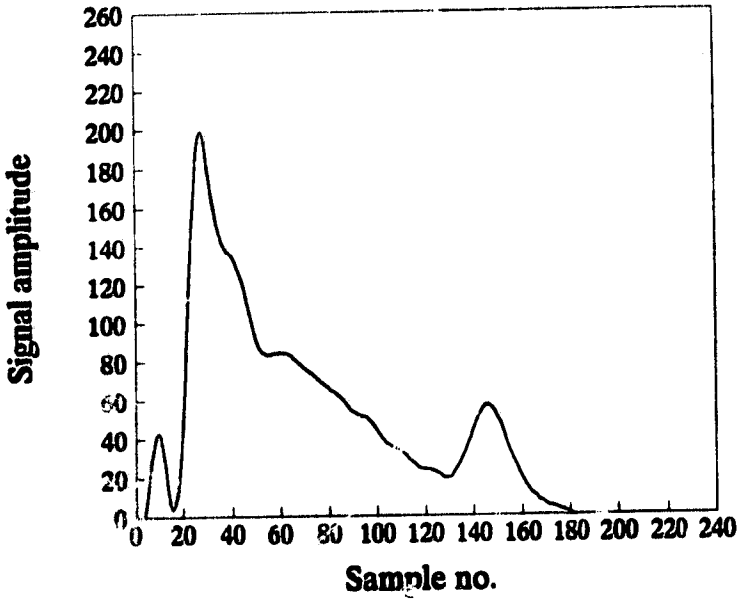

(a)

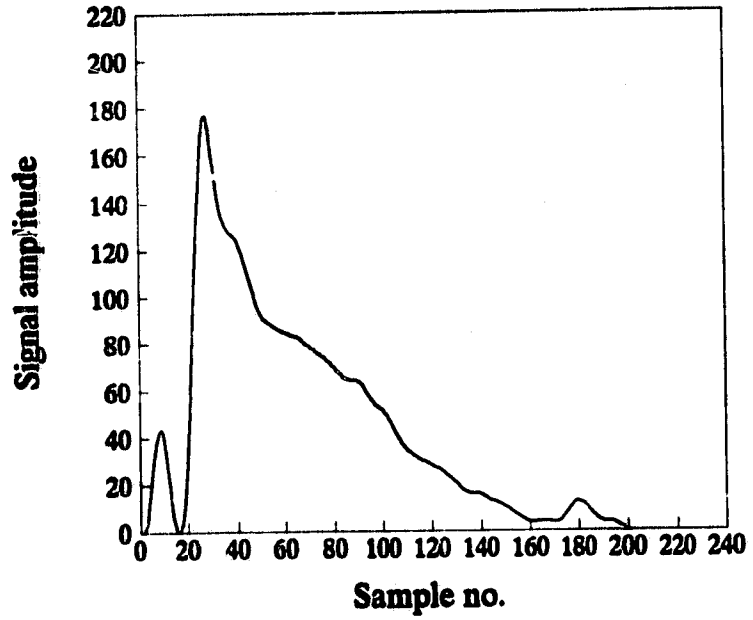

(b)

Fig. 2.3 Smoothed versions of LARSEN waveforms shown in Fig. 2.2(a) and (b).

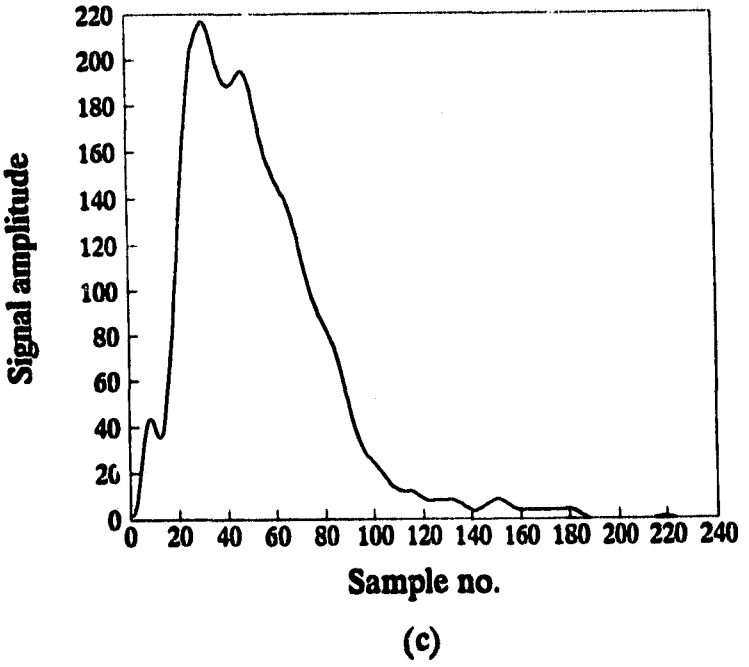

(c)

Fig. 2.3 Smoothed version of LARSEN waveform shown in Fig. 2.2(c).

functions can be obtained either analytically or numerically, and (3) since this is a data reduction process, the total number of parameters in the mathematical functions should be kept small.

At the outset, we preprocess the raw LARSEN waveforms by the digital smoothing filter as discussed in Section 2.2 to remove noise. Specially selected mathematical functions are then used to characterize the smoothed waveforms. In this analysis, we assume that atmospheric effects on the laser pulse are negligible. This assumption is valid since the atmospheric temporal dispersion of the pulse is small and its intensity is only slightly reduced when compared to that of the transmitted pulse [32].

2.3.1 Characterization of surface reflection

In this section, we refer to the combined effects of the laser backscatter from the sea surface and the laser backscatter from the water column as the surface reflection. The first component is primarily affected by the ocean surface reflectance, the field of view of the receiver, the scan angle of the laser beam off nadir, etc. A detailed discussion of the effects of these factors on backscatter can be found in [33]. The second component, on the other hand, depends on the optical characteristics and depth of the sea. A theoretical study of laser light backscattered from water ranging from clear to turbid is given in [23] and an experimental study of this subject is described in [34]. Below, we attempt to characterize the physical structure of the surface reflection in terms of mathematical functions.

We assume throughout that the turbidity of the water column is uniform. In such a case, the backscattered energy from the water column tends to decay exponentially and, therefore, causes the trailing edge of the reflected pulse to become asymmetrical. A mathematical function that was found to model the effect of turbidity well is the exponentially modified Gaussian (EMG) function. This function can yield a large variety of asymmetrical profiles that resemble the surface reflections contained in the LARSEN waveforms.

The EMG function is obtained via the convolution of the standard Gaussian function and an exponential decay function and is given by

$$y_{EMG}(t) = f_1(t) * f_2(t)$$

where

$$f_1(t) = h_G \exp\left[-(t - t_G)^2 / 2\sigma_G^2\right]$$

is the Gaussian function

$$f_2(t) = \frac{1}{\tau} e^{-t/\tau} u(t)$$

is the exponential decay function, and $u(t)$ is the unit-step function

$$u(t) = \begin{cases} 1 & \text{for } t \geq 0 \\ 0 & \text{otherwise} \end{cases}$$

The convolution of $f_1(t)$ and $f_2(t)$ is given by the integral

$$y_{EMG}(t) = \frac{h_G}{\tau} \int_0^\infty e^{-v/\tau} \exp\left\{-\left[(t - t_G) - v\right]^2 / 2\sigma_G^2\right\} dv \qquad (2.10)$$

Eq. (2.10) shows that the EMG function $y_{EMG}(t)$ depends on four parameters: the function amplitude h_G, the time of maximum amplitude t_G, and the standard deviation σ_G of the parent Gaussian function, and the time constant τ of the exponential decay function.

To reduce the complexity of the expression, we normalize the function by introducing the variable

$$T = \frac{(t - t_G)}{\sigma_G}$$

which measures the time t in units of the standard deviation σ_G and defines the ratio

$$S_\tau = \frac{\sigma_G}{\tau} \qquad (2.11)$$

which determines the shape of the function.

By introducing a new variable

$$\xi = \frac{v}{\sigma_G} + S_\tau - T \tag{2.12}$$

the EMG function can be rewritten as

$$y_{EMG}(t) = h_G S_\tau e^{-T^2/2} e^{(S_\tau - T)^2/2} \int_{(S_\tau - T)}^{\infty} e^{-\xi^2/2} d\xi$$

In order to retain the original Gaussian function as a factor in the EMG function, a modifying function $f(x)$ will be introduced. It is convenient to formulate the argument of this function as

$$x = S_\tau - T$$

so that

$$y_{EMG}(t) = h_G f(x) e^{-T^2/2}$$

where

$$\begin{aligned} f(x) &= S_\tau e^{x^2/2} \int_x^{\infty} e^{-\xi^2/2} d\xi \\ &= S_\tau p(x) \end{aligned}$$

with

$$p(x) = e^{x^2/2} \int_x^{\infty} e^{-\xi^2/2} d\xi \tag{2.13}$$

In order to ease the computation of Eq. (2.13), we can relate $p(x)$ to the error function to carry out the computation. Results have shown, however, that when x is very small ($x < -13$) floating-point overflow may occur in the computation in computers whose dynamic range is 10^{-38} to 10^{38}. Since x decreases with increasing T and a large T arises from a situation when the tail of the reflected pulse from the water column is long, overflow is not uncommon in situations where the ocean depth is large.

To avoid overflow errors in the computation of the EMG function, an alternate method is investigated. On separating the exponential term in $p(x)$ in Eq. (2.13) from the normal probability integral and replacing x by $-z$, we get

$$y_{EMG}(t) = \sqrt{2\pi}\, h_G\, e^{(S_\tau^2/2 - TS_\tau)}\, S_\tau I \tag{2.14}$$

where

$$I = \int_{-\infty}^{z} \frac{e^{-\xi^2/2}}{\sqrt{2\pi}}\, d\xi$$

$$z = T - S_\tau$$

and ξ is defined in Eq. (2.12).

The integral I in Eq. (2.14) can be approximated by a polynomial expression [35] as

$$I = \begin{cases} A(z)B(q) & \text{for } z \le 0 \\ 1 - A(z)B(q) & \text{for } z > 0 \end{cases}$$

where

$$A(z) = \frac{1}{\sqrt{2\pi}} e^{-z^2/2}$$

$$B(q) = \sum_{i=1}^{5} b_i q^i$$

$$q = \frac{1}{1 + p|z|}$$

and $p, b_1, \ldots, b_5$ are the constants given in Table 2.1. The method used here for the evaluation of the EMG function has been found to be accurate and reliable in describing actual field data from a variety of different areas.

TABLE 2.1
CONSTANTS IN THE POLYNOMIAL APPROXIMATION FOR I IN EQ. (2.14).

p	= 0.231642	b_3	= 1.78148
b_1	= 0.319382	b_4	= -1.82126
b_2	= -0.356564	b_5	= 1.33027

If we want to determine the asymmetry of the EMG function, it is important to use the ratio S_τ in Eq. (2.11) rather than the absolute values of σ_G and τ. Fig. 2.4 shows the shape of different EMG functions with various values of S_τ. As can be seen from the figure, a decrease in S_τ causes an increase in the asymmetry of the pulse. On the other hand, when S_τ becomes very large, the EMG function will assume the shape of the Gaussian function. By varying the four parameters (h_G, t_G, σ_G, and τ) of the EMG function, we can force the amplitude, peak position, width, and asymmetry of the profile to resemble the surface reflections collected by the LARSEN 500 system from different areas of the sea.

2.3.2 Characterization of bottom reflection

The bottom reflection is affected by a number of major factors such as sea turbidity, bottom reflectivity, sea state and sea depth. Different sea bottom compositions due to rocks and sea grass can broaden the reflected pulse significantly while the dispersion effects of laser pulse in water may skew the bottom reflection. In order to solve the resolution problem described in Section 1.2 while satisfying the three requirements listed at the beginning of Section 2.3, we characterize the bottom reflection in the LARSEN waveforms using the Gaussian function. This function is given by

$$y_G(t) = A_{max} \exp\left[-(t - t_{max})^2 / 2\sigma^2\right] \tag{2.15}$$

where A_{max} is the maximum amplitude of the Gaussian function, t_{max} is the position at which the maximum amplitude occurs, and σ is the standard deviation. We use this function because its three parameters can be adjusted to quantify different amplitudes, peak positions, and widths of the profile. Here, we have neglected the dispersion effects which may skew the bottom reflection. However, one might use a more general function, like the EMG function discussed in Section 2.3.1, in order to take care of the asymmetry of the profile.

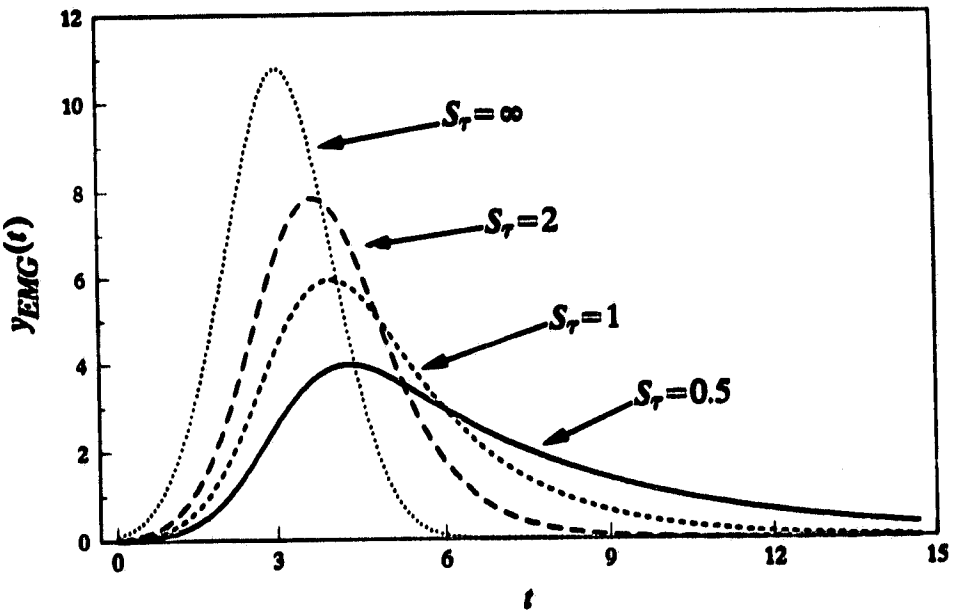

Fig. 2.4 Shape of $y_{EMG}(t)$ as a function of parameter S_τ.

Two reasons for our choice of the Gaussian function are as follows. When the bottom reflection has an asymmetrical profile, the peak position of the skewed bottom reflection is sensitive to two things according to [36]: (1) the dispersion effects of laser pulse and (2) the angle at which the laser pulse penetrates the sea. Specifically, an increase in dispersion causes a shift of the peak position to the left resulting in a smaller depth estimate; and an increase in the penetration angle causes a shift of the peak position to the right resulting in a larger depth estimate. The use of the symmetrical Gaussian function in Eq. (2.15) is analogous to assuming that, on the average, the depth bias due to the use of the peak position to estimate sea depths is small. Our second reason for choosing the Gaussian function is that it is relatively well-behaved mathematically. Moreover, its analytical representation reduces the computational complexity and increases the efficiency of sea depth estimation.

2.3.3 Analysis of simulated waveforms

We now wish to simulate the LARSEN waveforms represented by the function $y_T(t)$ which is formed by overlapping the EMG curve in Eq. (2.14) with the Gaussian curve in Eq. (2.15), namely,

$$y_T(t) = y_{EMG}(t) + y_G(t) \tag{2.16}$$

As the ratio S_T determines the asymmetry of the EMG function, we would like to investigate the effect of this ratio on the shape of $y_T(t)$. As can be seen in Fig. 2.5(a), for sufficiently small values of S_T, the two peaks cannot be distinguished. In this respect, a decrease in S_T has a similar effect as a decrease in peak separation. For a constant S_T, the loss of resolution between two peaks is most pronounced when the trailing peak is relatively weak as shown in Fig. 2.5(b). This figure shows the effect of different pulse widths of the bottom reflection on the overall simulated waveform. We see that when the bottom reflection is broadened to a certain degree, it is totally embedded in the surface reflection and, as a result, the sea depth information is lost. Loss of resolution between two peaks may also occur

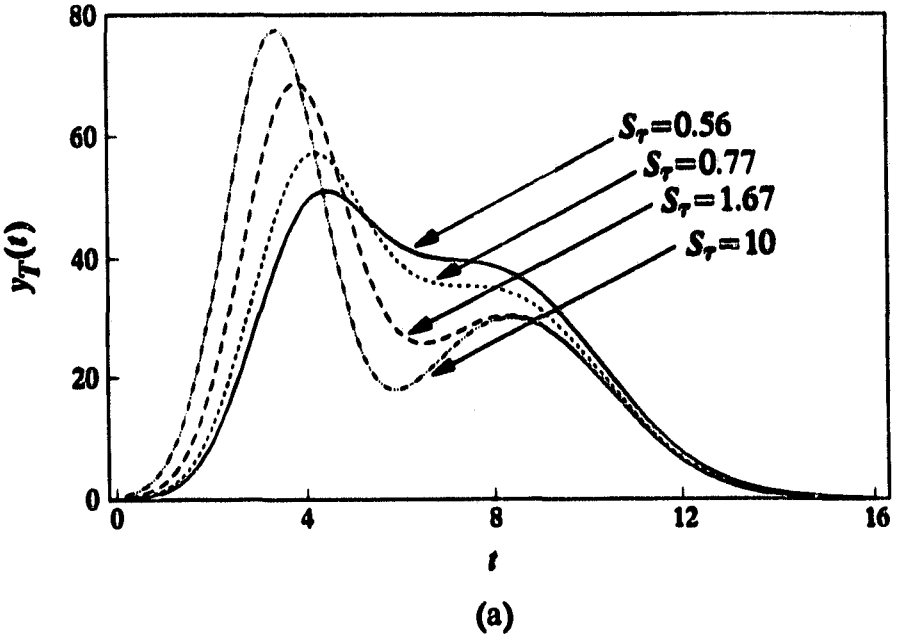

(a)

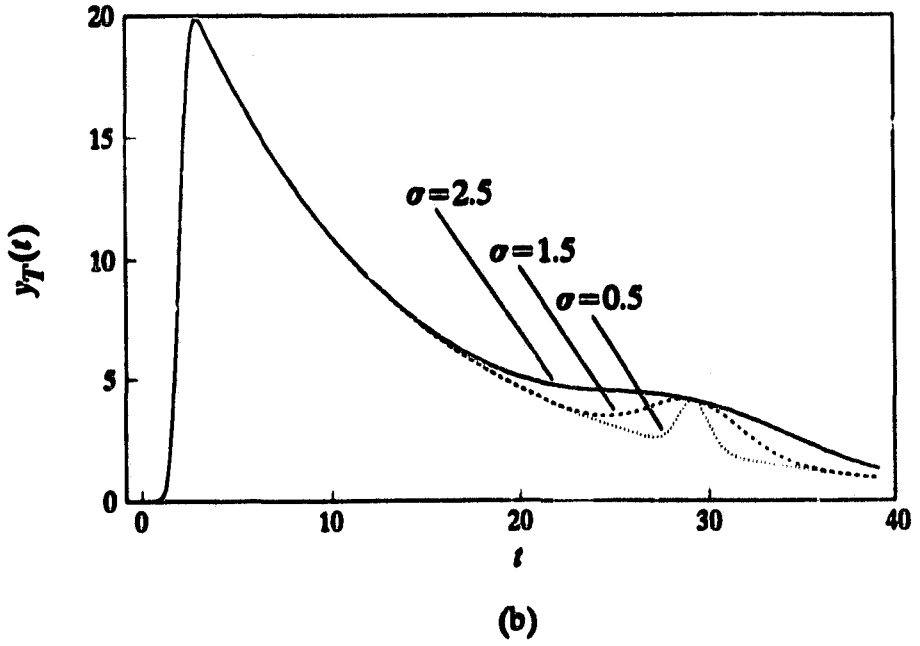

(b)

Fig. 2.5 Shape of $y_T(t)$ as a function of (a) parameter S_r; (b) parameter σ.

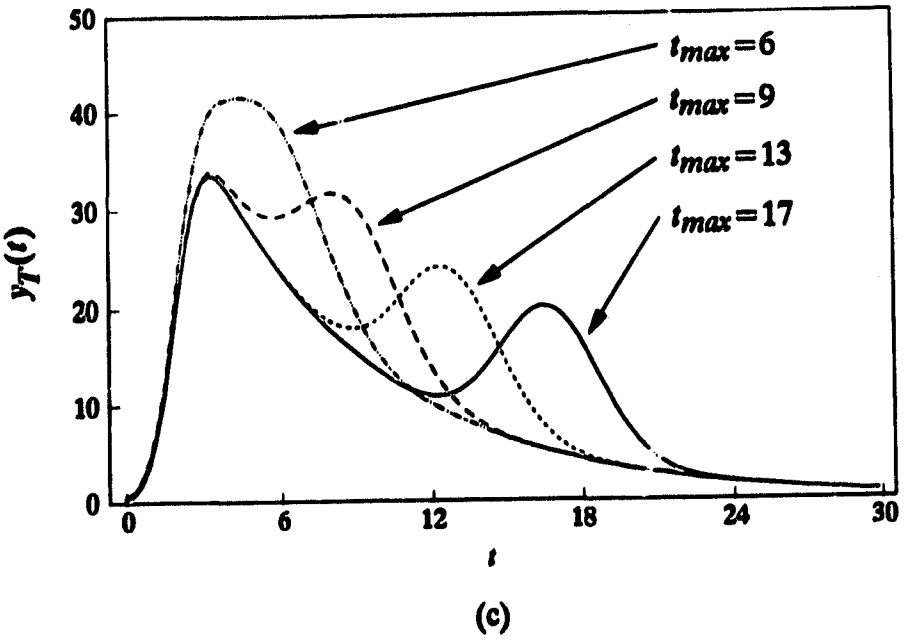

(c)

Fig. 2.5 Shape of $y_T(t)$ as a function of (c) parameter t_{max}.

in the case of a stronger trailing peak. This behavior is shown in Fig. 2.5(c) which depicts the change in the waveform shape for different peak separations. At smaller peak separations, the component peaks may overlap to such an extent that two peaks are fused into one. In physical situations, this occurs when the laser pulse is reflected from shoals or areas close to the shoreline where the sea water is very shallow.

2.4 PEAK DETECTION

This section describes the algorithms developed for the detection of the blue-green surface and bottom peaks in a waveform. The detection of the blue-green surface peak is essential for sea-depth estimation if the IR pulse is not received by the system. Even though the IR pulse is received, the detection of the surface peak is still necessary to provide structural information to waveform decomposition in order to extract the bottom return from the waveform, as will be discussed in Chapter 3. A simple algorithm for surface-peak detection is described in Section 2.4.1. Section 2.4.2 provides an algorithm for the detection of the bottom peak. With a reasonable knowledge of the bottom-peak position, efficient waveform decomposition can be achieved which results in accurate sea-depth estimation. Alternatively, the algorithm can be used for the direct estimation of sea depth when efficiency rather than accuracy is preferred.

2.4.1 Detection of surface peak

Surface peaks are relatively strong in the LARSEN waveforms in most cases and, therefore, their detection is quite simple.

To initialize the search for the surface peak, a search range called *surface zone* is set up in the waveform. The surface zone is the particular part of each waveform where the surface peak is expected to occur and is illustrated in Fig. 2.6. The *peak zone* is the region where the amplitude of the laser signal

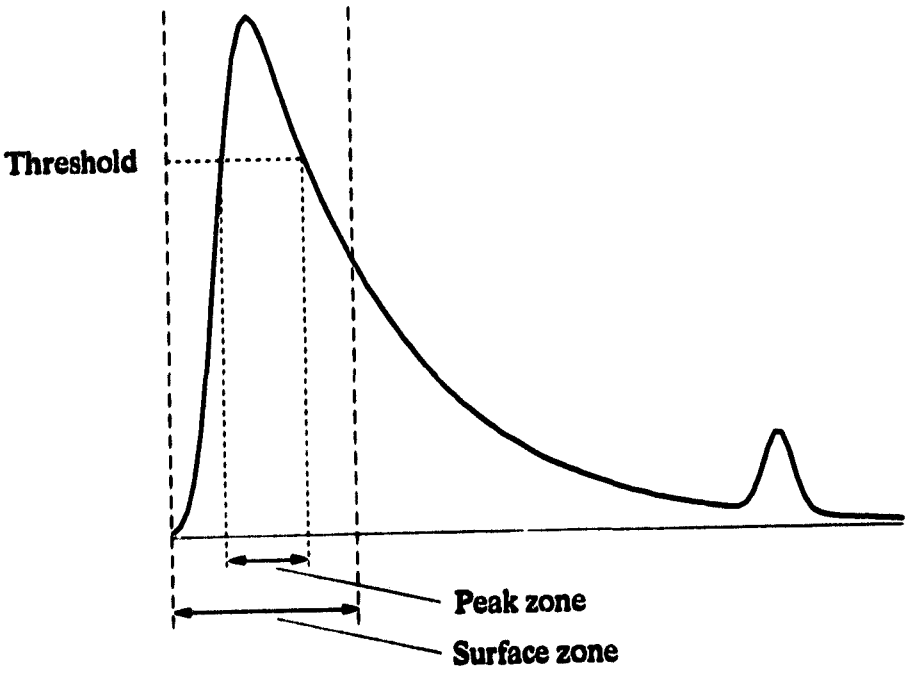

Fig. 2.6 Definition of surface zone and peak zone.

is greater than a specified threshold value as illustrated in Fig. 2.6. In every waveform, the surface zone is fixed while the peak zone is variable. It is possible to have no peak zone and this occurs when no surface return is detected by the receiver. On the other hand, two peak zones can be present in the surface zone and this can occur when the sea water is shallow. Sometimes it is possible to have both surface and bottom peaks in one peak zone. This usually happens when the water depth is between 2 to 4 m. The algorithm developed to detect the surface peak can also detect the bottom peak when it is situated in or next to the boundary of the surface zone. Once the bottom peak is identified, it can be used to confirm the result obtained in Section 2.4.2. The following is a brief description of the algorithm.

The algorithm first checks if there is any peak zone in the surface zone. If the algorithm finds a peak zone, it will continue to search for a second peak zone. After the ranges of the peak zones have been defined, the algorithm proceeds to search for the surface and bottom peaks.

The first peak in the first peak zone is always identified as the surface peak. If there is a second peak in the first peak zone, it will be identified as the bottom peak. If there is no second peak zone in the waveform, the algorithm ends and outputs the results. If a second peak zone is present, the maximum peak found in this zone is identified as the bottom peak and overrides the bottom peak found earlier in the first peak zone. A pseudo-code for the implementation of this algorithm is given in Appendix A-1.

2.4.2 Detection of bottom peak

In this section, we present a simple algorithm that incorporates a lowpass digital differentiation technique that can be used to locate the bottom peak position in the received waveforms. The function of lowpass differentiation is twofold: (1) to obtain the first derivative of the raw signal received, and (2) to eliminate spurious spikes and high-frequency noise components in the signal. It is important to note

that the noise-reduction process described here serves a different purpose from that described in Section 2.2. In Section 2.2, we reduce irregularities and retain the physical structure of the whole waveform so that waveform decomposition can be applied to the smoothed waveform; in this section, we concentrate on the detection of the bottom reflection by filtering the waveform based on the spectral content of the bottom reflection.

A Lowpass Digital Differentiation

The bottom return appears as a pulse in the waveform. To estimate its peak position, we can compute the first derivative of the laser signal and calculate the zero-crossing position. However, reflections from turbid layers may also appear as pulses in the waveform. As a result, we may find multiple zero crossings in the differentiated signal. Our objective is to construct an algorithm that identifies the zero crossing corresponding to the bottom peak. In order to do this, we first need to examine the characteristics of the pulses in the waveform.

Like other researchers [37], we find that the reflections from turbid layers usually appear as broader pulses when compared with the pulse arising from the sea bottom. As a result, the rate of change of signal intensity is not as high as that belonging to the bottom reflection. Since the first derivative provides the rate of change of the signal, we can design an algorithm based on the differentiated signal to discriminate against any reflections from turbid layers and detect the bottom reflection. In Fig. 2.7, we illustrate that when a pulse $f(t)$ is differentiated, the derivative $f'(t)$ reaches its peaks (both positive and negative) when $f(t)$ is at its inflection points. In the case where the change in signal intensity at the edges is rapid, as in the bottom return pulse, $|f'(t)|$ is large. Based on these observations, we expect the differentiated signal to contain a number of local maxima and minima and each extremum has a different magnitude depending on the slope at the corresponding inflection point.

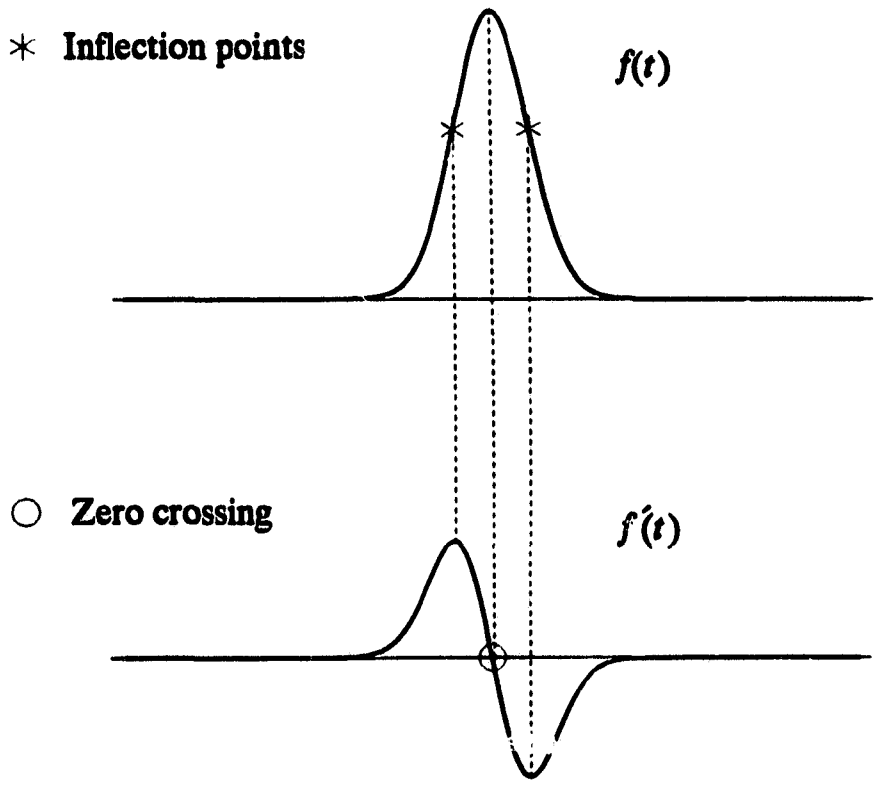

Fig. 2.7 A reflection pulse $f(t)$ and its derivative.

In order to utilize this information to detect the correct pulse, i.e., the one that corresponds to the bottom reflection, we analyze the differentiated signal further.

Depending on the water quality and depth of the sea, the volume backscatter in the received waveform may overlap with the bottom reflection. This situation arises occasionally when the water is not clear and the sea is not deep. The effect of overlap on the bottom reflection is illustrated in Fig. 2.8 where the bottom pulse is approximated by a Gaussian function and the volume backscattered envelope is represented by an exponential decaying function. In this illustration, we can make two interesting observations. First, the apparent bottom reflection is shifted to the left and, therefore, the corresponding zero crossing does not represent the true bottom-peak position. As a result, the accuracy of the sea-depth measurement is affected. Second, we observe that the rate of change of signal intensity at the leading edge of the bottom pulse is reduced somewhat by the overlap. Consequently, the size of the local maximum in the differentiated signal is reduced.

Our peak-location process involves two parts. The first part is concerned with the selection of the appropriate zero crossing and the second part deals with the location of the bottom peak according to the selected zero crossing. To select the desired zero crossing, the algorithm initially searches for a local maximum in the differentiated waveform starting from the location of the peak of the surface reflection. If a local maximum is found, the algorithm continues to search for the local minimum immediately next to it. The algorithm records the locations of these extrema and continues to search for another pair. Only one pair of extrema locations is preserved, namely, the one that corresponds the global minimum so far. The zero crossing located within this pair represents the desired zero crossing. A pseudo-code for the implementation of this algorithm is given in Appendix A-2.

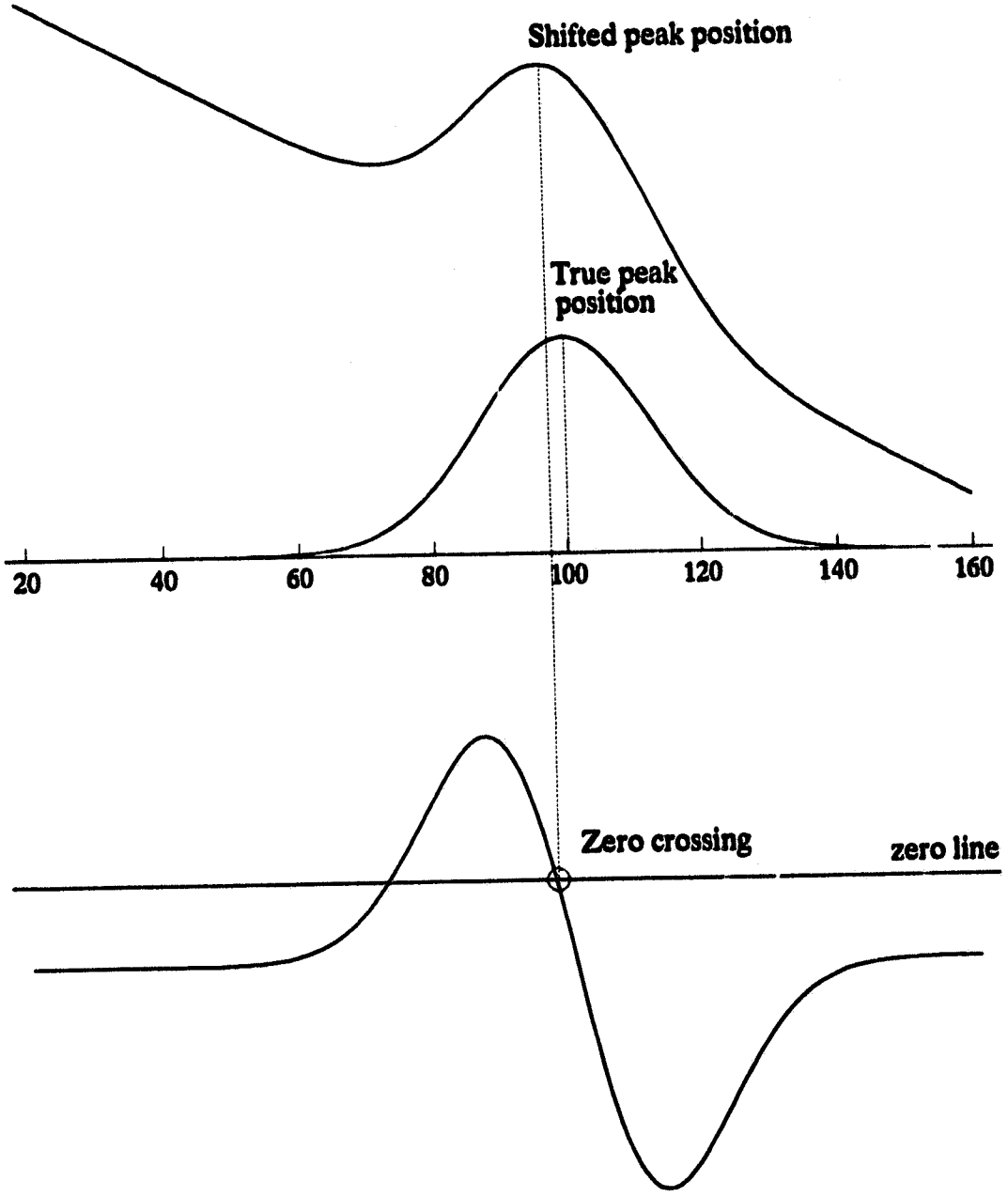

Fig. 2.8 Shift of peak position due to overlapped with exponential decaying curve.

A simple method to reduce the problem with the shifting of the zero crossing in $f'(t)$ is to use the average of the positions of the selected maximum and minimum to approximate the true bottom-peak position. Let $f(t)$ be the bottom return, $k(t)$ be the water-column backscattered signal, and $y(t)$ be the sum of these two signals. If $k(t)$ is approximated by a linear function, i.e., $k(t) = rt + c$, where $r < 0$ and $c > 0$, and $f(t)$ is approximated by a symmetric function such as a Gaussian function, then

$$y(t) = f(t) + rt + c$$

and

$$y'(t) = f'(t) + r \tag{2.17}$$

Assuming that r does not offset $f'(t)$ to the extent that a local maximum no longer exists, Eq. (2.17) implies that the positions of the extrema in $y'(t)$ are identical to those in $f'(t)$ and the effect of the overlap between the backscattered envelope and the bottom reflection can be compensated.

B. Design of Lowpass Digital Differentiator

The ideal amplitude response of a lowpass differentiator is shown in Fig. 2.9. The *x-axis* variable ν shown represents the normalized frequency which is defined as $\nu = \omega T/\pi$ where ω is the frequency in rad/s and T is the sampling period in s; parameter ν_c is the normalized cutoff frequency. The value of ν_c defines the maximum frequency at which the filter operates as a differentiator and frequency components higher than ν_c will be suppressed.

Our goal is to determine an optimal ν_c such that reflections from the sea bottom are correctly differentiated while spurious spikes and high-frequency noise are suppressed. As a first step, we need to investigate the spectral content of the bottom reflection.

In Section 2.3.2, we characterize the bottom reflection as a Gaussian function as expressed in Eq. (2.15). The discrete-time nature of the signals requires $y_G(t)$ in Eq. (2.15) to be represented as

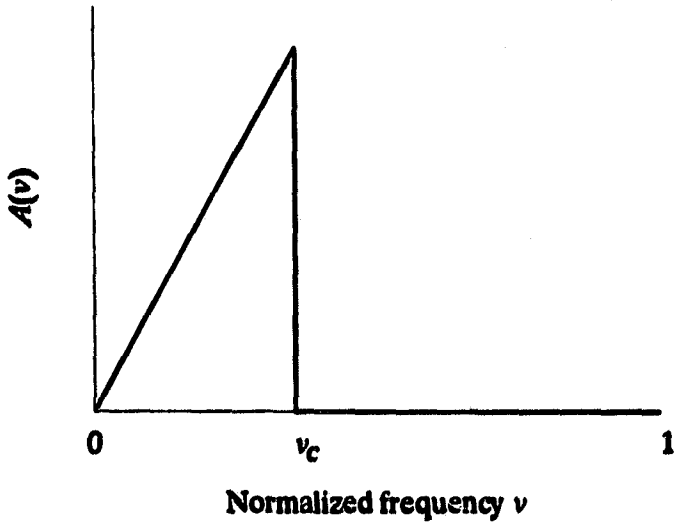

Fig. 2.9 Amplitude response of ideal lowpass differentiator.

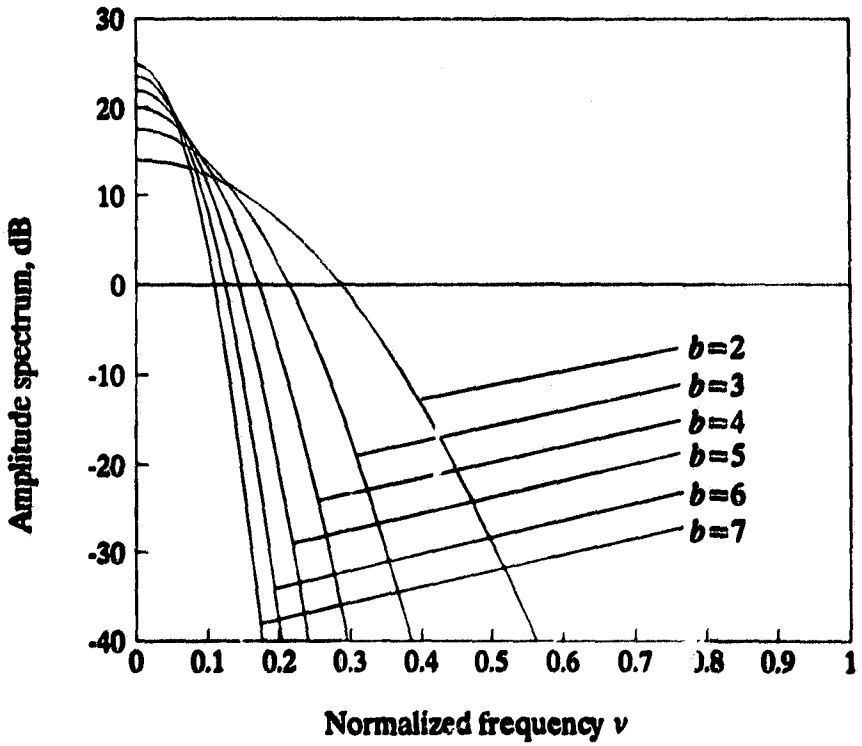

Fig. 2.10 A family of amplitude spectra of Gaussian pulses for various values of b.

$$y_G(n) = A_{max} \exp\left(\frac{-(n-n_{max})^2}{2b^2}\right) \tag{2.18}$$

where

$$n_{max} = \frac{t_{max}}{T}, \qquad b = \frac{\sigma}{T}$$

n is the sampling index, and T is the sampling period. The discrete-time Fourier transform of $y_G(n)$ is given by

$$Y_G(\omega) = b\sqrt{2\pi} \exp\left(\frac{-b^2T^2\omega^2}{2}\right) \tag{2.19}$$

and its amplitude spectrum has the same value. For convenience, we have assumed that $A_{max} = 1$ and $n_{max} = 0$ in Eq. (2.18). Parameter A_{max} is a scaling factor and its value is insignificant when designing the differentiator. The quantity n_{max}, on the other hand, is simply a time-shifting parameter and the amplitude spectrum of a time-shifted sequence is the same as that of the original sequence. By expressing the amplitude spectrum in Eq. (2.19) in terms of the normalized frequency ν, we get

$$|Y_G(\nu)| = b\sqrt{2\pi} \exp\left(\frac{-\pi^2b^2\nu^2}{2}\right) \tag{2.20}$$

Evidently, the amplitude spectrum also has a Gaussian shape that depends only on parameter b which controls the width of the bottom reflection. Fig. 2.10 shows a family of amplitude spectra for various values of b. We observe that for all values of b, the spectrum is monotonically decreasing. Further, except for small values of b, the energy of the function is concentrated in the low-frequency region. Our interest is to establish a relationship between the optimal cutoff frequency ν_c and the width parameter b so that we may determine ν_c based on our knowledge of the typical ranges of b in the LARSEN waveforms. By examining the statistical results obtained from waveform decomposition, we find that, on the basis of a sample of 1000 waveforms collected from different ocean areas, 90 % of the bottom reflections have $b > 4.88$. If ν_c is determined based on the spectrum of the Gaussian function with

$b = 4.88$, we can correctly differentiate most of the bottom reflections. The amplitude spectrum of $y_G(n)$ with $b = 4.88$ is shown in Fig. 2.11. Assuming that frequency components with amplitude spectrum less than -20 dB represent noise, then with the use of Eq. (2.20), a relationship between v_c and b can be derived as $v_c = 0.683/b$. For $b = 4.88$, we obtain $v_c = 0.14$.

For an ideal lowpass digital differentiator with zero phase, the appropriate frequency response is

$$H_d(e^{j\omega T}) = \begin{cases} j\omega & \text{for} \quad |\omega| < \omega_c \\ 0 & \text{for} \quad \omega_c < |\omega| < \dfrac{\omega_s}{2} \end{cases}$$

where ω_c is the highest frequency for which differentiation is required and ω_s is the sampling frequency. A differentiator whose frequency response approximates $H_d(e^{j\omega T})$ can be designed as an FIR digital filter using the window method. In order to obtain an FIR filter of finite order, the ideal impulse response, after truncation, is represented as

$$h(n) = -\frac{1}{\pi}\left(\frac{\sin n\pi v_c}{n^2} - \frac{\pi v_c \cos n\pi v_c}{n}\right) \tag{2.21}$$

for $n = 1, 2, .., K$ where $2K$ is the order of the filter. Note that $h(-n) = -h(n)$ for $n = 1, 2, .., K$, i.e., $h(n)$ is antisymmetrical about the origin.

A good window for the application at hand is the Kaiser window [38] and its application involves multiplying $h(n)$ in Eq. (2.21) by the window function to obtain the required impulse response [39]. The shape parameter, α, of the window can be chosen to be 4.5 and a suitable filter order is 20. As a result, $v_c = 0.14$ and stopband attenuation would be at least 50 dB. The amplitude response of the resulting differentiator is shown in Fig. 2.12.

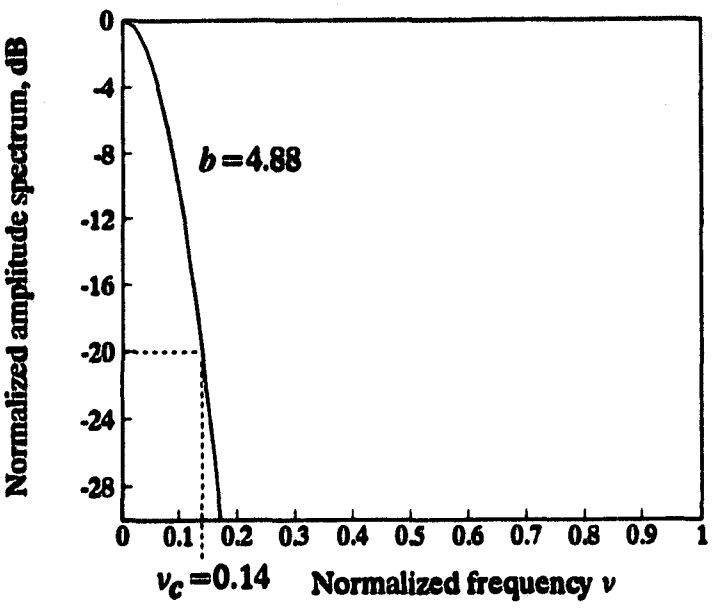

Fig. 2.11 Normalized amplitude spectrum of a Gaussian pulse for $b = 4.88$.

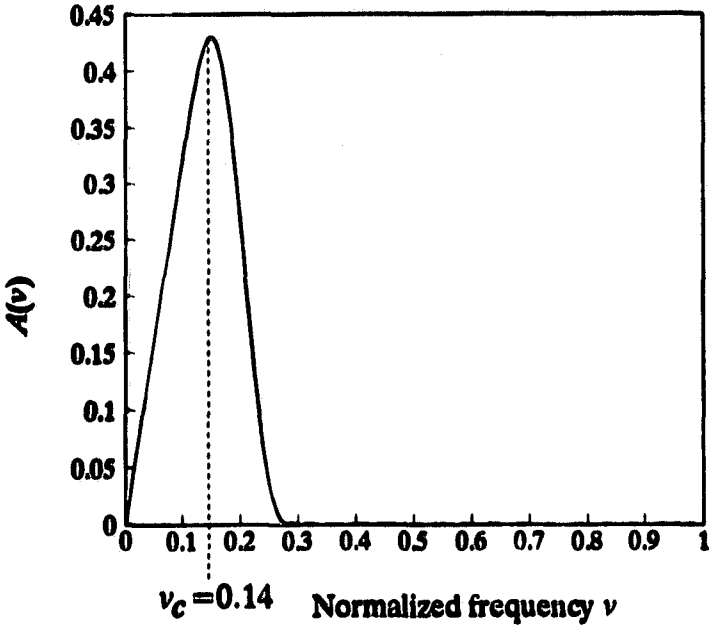

Fig. 2.12 Amplitude response of the lowpass digital differentiator.

C. Simulation Studies

In this section, we present simulation results obtained by using the methods described in Sections 2.4.2-A and 2.4.2-B. Two sets of simulations have been carried out.

In the first set, random noise was added to Gaussian pulses of different widths and then the algorithm was used to estimate the peak position of the Gaussian pulse. The signal-to-noise ratio (SNR) of the signal was varied in the simulation to study the effects of noise on the accuracy of the results. Let

$$y(n) = y_G(n) + w(n)$$

be the degraded signal where $y_G(n)$ is a Gaussian function defined in Eq. (2.18) and assume that $w(n)$ is white noise of zero mean and variance σ_w^2. For the purpose of illustration, an example of differentiation of $y(n)$ is provided in Fig. 2.13. The signal $y(n)$ shown in Fig. 2.13(a) is formed by using $b = 5$ and SNR = 5 dB. The SNR in dB is defined as

$$\text{SNR} = 10\log_{10}\frac{\text{VAR}\,[y_G(n)]}{\text{VAR}\,[w(n)]}$$

where VAR $[\cdot]$ denotes the variance of $[\cdot]$. Fig. 2.13(b) illustrates the differentiated signal and Fig. 2.14 shows the overall results obtained from $y_G(n)$ of different widths and at different SNRs. In general, the root-mean-square (RMS) error between the estimated and true peak positions decreases as the SNR increases, as may be expected. When the SNR is 4 dB, the RMS error is close to 4 samples but when SNR is equal to or exceeds 8 dB, the RMS error is within 1 sample.

The second set of simulations involved the characterization of the LARSEN waveforms by the model described in Section 2.3.3. Different degrees of random noise were added to the simulated waveform to evaluate the accuracy of the method. In addition, values of the parameters in the model were varied in order to test the sensitivity of the algorithm under different ocean conditions. In this case, the degraded signal, which represents the raw LARSEN waveform, is characterized by

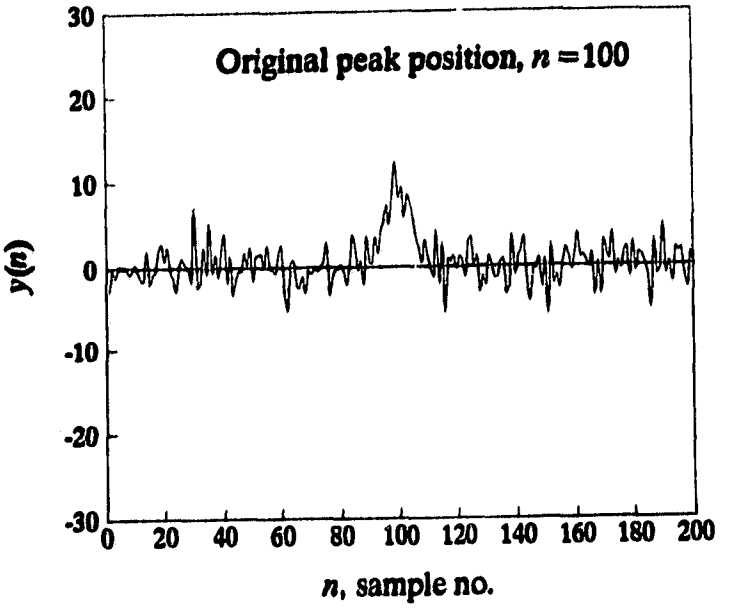

Fig. 2.13(a) Degraded signal $y(n)$, SNR = 5 dB.

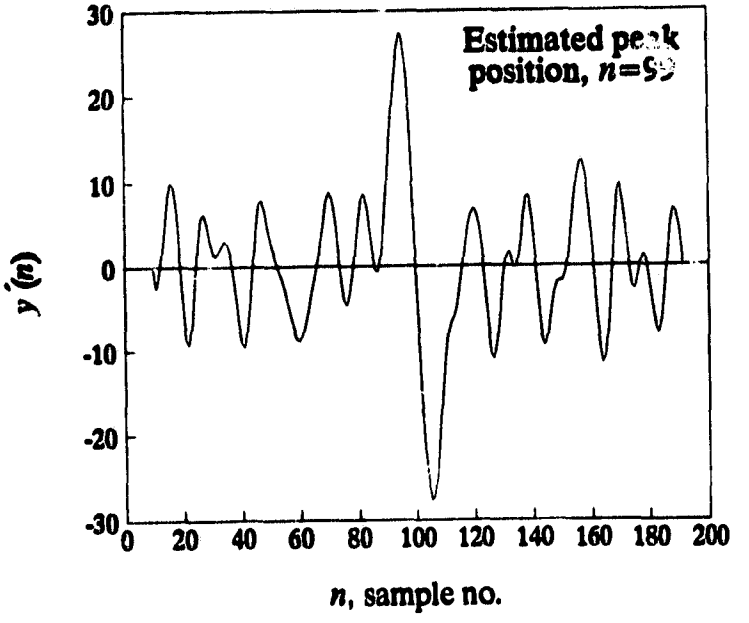

Fig. 2.13( ) Lowpass differentiated signal $y'(n)$.

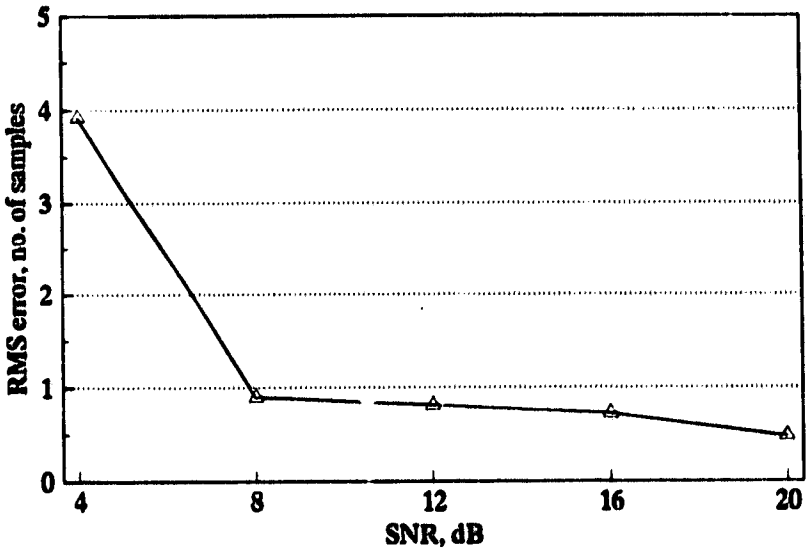

Fig. 2.14 RMS error between the estimated and true peak positions for various SNRs. The values of *b* used in the simulation are 4, 6, 8, 10, 12.

$$y(n) = y_T(n) + w(n)$$

where $y_T(n)$ is the model in Eq. (2.16) in discrete-time representation and $w(n)$ is white noise of zero mean and variance σ_w^2. The seven parameters of $y_T(n)$ were varied in the simulation to adjust the amplitude, pulse width, and peak position of the surface and bottom reflections, as well as the skewness of the backscattered envelope. Fig. 2.15 illustrates an example of lowpass differentiation of $y(n)$.

As described in Section 2.3.3, interference due to multiple returns from the sea may affect the resolution of laser reflections. The resolving power depends on the technique used and some results will be given in this section to show the sensitivity of the developed algorithm under different degrees of resolution between laser reflections. A measure of resolution, which may be referred to as the resolution factor, can be defined as

$$R_S = \frac{\Delta t_p}{N\sqrt{\mu_2}} \tag{2.22}$$

where Δt_p is the time separation between the surface and bottom peak positions, μ_2 is the sum of the second-order central moments of $y_{EMG}(n)$ and $y_G(n)$, and N is a normalizing factor that scales R_S in the range between 0 and 1 for the waveforms examined. Parameter μ_2 is computed as

$$\mu_2 = (\sigma_G^2 + \tau^2) + b^2$$

where σ_G and τ control the width and tailing of $y_{EMG}(n)$, respectively, and b is defined in Eq. (2.18). As Eq. (2.22) implies, small separation between the surface and bottom reflections gives low values of R_S when μ_2 remains constant. Also, an increase in the skewness of the backscattered envelope and/or increase in the pulse width of the bottom reflection can decrease R_S. Note, however, that R_S may not be low even if the separation of the two peak positions is small. This happens when the backscattered envelope is not prominent (i.e., when the water is clear) and the bottom return is narrow.

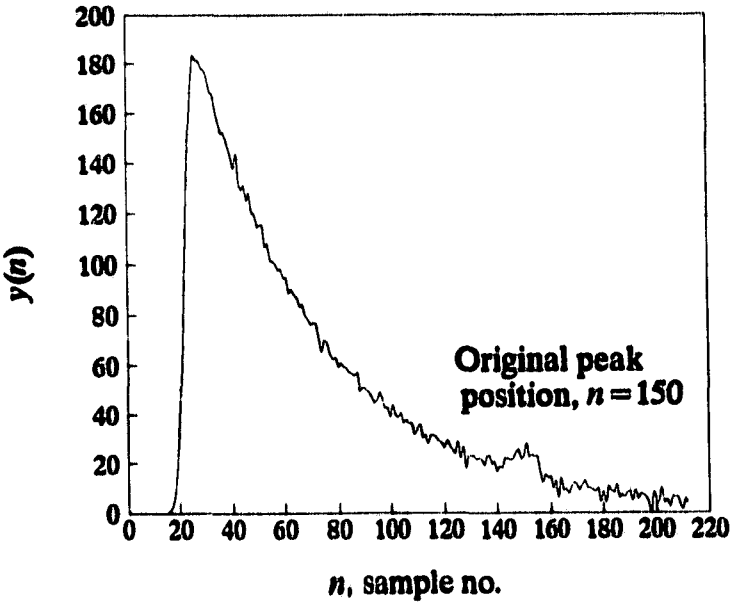

Fig. 2.15(a) Degraded signal $y(n)$.

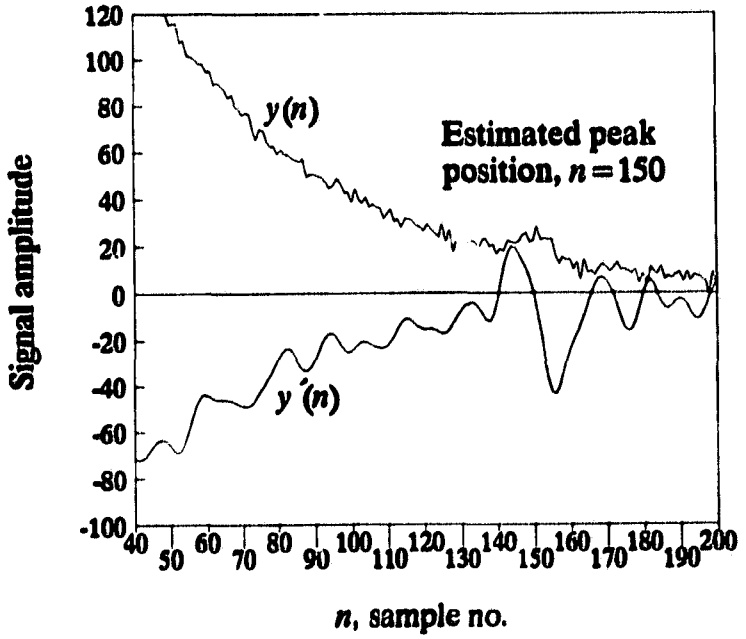

Fig. 2.15(b) Degraded signal and signal after lowpass differentiation.

Fig. 2.16 illustrates the performance of the algorithm at different SNRs for two ranges of R_S. Several observations are in order. First, the trend shown in the graph suggests that as the effects of random noise decrease, the estimated bottom peak position becomes more accurate at both ranges of resolution. Further, for all the SNR values shown, the RMS error is consistently larger for lower R_S. This indicates that interference of laser reflections in the waveform can degrade the performance of the algorithm and thus introduce bias in the estimation. Next, we see that the difference between the RMS errors decreases as the SNR increases, which shows that when the level of the random noise in the waveform is less, the algorithm becomes less sensitive to the variation in R_S, as may be expected.

In general, the algorithm is effective in detecting the peak position of the bottom reflection in the presence of random noise under certain resolution conditions. In conditions where the resolution is fairly low, the accuracy of the algorithm is limited. However, its application offers a number of advantages. They include (1) decreased sensitivity to amplitude variations in the bottom reflection, (2) noise pulses are suppressed rather than amplified as in standard differentiation, and (3) the algorithm is simple to apply.

2.5 CONCLUSIONS

The laser reflections received from the ocean surface and bottom have been interpreted in terms of their moments. On the basis of this interpretation, a special class of digital smoothing filters has been used to preprocess the laser reflections. After preprocessing, we have shown that the important fundamental characteristics, such as peak position, pulse width, and skewness of the laser reflections can be preserved in the noise-reduction process.

In the chapter, we have also developed a mathematical model function to represent LIDAR waveforms received from different situations. In order to gain insight into how the laser reflections in

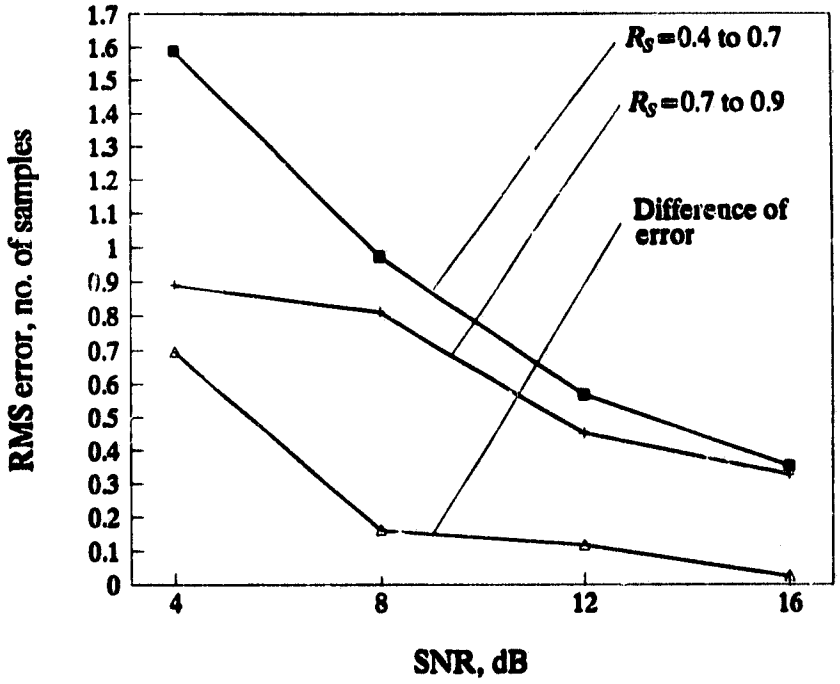

Fig. 2.16 RMS error between the estimated and true peak positions for various SNRs. Two ranges of resolution are considered: R_S = 0.4 to 0.7 and R_S = 0.7 to 0.9.

the waveform interfere with each other, we have varied the model parameters and examined the effects of these parameters on the resolution between the surface and bottom peaks.

Next we have developed two algorithms to identify the surface and bottom peaks in the LARSEN waveforms. The surface peak is identified by means of thresholding and the bottom peak is detected through the incorporation of lowpass digital differentiation. A method for identifying the zero crossing in the lowpass differentiated waveform that corresponds to the bottom reflection is also designed. Simulation studies have been carried out to test the algorithm under different noise and resolution conditions. Results have shown that the algorithm is insensitive to amplitude variations in the bottom reflection and is effective in detecting the bottom peak position provided that the surface and bottom peaks are not fused into a single peak.

CHAPTER THREE
ESTIMATION OF SEA DEPTH

3.1 INTRODUCTION

Surface and bottom reflections in the waveforms overlap and their separation depends on the depth of the ocean. When the sea is deep, the bottom reflection is usually weak and in some cases it is also broadened significantly due to the dispersion of the laser beam in water. Under these circumstances, the bottom reflection may be embedded in the tail of the surface reflection and the separation between the two reflections is lost. On the other hand, when the sea is shallow, the bottom reflection is usually strong and lies close to the surface reflection. They strongly overlap and may merge into a single peak situated in the surface zone. Again, the separation between the two reflections is lost. When the sea is of moderate depth and the water column is of nonuniform turbidity, the bottom reflection may be embedded in the backscattered envelope if the bottom return is not strong enough. The situation may be worse if the bottom reflectivity of the ocean is weak and the reflected pulse is broadened significantly.

Sea depth estimates obtained directly from the LARSEN waveforms may not be sufficiently reliable even when the peaks of the surface and bottom reflections are distinct. The reason is that when there is a certain degree of overlap between the surface and bottom reflections, the position of their peaks will be modified. Specifically, the peak of the surface reflection will shift to the right, and the peak of the bottom reflection will shift to the left, resulting in a smaller depth estimate.

In order to improve the accuracy in sea-depth estimation, we need to first accurately separate the bottom reflection from the surface reflection. From the position of the peaks of these two reflections, we can then determine the sea depth. To do this, we utilized the mathematical model function developed in Chapter 2 along with an optimization technique described in this chapter to decompose LARSEN

waveforms into two separate signal components which represent the surface and bottom reflections. The parameters of the mathematical model estimated from this waveform-decomposition process are then used to obtain sea-depth estimates. Using this technique, depth estimates can be obtained independently of the degree of overlap of the surface and bottom reflections in the LARSEN waveforms.

In this chapter, a scheme for obtaining initial estimates of the model function parameters in Eq. (2.16) is presented. The locations of the surface and bottom peaks that have been detected in each waveform in Chapter 2 are used for this purpose. Then some general optimization methods applicable to this problem are reviewed and a procedure for solving the problem is described. Optimization results are subsequently presented.

In order to help evaluate the results, depth estimates obtained through waveform decomposition are compared with corresponding estimates obtained by a local surveying company using state-of-the-art techniques; furthermore, a statistical analysis of the results is undertaken.

3.2 INITIAL ESTIMATION OF PARAMETERS

If the bottom peak in the LARSEN waveform is not embedded in noise or fused with the surface peak into one, we can identify the bottom peak and obtain an accurate estimate of its position using the algorithm described in Section 2.4.2-A. By using this estimate together with a simple algorithm, the parameters of the Gaussian function in Eq. (2.15) can be estimated directly from the waveform. However, if the bottom peak cannot be identified by this algorithm, the three parameters obtained from the results of the previous waveform can be used as initial estimates for the current waveform. These estimates are fairly accurate since there is, usually, a high degree of spatial correlation among neighboring depths. If the waveform being processed is the first waveform, arbitrary values within the range of interest can be assigned to the three parameters. This assignment is permissible since

optimization algorithms are usually tolerant to initial estimates that are far from the minimum point although the amount of computation could be increased to some extent.

In order to evaluate the four EMG parameters h_G, t_G, σ_G, and τ in Eq. (2.10) from the waveform, an algorithm involving the estimation of the four parameters A_α, B_α, W_α, and t_p illustrated in Fig. 3.1 is used. Parameter α is a fraction of the peak height. W_α is computed as $t_B - t_A$, and A_α and B_α are computed as $t_p - t_A$ and $t_B - t_p$, respectively. With α specified, it is possible to determine the EMG parameters by calculating the second central moment μ_{EMG} of the EMG function [40]. For $\alpha = 0.1$, we have

$$\mu_{EMG} = \frac{W_\alpha^2 (B_\alpha/A_\alpha + 1.25)}{41.7} \tag{3.1}$$

With W_α and B_α/A_α known, parameter σ_G is evaluated as

$$\sigma_G = \frac{W_\alpha}{3.27(B_\alpha/A_\alpha) + 1.2} \tag{3.2}$$

Parameter τ is related to μ_{EMG} and σ_G as

$$\mu_{EMG} = \sigma_G^2 + \tau^2 \tag{3.3}$$

Once μ_{EMG} and σ_G are determined from Eqs. (3.1) and (3.2), τ can be obtained from Eq. (3.3) as

$$\tau = \sqrt{\mu_{EMG} - \sigma_G^2} \tag{3.4}$$

Given t_p, t_G can be determined from σ_G and B_α/A_α as

$$t_G = t_p - \sigma_G\left[-0.193(B_\alpha/A_\alpha)^2 + 1.162(B_\alpha/A_\alpha) - 0.545\right] \tag{3.5}$$

The only parameter left is h_G. However, if we substitute σ_G, τ, and t_G from Eqs. (3.2), (3.4), and (3.5) into Eq. (2.10) and assume that at $t = t_p$, the amplitude of the surface peak is $y_{EMG}(t_p)$; hence h_G can be calculated. Strictly speaking, the amplitude of the surface peak may be modified by the

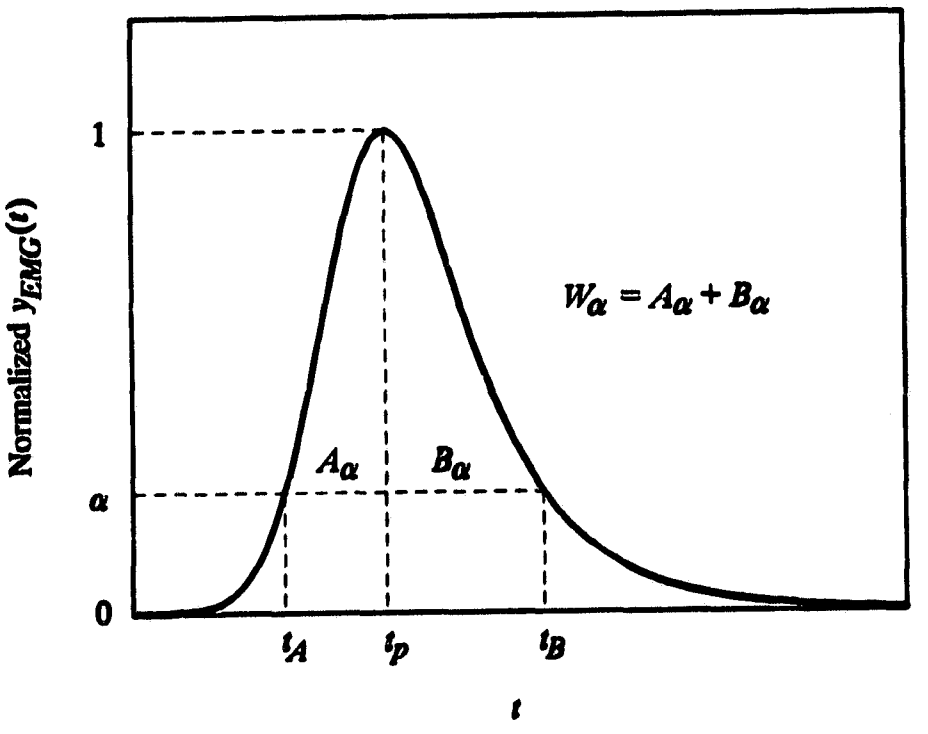

Fig. 3.1 Determination of A_α, B_α, W_α, and t_p from EMG function.

bottom reflection and, therefore, it cannot truly represent the function value $y_{EMG}(t_p)$. Nevertheless, our requirement at this point is to obtain reasonable initial estimates of the function parameters so as to initialize the optimization algorithm. Equations for the computation of the EMG parameters using other values of α are also available in [40]. Tables 3.1 and 3.2 list the equations for $\alpha = 0.3$ and $\alpha = 0.5$, respectively.

Among the three α values we have discussed, the smaller the α used, the more accurate are the EMG parameters obtained. Nevertheless, we have used all three sets of equations. The procedure used to choose α under different circumstances is as follows. Initially, α is chosen as 0.3 to locate t_A and t_B in the waveform. The value 0.1 is not used because of two reasons. If the surface and bottom reflections overlap, it is usually difficult to locate t_B in the waveform. On the other hand, if there is wide separation between the surface and bottom returns, the sea is very deep and deep waters can increase the pulse broadening effect. In such a case, it may not be possible to locate t_B with $\alpha = 0.1$ as illustrated in Fig. 3.2. However, using $\alpha = 0.3$, as illustrated in Fig. 3.2, yields satisfactory results for most waveforms. However, this value of α cannot guarantee the location of t_B. For example, if the bottom return is strong and the water is not deep, the bottom and surface returns overlap strongly and t_B cannot be located. Fig. 3.3 illustrates an example where t_B cannot be located with $\alpha = 0.1$ or $\alpha = 0.3$. When t_B cannot be located using $\alpha = 0.3$, α is changed to 0.5 and the location process is continued. Fig. 3.3 shows how t_B can be obtained when $\alpha = 0.5$. When the sea is very shallow, the bottom reflection is usually strong and situated close to the surface reflection. As shown in Fig. 3.4, the two reflections can overlap to such a degree in such a case that the location of t_B is not possible even when $\alpha = 0.5$. However, if we examine the simulated waveform more closely, we find that the trailing portion of the waveform is contributed solely by the EMG function (dotted line) and the Gaussian

TABLE 3.1

EQUATIONS FOR THE COMPUTATION OF THE EMG PARAMETERS FOR $\alpha = 0.3$.

$$\mu_{EMG} = \frac{W_\alpha^2 (B_\alpha / A_\alpha - 0.3)}{6.88}$$

$$\sigma_G = \frac{W_\alpha}{2.8(B_\alpha / A_\alpha) + 0.48}$$

$$\tau = \sqrt{\mu_{EMG} - \sigma_G^2}$$

$$t_G = t_p - \sigma_G \left[-0.6(B_\alpha / A_\alpha)^2 + 2.58(B_\alpha / A_\alpha) - 1.58 \right]$$

TABLE 3.2

EQUATIONS FOR THE COMPUTATION OF THE EMG PARAMETERS FOR $\alpha = 0.5$.

$$\mu_{EMG} = \frac{W_\alpha^2 (B_\alpha / A_\alpha - 0.7)}{1.83}$$

$$\sigma_G = \frac{W_\alpha}{2.5(B_\alpha / A_\alpha)}$$

$$\tau = \sqrt{\mu_{EMG} - \sigma_G^2}$$

$$t_G = t_p - \sigma_G \left[-1.46(B_\alpha / A_\alpha)^2 + 5(B_\alpha / A_\alpha) - 3.14 \right]$$

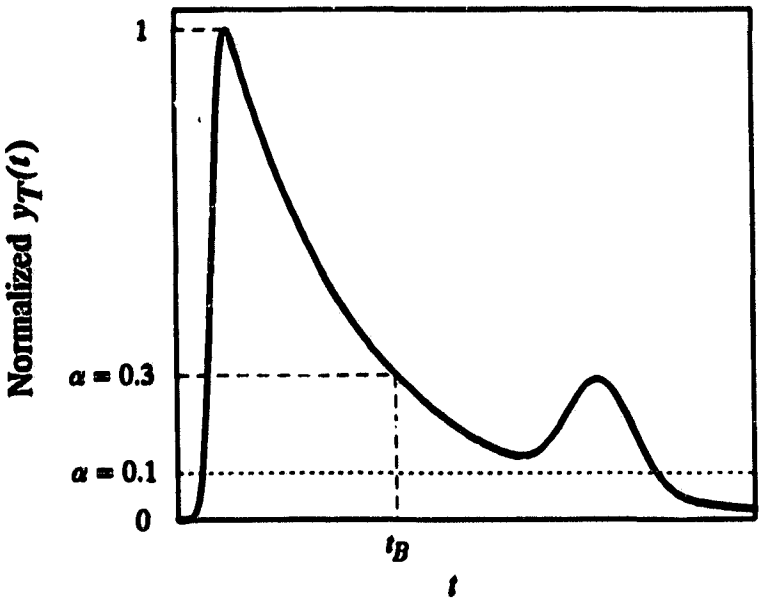

Fig. 3.2 An example illustrating the case where t_B cannot be located with $\alpha = 0.1$.

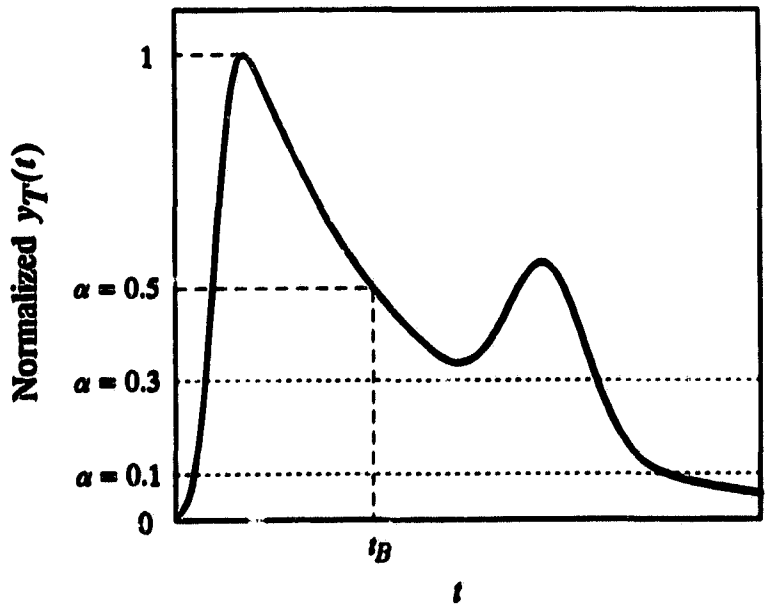

Fig. 3.3 An example illustrating the case where t_B can be located with $\alpha = 0.5$.

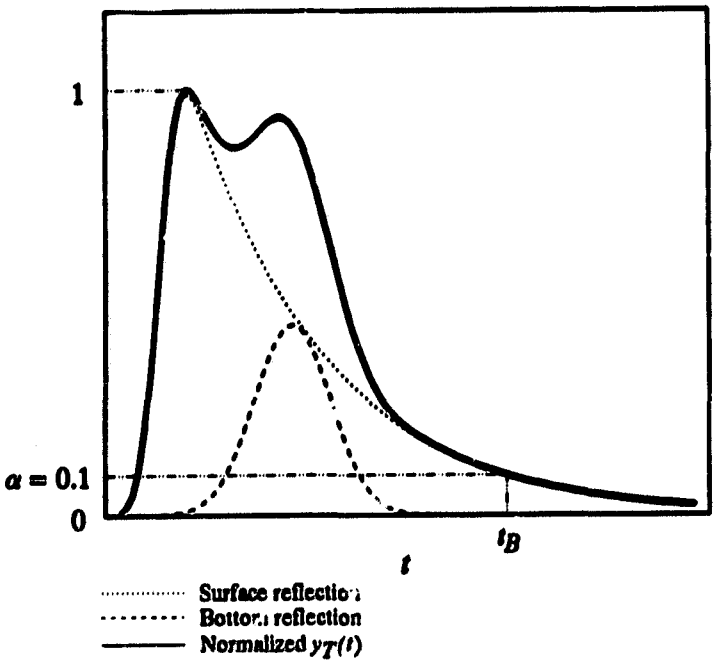

Fig. 3.4 An example illustrating the case where t_B can be located with $\alpha = 0.1$ even though t_B is beyond the location of the bottom peak.

function (dashed line) resides only in a specific region. In this case, we can conclude that $\alpha = 0.1$ can locate t_B since the tail of the EMG function is not modified even though t_B is beyond the location of the bottom peak. Therefore, if t_B cannot be located with $\alpha = 0.5$, we assume that the surface and bottom returns are strongly overlapping. In such a case, we switch α to 0.1 and start the location process for t_B again. We should note that the trailing part of the waveform may not be contributed solely by the surface reflection even if the two reflections strongly overlap. However, when the water is very shallow the pulse broadening effect is reduced and thus the bottom reflection hardly extends to the trailing part of the waveform. It should be noted that the Gaussian and EMG function parameters, obtained from the waveform using the results of Chapter 2 and the measurements referred to in Fig. 3.1 are only approximations due mainly to the fact that the surface and bottom reflections are overlapping. In order to decompose the waveform into separate and more accurate components, a procedure utilizing an optimization technique will be used. This is described in the following section.

3.3 OPTIMIZATION OF PARAMETERS

A smoothed waveform can be decomposed into two signal components representing the surface and bottom reflections by fitting the waveform to a mathematical model function which involves a number of adjustable parameters. The model in our case is (see Eq. (2.16))

$$y_T(t) = y_{EMG}(t) + y_G(t) \tag{3.6}$$

The basic approach is to construct an objective function that will measure the difference between the data and $y_T(t)$ for a particular selection of the seven parameters of $y_G(t)$ and $y_{EMG}(t)$ in Eq. (3.6). The parameters of $y_T(t)$ are then adjusted to minimize the objective function, thereby yielding the parameter values that correspond to the best fit. The adjustment process is thus a problem in minimization in many dimensions.

Let $E(\mathbf{x})$ be the objective function and $\mathbf{x} = [h_G \; t_G \; \sigma_G \; \tau \; A_{max} \; t_{max} \; \sigma]^T$ be the vector of the parameters of $y_T(t)$. $E(\mathbf{x})$ is a function dependent on the elements of $\mathbf{x}$ and the independent variable t of the form

$$E(\mathbf{x}) = g\left\{e(\mathbf{x}, t_1),\ e(\mathbf{x}, t_2),\ \ldots,\ e(\mathbf{x}, t_m)\right\} \tag{3.7}$$

where $t_1, t_2, \ldots, t_m$ are values of t at the m sample points. The residuals $e(\mathbf{x}, t_k)$ are given by

$$e(\mathbf{x}, t_k) = e_k(\mathbf{x}) = y_T(\mathbf{x}, t_k) - y(t_k) \tag{3.8}$$

for $k = 1, 2, \ldots, m$ where $y(t_k)$ represents the smoothed waveform. Our goal is to minimize $E(\mathbf{x})$ by varying the elements of $\mathbf{x}$.

The objective function $E(\mathbf{x})$ can assume several forms. In the problem at hand, the sum of squares of the residuals $e_k(\mathbf{x})$, namely,

$$E(\mathbf{x}) = \sum_{k=1}^{m} e_k^2(\mathbf{x}) = \mathbf{e}(\mathbf{x})^T \mathbf{e}(\mathbf{x}) \tag{3.9}$$

where

$$\mathbf{e}(\mathbf{x}) = [e_1(\mathbf{x}) \cdots e_k(\mathbf{x}) \cdots e_m(\mathbf{x})]^T \tag{3.10}$$

was found to give good results.

The method used to minimize $E(\mathbf{x})$ is known as the Levenberg-Marquardt method which was proposed by Levenberg [41] and enhanced by Marquardt [42]. This method utilizes the specific least-squares structure of Eq. (3.9) in minimization and takes advantage of the fast convergence of the steepest-descent method far from the minimum point and the fast convergence of the Newton-Raphson method as the minimum point is approached. Various implementations of the Levenberg-Marquardt method have been proposed and the approaches of Powell [43], Osborne [44], and Mofe [45] can achieve convergence from almost any starting point. In our case, we have adopted the trust-region approach [45]-[46] to find the search direction and step length in each iteration in order to assure convergence. The methods that make use of this approach in minimization are also referred to as

restricted-step methods by Fletcher [47]. In the following, we first briefly review the mathematical details of both the steepest-descent method and Newton-Raphson methods. We then describe the problem formulation of the Levenberg-Marquardt method with the trust-region approach and present its solution.

The steepest-descent and Newton-Raphson methods are both gradient methods for optimization based on the Taylor expansion given by

$$f(\mathbf{x} + \mathbf{s}) \approx f(\mathbf{x}) + \mathbf{g}(\mathbf{x})^T \mathbf{s} + \frac{1}{2} \mathbf{s}^T \mathbf{H}(\mathbf{x}) \mathbf{s} \tag{3.11}$$

with the terms involving third- and higher-order derivatives neglected. Vector $\mathbf{g}$ in Eq. (3.11) is known as the gradient vector and $\mathbf{H}$ as the Hessian matrix [47]. Both are evaluated at the current point $\mathbf{x}$. Eq. (3.11) can also be expressed as

$$f(\mathbf{x} + \mathbf{s}) \approx f(\mathbf{x}) + \Delta f \tag{3.12}$$

where the scalar correction Δf corresponds to the last two terms in Eq. (3.11).

Optimization methods in which the final term in Eq. (3.11) is neglected are termed first-order methods. In these methods, second derivatives are assumed small enough to be neglected. If an optimization method utilizes second derivatives, it is termed a second-order method. The steepest-descent method uses the gradient $\mathbf{g}$ to determine a suitable direction of movement $\mathbf{s}$ and it is the most fundamental first-order method. On the other hand, the Newton-Raphson method uses the Hessian matrix $\mathbf{H}$ to determine $\mathbf{s}$ and therefore it is a second-order method.

To determine $\mathbf{s}$ by using the steepest-descent method, Δf in Eq. (3.12) is expressed as

$$\Delta f = \mathbf{g}(\mathbf{x})^T \mathbf{s}$$

Our purpose is to determine the maximum negative value of Δf so that $f(\mathbf{x} + \mathbf{s})$ in Eq. (3.12) is minimized. It can be shown that the step $\mathbf{s}$ in this method is given by

$$\mathbf{s} = -\gamma \frac{\mathbf{g}(\mathbf{x})}{|\mathbf{g}(\mathbf{x})|}$$

with $\gamma > 0$ chosen such that $f(\mathbf{x} + \mathbf{s})$ is minimized.

The steepest-descent method is usually robust, is simple to apply, and converges rapidly at points which are not in the neighborhood of the solution. However, as the solution is approached convergence becomes very slow. The Newton-Raphson method, described as below, overcomes this disadvantage.

In the Newton-Raphson method, our objective is to determine the required $\mathbf{s}$ to approximate the minimum of $f(\mathbf{x} + \mathbf{s})$ in Eq. (3.11) from the point $\mathbf{x}$. Expanding Eq. (3.11) into coordinate form yields

$$f(\mathbf{x} + \mathbf{s}) \approx f(\mathbf{x}) + \sum_{i=1}^{n} \frac{\partial f(\mathbf{x})}{\partial x_i} s_i + \frac{1}{2} \sum_{i=1}^{n} \sum_{j=1}^{n} s_i \frac{\partial^2 f(\mathbf{x})}{\partial x_i \partial x_j} s_j \tag{3.13}$$

To approximate $\mathbf{s}$, consider $\mathbf{g}$ and $\mathbf{H}$ fixed and partially differentiate Eq. (3.13) with respect to the elements s_j, $j = 1, 2, \ldots, n$. Setting the results to zero gives

$$\frac{\partial f(\mathbf{x})}{\partial x_j} + \sum_{i=1}^{n} s_i \frac{\partial^2 f(\mathbf{x})}{\partial x_i \partial x_j} = 0 \tag{3.14}$$

for $j = 1, 2, \ldots, n$. By expressing Eq. (3.14) in matrix form and solving for $\mathbf{s}$, we get

$$\mathbf{s} = -\mathbf{H}(\mathbf{x})^{-1} \mathbf{g}(\mathbf{x}) \tag{3.15}$$

The convergence of the Newton-Raphson method is rapid when $\mathbf{x}$ is close to the minimum. However, if $\mathbf{x}$ is far from the minimum, convergence is slow and steady progression towards the minimum cannot be guaranteed.

3.3.1 The Gauss-Newton least-squares method

An iterative method developed for solving nonlinear least-squares problems is referred to as the Gauss-Newton method. This method is designed based on the Newton-Raphson method and, therefore, $\mathbf{g}$ and $\mathbf{H}$ must be obtained in each iteration in order to compute $\mathbf{s}$ in Eq. (3.15). Referring to our least-squares minimization problem in Eq. (3.9), the elements of $\mathbf{g}$ can be derived by partial differentiation of $E(\mathbf{x})$ with respect to each parameter in turn as

$$\frac{\partial E(\mathbf{x})}{\partial x_i} = \sum_{k=1}^{m} 2 e_k(\mathbf{x}) \frac{\partial e_k(\mathbf{x})}{\partial x_i} \tag{3.16}$$

for $i = 1, 2, ..., n$. Using the first-derivative matrix

$$\mathbf{J}(\mathbf{x}) = \begin{bmatrix} \frac{\partial e_1}{\partial x_1} & \cdots & \frac{\partial e_1}{\partial x_i} & \cdots & \frac{\partial e_1}{\partial x_n} \\ \vdots & & \vdots & & \vdots \\ \frac{\partial e_k}{\partial x_1} & \cdots & \frac{\partial e_k}{\partial x_i} & \cdots & \frac{\partial e_k}{\partial x_n} \\ \vdots & & \vdots & & \vdots \\ \frac{\partial e_m}{\partial x_1} & \cdots & \frac{\partial e_m}{\partial x_i} & \cdots & \frac{\partial e_m}{\partial x_n} \end{bmatrix}$$

Eq. (3.16) becomes

$$\mathbf{g}(\mathbf{x}) = 2\mathbf{J}(\mathbf{x})^T \mathbf{e}(\mathbf{x}) \tag{3.17}$$

where

$$\mathbf{g}(\mathbf{x}) = \left[\frac{\partial E(\mathbf{x})}{\partial x_1} \cdots \frac{\partial E(\mathbf{x})}{\partial x_i} \cdots \frac{\partial E(\mathbf{x})}{\partial x_n} \right]^T$$

and $\mathbf{e}(\mathbf{x})$ is defined in Eq. (3.10).

Now assuming that the e_k, $k = 1, 2, ..., m$ has continuous second-order partial derivatives, partial differentiation of Eq. (3.16) with respect to each parameter gives

$$\frac{\partial^2 E}{\partial x_i \partial x_j} = 2 \sum_{k=1}^{m} \frac{\partial e_k(\mathbf{x})}{\partial x_i} \frac{\partial e_k(\mathbf{x})}{\partial x_j} + 2 \sum_{k=1}^{m} e_k(\mathbf{x}) \frac{\partial^2 e_k(\mathbf{x})}{\partial x_i \partial x_j} \tag{3.18}$$

If we assume that the second term in Eq. (3.18) is negligible, we have

$$\frac{\partial^2 E}{\partial x_i \partial x_j} \approx 2 \sum_{k=1}^{m} \frac{\partial e_k(\mathbf{x})}{\partial x_i} \frac{\partial e_k(\mathbf{x})}{\partial x_j} \tag{3.19}$$

Eq. (3.19) for i and $j = 1, 2, ..., n$ gives approximations for the elements of the Hessian matrix and hence we can write

$$\mathbf{H}(\mathbf{x}) = 2\mathbf{J}(\mathbf{x})^T \mathbf{J}(\mathbf{x}) \tag{3.20}$$

Using Eqs. (3.17) and (3.20), the step in the Newton-Raphson minimization procedure given in Eq. (3.15) may now be written as

$$\mathbf{s} = -\left[\mathbf{J}(\mathbf{x})^T \mathbf{J}(\mathbf{x})\right]^{-1} \mathbf{J}(\mathbf{x})^T \mathbf{e}(\mathbf{x}) \tag{3.21}$$

3.3.2 The Levenberg-Marquardt least-squares method with the trust-region approach

In the neighborhood of the solution, $\mathbf{J}(\mathbf{x})^T\mathbf{J}(\mathbf{x})$ is positive definite in Eq. (3.21) and so the application of the Gauss-Newton method in minimization would converge. However, at points far from the minimum or when the minimization problem is highly nonlinear, the procedure may not converge to yield a minimum. There are two ways to improve the Gauss-Newton method: Use the method with (1) a line-search approach or (2) a trust-region approach. When the method is modified to include line searching, the step $\mathbf{s}$ in Eq. (3.21) can be modified as

$$\mathbf{s} = -\gamma\left[\mathbf{J}(\mathbf{x})^T \mathbf{J}(\mathbf{x})\right]^{-1} \mathbf{J}(\mathbf{x})^T \mathbf{e}(\mathbf{x}) \tag{3.22}$$

where $\gamma > 0$ is the line-search parameter. The method that uses Eq. (3.22) in least-squares optimization is usually referred to as the damped Gauss-Newton method.

An alternative way to improve the Gauss-Newton method is to modify not only the step length but also the search direction. The trust-region approach to minimization is to find a step $\mathbf{s}$ that solves

$$\begin{aligned} &\min m(\mathbf{x}+\mathbf{s}) = E(\mathbf{x}) + \mathbf{g}(\mathbf{x})^T\mathbf{s} + \frac{1}{2}\mathbf{s}^T\mathbf{H}(\mathbf{x})\mathbf{s} \\ &\text{subject to } \|\mathbf{s}\|_2 \le \delta \end{aligned} \tag{3.23}$$

where m is the local quadratic model of $E(\mathbf{x})$ in the neighborhood of $\mathbf{x}$ and δ is the trust radius that defines the size of the trust region. Norm $\|\mathbf{s}\|_2$ in Eq. (3.23) represents the Euclidean norm of the step $\mathbf{s}$. From Eqs. (3.9), (3.17), and (3.20), we can rewrite Eq. (3.23) as

$$\min m(x + s) = e(x)^T e(x) + 2 s^T J(x)^T e(x) + s^T J(x)^T J(x) s \quad \text{subject to } \|s\|_2 \le \delta \tag{3.24}$$

The solution of Eq. (3.24), which can be obtained using the Levenberg-Marquardt method, is given by

$$s(\lambda) = -\left[\lambda I + J(x)^T J(x)\right]^{-1} J(x)^T e(x) \quad \text{for } \|s(\lambda)\|_2 \le \delta \tag{3.25}$$

where λ is a non-negative scalar and I is the $n \times n$ identity matrix. For a sufficiently large value of λ, the matrix $\lambda I + J(x)^T J(x)$ in Eq. (3.25) is positive definite. In this case, the divergence of the process is avoided even when the solution is far from the minimum. As $\lambda \to \infty$, the effect of the term λI increasingly dominates that of $J(x)^T J(x)$ so that $s(\lambda)$ in Eq. (3.25) tends to

$$s(\lambda) = -\frac{J(x)^T e(x)}{\lambda}$$

Using Eq. (3.17), the above equation can be rewritten as

$$s(\lambda) = -\left(\frac{1}{2\lambda}\right) g(x)$$

which is essentially an increment in the steepest-descent direction. On the other hand, when $\lambda \to 0$ Eq. (3.25) tends to the standard Gauss-Newton increment in Eq. (3.21).

From Eq. (3.25), we see that the minimization process involves two major steps. The first is to choose the size of the trust region δ and the second is to find a value for λ such that the vector $s(\lambda)$ satisfies Eq. (3.25) for a specified δ. To improve the speed of convergence, δ can be varied adaptively using the values of δ and $E(x)$ obtained in the previous iteration. A minimization algorithm based on the above principles [46] is as follows:

1. Initialize x and δ. Set $x_c = x$ and evaluate $E_c = E(x_c)$.
2. Set $\lambda = 0$, compute $s_N = s(\lambda)$ using Eq. (3.25), and evaluate $\|s_N\|_2$.
3. If $\|s_N\|_2 \le 1.5\delta$ then set $s = s_N$, $\delta = \min\{\delta, s_N\}$ and go to Step 5.

4. Find a value of λ, λ^*, and a corresponding vector $s(\lambda^*)$ using Eq. (3.25) such that $\|s(\lambda^*)\|_2 \in [0.75\delta, 1.5\delta]$. Set $s = s(\lambda^*)$.

5. Set $x_+ = x_c + s$. Evaluate $E_+ = E(x_+)$ and $\Delta E = E_+ - E_c$.

6. If $\Delta E \geq 0$ then reduce δ such that $\delta \in [0.1\delta, 0.5\delta]$ and go to Step 4.

7. Compute $m(x_+)$ using Eq. (3.24) and set $\Delta E_{pred} = m(x_+) - E_c$. Compute $R = \Delta E / \Delta E_{pred}$. If $R \leq 0.1$ then set $\delta = \delta/2$; else if $R \geq 0.75$ then set $\delta = 2\delta$.

8. If $|s_i|/(\beta + |x_{ci}|) < \alpha$ for $i = 1, 2, ..., n$ then output $x_f = x_+$, $E_f = E_+$ and stop; else set $x_c = x_+$, $E_c = E_+$ and go to Step 2.

Vector x can be initialized using estimates based on the method of Section 3.2 and the trust radius δ can be initialized as the size of the Cauchy step [46], [48], which is the size of the step s that minimizes $m(x + s)$ in the steepest-descent direction. In the algorithm, Eq. (3.25) is solved as follows. If the size of the Gauss-Newton step $\|s_N\|_2$ obtained from Eq. (3.25) with $\lambda = 0$ is less than or equal to the upper bound of the trust region, which is chosen as 1.5δ, then we make a trial step to point x_+ and decide whether x_+ is acceptable for the next iteration. However, if the size of the Gauss-Newton step is greater than the upper bound, we obtain s by solving Eq. (3.25) for λ using the iterative process detailed in [45]-[46] such that $\|s(\lambda)\|_2 \approx \delta$. In practice, the condition $\|s(\lambda^*)\|_2 \in [0.75\delta, 1.5\delta]$ should be satisfied.

To decide whether the trial step s obtained either from Step 3 or Step 4 is successful, we compare the two values of the objective function obtained in Steps 1 and 5, namely, E_c obtained at the current point x_c and E_+ at the trial point x_+. If there is a reduction in the objective function, x_+ is accepted and the trust region is modified for the next iteration. Otherwise, the trust region is reduced in size and $s(\lambda)$ is obtained by solving Eq. (3.25) for the new trust region. The amount of the reduction in the trust region can be obtained using a method based on quadratic interpolation as described in [46]. The

relative change in x is checked in Step 8 and the algorithm is stopped when the norm of s is within the step tolerance. Typical values for α and β used in waveform decomposition are given in Table 3.3 as will be described in the next section.

3.3.3 Optimization results and discussions

In this section, we illustrate the decomposition method by two examples. Example 1 illustrates the case where the surface and bottom reflections strongly overlap and merge into a single peak in the received waveform. As can be seen in Fig. 3.5(a), the optimization algorithm has resolved the waveform into two reflections; the sea depth can, therefore, be easily determined from the peak positions of these two reflections. The small separation between the surface and bottom reflections in Fig. 3.5(a) indicates that the water is very shallow. In Example 2, the waveform was obtained in an area where the sea is relatively deep and the water column has nonuniform turbidity. Fig. 3.5(b) shows the smoothed waveform and its decomposition. Although the backscattered envelope is distorted with peaks and lumps which cannot be fully eliminated by digital smoothing, the weak bottom reflection was detected by the optimization algorithm. The results obtained in these two examples are given in Table 3.3. As can be seen, the CPU time and number of function evaluations required in the optimization depend heavily

TABLE 3.3
OPTIMIZATION RESULTS OBTAINED IN EXAMPLES 1 AND 2

Example	α	β	CPU Time, s	Func. Evals.	Depth, m	Error $\times 10^{-2}$
1	0.1	0.001	8.7	5	2.7	2.56
	0.01	0.001	19.9	10	2.7	2.38
2	0.1	0.001	9.8	5	28.7	3.27
	0.01	0.001	22.6	11	28.8	2.95

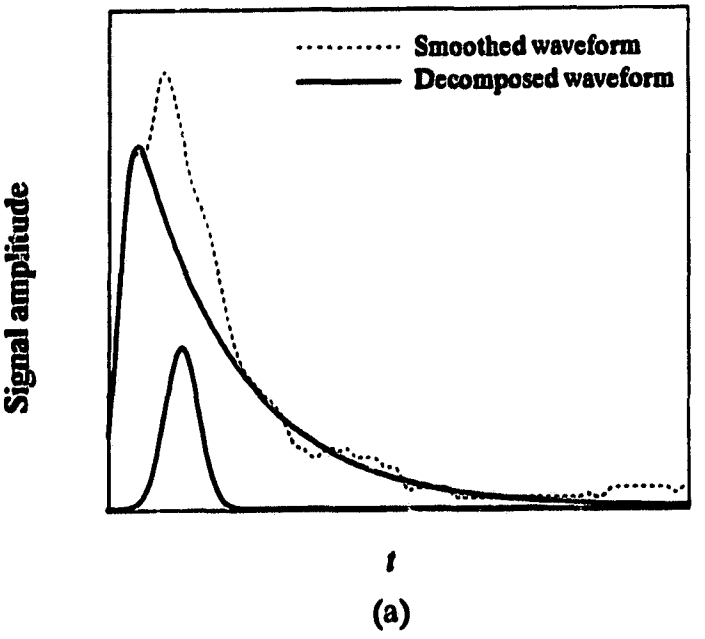

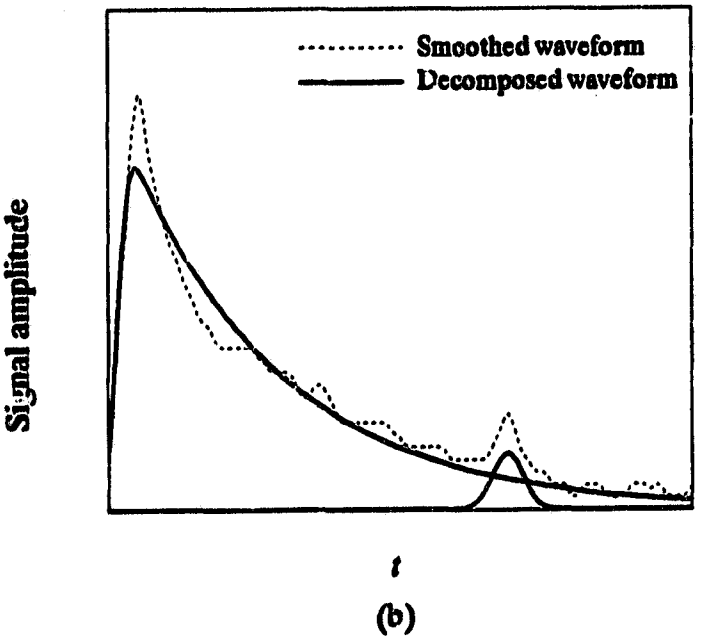

Fig. 3.5 Smoothed waveform decomposed into surface and bottom reflections: (a) very shallow water, strong bottom reflection; (b) deep water, weak bottom reflection.

on the values of α and β, the parameters in the stopping criterion. The normalized root-mean-square (RMS) error in the least-squares optimization is computed as $\sqrt{[E(\mathbf{x})/m]}\,/A$, where A is the maximum amplitude of the smoothed waveform, and m is the number of data points in the waveform. Vector $\mathbf{x}$ is initialized using estimates based on the method of Section 3.2. The decomposed reflections shown in Figs. 3.5(a) and (b) were obtained using $\alpha = 0.1$ and $\beta = 0.001$. The computer used was a Sun-3/160c workstation based on the Motorola MC68020 CPU chip and is equipped with a MC68881 floating-point coprocessor. Table 3.4 gives the average processing time, number of function evaluations required, and normalized RMS error obtained when 500 waveforms were processed with $\alpha = 0.1$ and $\beta = 0.001$.

The values of the parameters in the stopping criterion, namely, α and β, have been selected to achieve a compromise between processing speed and accuracy of the results. In practice, however, these parameters can be adjusted to suit the area being surveyed. They may also be set by some adaptive mechanism.

The use of optimization techniques in the estimation of sea depth offers several advantages. First, the overlapping surface and bottom reflections in the waveform are mathematically resolved into two separate components. Therefore, both the detection and resolution problems can be solved simultaneously. Furthermore, the method is insensitive to changes to the degree of overlap. Consequently, more accurate results compared to those in Chapter 2 can be obtained. However, initial estimation of the model parame-

TABLE 3.4
AVERAGE CPU TIME, FUNCTION EVALUATIONS, AND NORMALIZED RMS ERROR IN OPTIMIZATION. ($\alpha = 0.1$, $\beta = 0.001$)

Waveforms	Depth, m	CPU Time, s	Func. Evals.	Error
500	1.5 to 40	9.2	5	2.71×10^{-2}

ters of $y_T(t)$ is required in the optimization process and for rapid convergence, good estimates are necessary. In fact, the accuracy of the initial estimates relies upon the locations of the surface and bottom peaks obtained in Chapter 2. With reliable peak locations, we can then use the algorithm described in Section 3.2 to provide reliable initial estimates. In the case when the waveform is poorly represented by $y_T(t)$, unreliable initial estimates may result in slow convergence or convergence on to false values.

As in Chapter 2, the peak locations of the surface and bottom reflections can be used to estimate the sea depth. To locate t_p in Fig. 3.1, the EMG function is first evaluated using the optimized EMG parameters. Based on the fact that t_p is always greater than t_G, it can be easily located using an iterative search scheme.

The model parameters used in estimating sea depths may also be used to investigate the optical properties of the sea. Recent studies [5], [16], [49] have shown that the physical structure of the received laser waveforms, especially the backscattered envelopes, are related to the scattering and absorption of the laser beam in water. For example, the amplitude of the backscattered signal is indicative of the degree of scattering while its decay with time is related to absorption. Since the EMG parameters reflect the physical structure of the backscattered signal, they may be useful in a number of applications. First, with the knowledge of the optical parameters of the ocean, operating limits of the LIDAR system can be characterized and adjustments can be made to maximize its performance. As a result, more accurate depth estimates can be obtained. In addition, the LIDAR bathymeter may also be used for non-bathymetric purposes such as in the measurement of sea water turbidity. A quantitative measure of turbidity is the rate of attenuation of the laser beam in water, and this rate is dependent on the degree of scattering and absorption of the laser light in water.

3.4 COMPARATIVE STUDY

In order to examine the effectiveness of the proposed techniques, a fairly extensive comparative study has been undertaken. In this study, waveforms collected in a survey in the Canadian Central Arctic in 1990 using the LARSEN 500 airborne system were processed using the following procedure. First, waveforms were smoothed by the 12th-order digital smoothing filter as described in Section 2.2 to remove noise. The surface-detection and depth-detection algorithms described in Section 2.4 were then applied to the smoothed waveform for the estimation of the blue-green surface and bottom peak positions. Using these estimates, the decomposition technique described in Section 3.3 was then applied to the smoothed waveform to extract the bottom return. Sea depth was subsequently estimated according to the peak position of the extracted bottom return. The depth estimates obtained were then compared with corresponding estimates obtained by a local surveying company.

The processing applied by the surveying company involved the use of heuristic rules in the algorithm to identify the bottom reflection in the waveform. Specifically, the algorithm assigns a confidence level to each possible bottom return pulse in a waveform and the pulse with the highest confidence level is selected and regarded as the laser reflection from the ocean bottom. The confidence level is assigned on the basis of the characteristics of a pulse, which include the amplitude and width of a pulse as well as the ratio between these two quantities. The algorithm can keep track of the location of the selected bottom reflection in a series of waveforms and the corresponding trend thus established is used to correct for anomalies in the data. When the bottom reflection is identified, the peak of the reflection is located directly from the waveform and sea depth is then estimated based on this peak position.

In both approaches, the location of the surface reflection chosen for sea-depth estimation is the peak position of the synthetic infrared pulse generated by the LARSEN 500. The two sets of depth estimates reported have been corrected for tide and path correction for the scanning beam geometry has been applied.

When the resolution between the laser reflections is very low, sea-depth estimates are not available from the surveying company. In order to evaluate the decomposition results under this circumstance, we have formulated a procedure in Chapter 4 to perform further comparisons.

3.4.1. Difference in depth estimates as a function of sea depth

Let d_{WD} be the depth estimate obtained by the waveform decomposition, d_{TS} the estimate obtained by the surveying company, $d_f = d_{WD} - d_{TS}$ their difference, and

$$d_r = \frac{|d_f|}{d_{TS}} \times 100\,\%$$

the magnitude of the difference expressed as a percentage. We first analyzed d_r by examining how d_r is distributed in different sea-depth ranges. To do this, we grouped d_r into several categories according to its size, and then we crosstabulated each category of d_r with d_{WD}, as shown in Table 3.5.

Table 3.5 is a row-percentage table in which the sum of all the percentages in each row is 100 %. The advantage of using the row-percentage format is that we are able to make comparisons across different sea-depth ranges even though the number of waveforms collected in each depth range is not uniform. From Table 3.5, we can make the following observations. For depth ranges from 5 to 10 m, a total of 89.1 % of d_f are within 6 % of d_{TS}. When depth ranges from 10 to 20 m, a total of 88.6 % of d_f are within 3 % of d_{TS}. When depth ranges from 20 to 40 m, at least 99 % of d_f are within 2 % of d_{TS}. These results are derived from processing 1000 waveforms collected from various areas in the Canadian Central Arctic.

TABLE 3.5
DISTRIBUTION OF d_f FOR DIFFERENT SEA-DEPTH RANGES
(NUMBERS SHOWN ARE ROW PERCENTAGES)

	d_f, percent				
d_{WD}, m	< 1	1 - 2	2 - 3	3 - 6	6 - 12
5 to 10	6.3	9.4	15.6	57.8	10.9
10 to 20	43.1	35.4	10.1	11.4	
20 to 30	67.7	31.6	0.7		
30 to 40	96.8	3.2			

Comparison of the two results showed agreement particularly when the sea is relatively deep, although differences can be noted. The major cause for the differences is primarily due to the use of different approaches to estimate the location of the bottom reflection in the waveforms. Examination of Table 3.5 suggests that when the sea is deeper, the agreement between the two sets of results increases, and vice versa. In order to explore the implications of these results and make the comparison more meaningful, we have investigated the correlation between d_f and sea depth to understand under what circumstances these differences occur. Our effort indicates that when sea depth ranges from 5 to 10 m and 30 to 40 m, d_f does not appear to be related to d_{WD}. On the other hand, when sea depth ranges from 10 to 20 m and 20 to 30 m, there is a reasonable degree of linear correlation between d_f and d_{WD}, as can be seen in Fig. 3.6(a) and (b). When d_{WD} ranges between 10 and 20 m, a negative correlation exists between d_f and d_{WD}, as can be noted in the scatter plot of Fig. 3.6(a), i.e., d_f becomes more positive as sea depth decreases; the

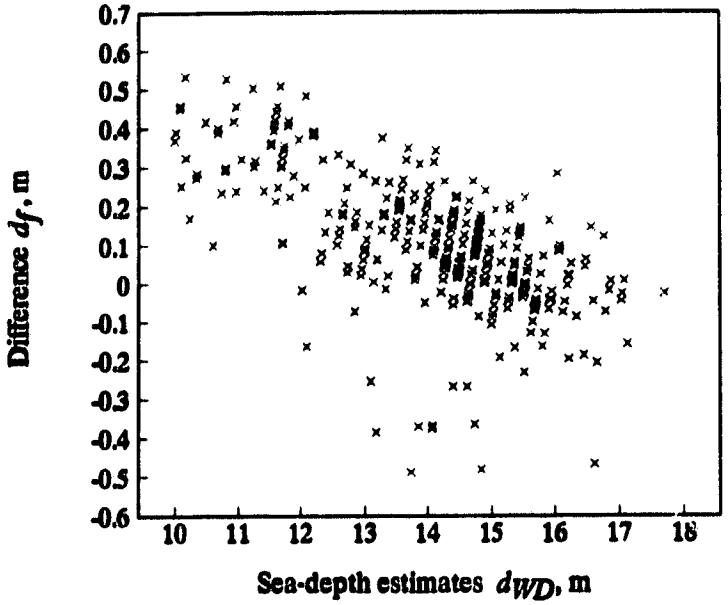

(a)

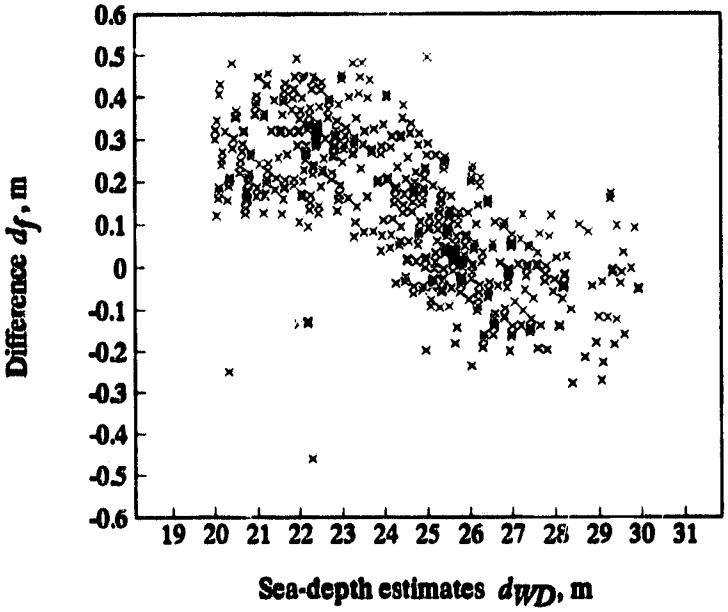

(b)

Fig. 3.6 Scatter plot of d_f versus d_{WD}: (a) sea depth is between 10 and 20 m; (b) sea depth is between 20 and 30 m.

correlation coefficient was found to be -0.63. A similar correlation exists for values of d_{WD} in the range 20 to 30 m, as can be noted in Fig. 3.6(b). In this case, the correlation coefficient was found to be -0.69.

An analysis of the above results will now be undertaken. As discussed in Chapter 1, when a blue-green laser pulse is projected from the aircraft into the water column, some of the photons will be scattered upwards to form the backscattered envelope in the waveform and the shape of this envelope depends on the turbidity of the ocean. For sea depth estimates between 10 and 20 m, the tailing of the backscattered envelope may interfere with the leading edge of the bottom reflection. As a result, the bottom peak is displaced to the left and thus smaller depth estimates will be obtained. When the sea is deeper, the influence of the backscattered envelope on the bottom return is reduced. In this case, the displacement of the bottom peak is insignificant.

The trend shown in Fig. 3.6(a) is seen to confirm the above interpretation. Measurement d_{TS} is consistently less than d_{WD} because of the possible influence of the tailing of the envelope on the bottom return. A similar argument applies to the trend shown in Fig. 3.6(b). In this case, the waveforms are collected from an area with a different degree of sea turbidity. Consequently, the amplitude of the backscattered signal and its rate of decay are different. Specifically, the influence of the tail of the envelope extends more to the right of the waveform and can lead to a slight displacement of the bottom peak position to the left. An increase in sea depth results in a decrease of the interference and eventually the influence of the backscattered energy on the bottom return becomes insignificant. When sea depth ranges from 30 to 40 m, the bottom return is located further to the right and, therefore, its position is not influenced by the backscattered envelope. As a result, d_f no longer relates to sea depth. On the other hand, when sea depth ranges from 5 to 10 m, the temporal position of the bottom reflection is located immediately to the right of the surface reflection. The bottom return may interfere with the volumetric backscatter and, w overlap

PM-1 3½"x4" PHOTOGRAPHIC MICROCOPY TARGET
NBS 1010a ANSI/ISO #2 EQUIVALENT

1.0
1.1
1.25
1.4
1.6
1.8
2.0
2.2
2.5
2.8
3.2
3.6
4.0

PRECISION[SM] RESOLUTION TARGETS

with the surface reflection depending on the sea depth. As a result, the displacement of the bottom peak is more prominent when sea water is shallow, as indicated in Table 3.5.

3.4.2. Difference in depth estimates as a function of resolution

In the preceding section, the effect of sea depth on d_f has been examined. An alternative possibility is to examine the effect of resolution R_S on d_f. R_S has been defined in Eq. (2.22) and its value may depend on sea turbidity, sea depth, bottom composition of the ocean, roughness of the ocean surface, etc. In this comparison, we have crosstabulated R_S and $|d_f|$ in Table 3.6 where the three rows provide results for low, medium, and high resolutions. We observe that when the resolution is low, slightly more than half of the proportion of d_f are within 0.25 m or about 1 sample in the waveform. When the resolution is medium, the proportion becomes more than 80 %, and it increases to more than 90 % when the resolution is high. When the resolution is at least in the medium range, all of the differences are found to be within 0.5 m or about 2 samples in the waveform. When the resolution is low, about 6 % of d_f are not within 0.5 m. In general,

TABLE 3.6
DISTRIBUTION OF $|d_f|$ FOR DIFFERENT RANGES OF R_S
(NUMBERS SHOWN ARE ROW PERCENTAGES)

	$|d_f|$, m			
R_S	< 0.25	0.25 - 0.5	0.5 - 0.75	0.75 - 1.0
Low R_S: 0.3 - 0.5	56.6	37.6	4.0	1.8
Medium R_S: 0.5 - 0.75	83.0	17.0		
High R_S: 0.75 - 1.0	92.4	7.6		

the higher the resolution, the better the agreement between the two results, i.e., the difference in the two approaches becomes more explicit when the resolution is low.

Fig. 3.7(a), (b), (c) shows typical profiles of d_{WD}, d_{TS}, and d_f. The two profiles generated by d_{WD} and d_{TS} are highly correlated in all sea-depth ranges. We see, in addition, that d_{WD} is consistently larger than d_{TS} and that the difference d_f between the two profiles is progressively diminishing as the ocean becomes deeper, as may be expected from the above comparisons.

3.5 CONCLUSIONS

A waveform-decomposition procedure has been developed to decompose each LARSEN waveform into the surface and bottom reflections. The procedure involves the use of the Levenberg-Marquardt minimization algorithm with a trust-region approach in order to assure convergence from almost any starting point. An initialization scheme that leads to a reduction in the amount of computation in decomposition has also been proposed.

A comparative study of sea-depth estimates obtained with corresponding estimates obtained by a surveying company has then been performed. The differences between the two sets of results have been examined with respect to different ranges of sea depth and resolution.

Since the waveform parameters obtained through decomposition quantify the characteristics of the laser reflections, including the shape of the backscattered envelope, these parameters will be useful in number of applications. Firstly, it has been found that there exists a "propagation bias" [24] in sea-depth measurements obtained by using the LIDAR technology owing to the multiple scattering of photons in the water column. As discussed in [16], this bias can be estimated from the shape of the backscattered envelope, which can be deduced using the decomposition approach. Secondly, waveforms collected from different survey missions or areas can be compared systematically and the characteristics of the LIDAR signature can be studied in relation to variations of the optical properties of the sea as well as the changes in the ocean and weather conditions.

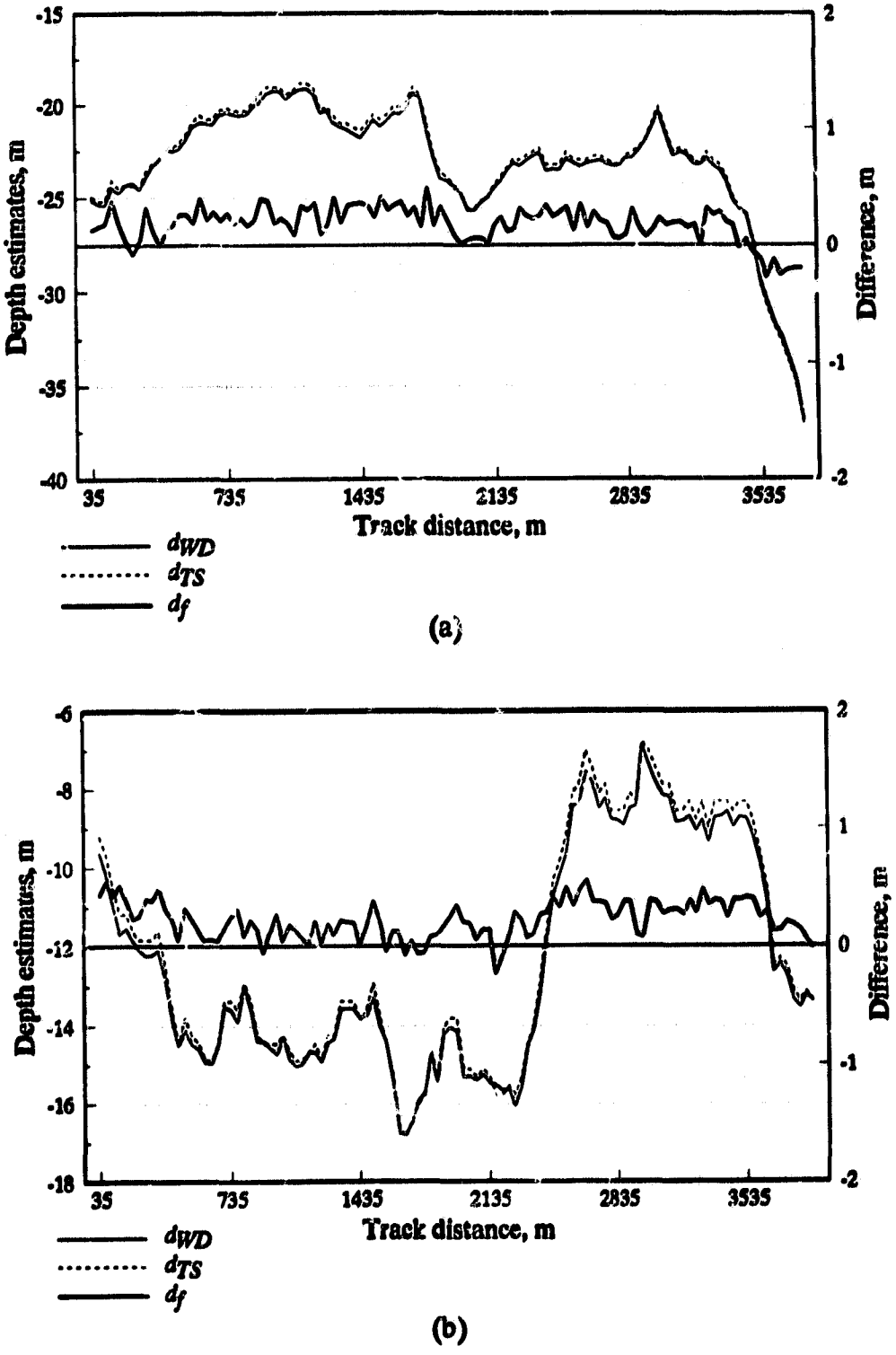

Fig. 3.7 Compare depth profiles: (a) moderately deep waters; (b) fairly rugged sea bottom, sea depth below 20 m.

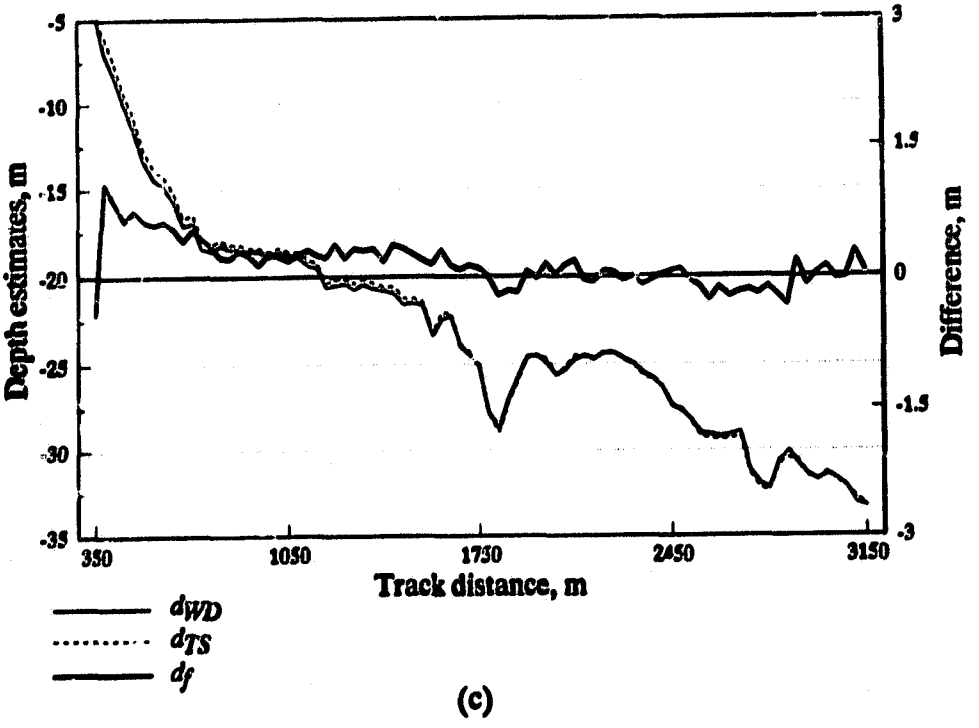

Fig. 3.7 Compare depth profiles: (c) fairly smooth sea bottom, sea depth increases from 5 to 35 m.

CHAPTER FOUR
TWO-DIMENSIONAL SIGNAL PROCESSING OF SCATTERED SEA-DEPTH ESTIMATES

4.1 INTRODUCTION

In laser bathymetry, noise embedded in sea-depth estimates can be broadly divided into two types. The first type of noise corrupts a laser waveform when it is collected at a sounding location. As a result of the application of 1-D signal processing techniques described in Chapters 2 and 3, the effects of this type of noise on the accuracy of sea-depth estimates are significantly reduced. The second type of noise is the noise inherent in the 2-D bathymetric profiles which is difficult to detect in individual waveforms, and, therefore, difficult to eliminate with 1-D processing. This type of noise generally depends on the positioning of laser soundings, sea state during survey missions, and the measurement errors of the LIDAR system. Specifically, the geographical position of each laser sounding is dependent upon the laser-firing angle, aircraft position, and altitude information. Measurement inaccuracies due to one or more of these factors contributes uncertainties in the laser-sounding location and this, in turn, gives rise to uncertainties in the depth estimates at the recorded geographical positions. Another type of error inherent in the bathymetric profiles is associated with the condition of sea. The world's oceans are rarely calm and when the wind is strong during a survey, white caps and foam patches begin to form and this may lead to altitude errors measured from the aircraft as well as errors in sea depths estimated on the basis of the time delay between the surface and bottom reflections. On the other hand, measurement errors inherent in the LIDAR system may produce a range bias or offset in the bathymetric measurements. All of these errors combine to form a noise component and since these errors are random in nature, they can be approximated as wideband noise in the bathymetric data set.

Another type of error, which is difficult to detect in 1-D processing, manifests itself in a totally different form in a bathymetric profile. This type of error is often caused by false returns from the ocean, i.e., laser pulses are reflected by objects other than ocean bottom, for example, fish shoals. In addition, laser reflections from the ice mass are also quite common in the bathymetric survey missions in places such as the Canadian Central Arctic. Since the sea depths estimated from the waveforms received under these circumstances can be very different from the actual depths, considerable errors, which are in the form of impulsive noise, may result if further processing of the bathymetric profiles is not applied.

In this chapter, we introduce a type of 2-D interpolating filters for the elimination of impulsive noise and in Chapter 5 we will describe two different methods developed for eliminating wideband noise in the profiles. The reason for dealing with the problem of impulsive noise first is that the processing techniques developed for the removal of wideband noise require the conversion of the scattered depth estimates into a regular grid of data. If the impulsive noise is not removed from the scattered depth estimates, the estimates on the constructed regular grid located close to the impulsive noise components can be significantly affected and, thereby, seriously degrade the representation of the sea-bed topography.

A sophisticated 2-D interpolation technique that can be used to convert scattered data points into a regular grid of data will be discussed in this chapter. With the application of this interpolation technique, sea-bed topography can be reconstructed from irregularly spaced data points and, therefore, can eventually be represented in the form of contour maps or represented as 3-D surfaces for perspective view. The 2-D interpolation technique may also be used to construct maps of various resolutions for different application needs.

In Chapter 3 we have performed a comparative study in detail to examine our 1-D processing results by comparing these results with those obtained by a surveying company. However, in cases where the resolution of laser reflections in the waveforms is very low, the depth estimates are not available from the surveying company. In order to assess the accuracy of our 1-D processing results obtained under these circumstances, we will complete the comparative study in this chapter by describing a procedure which incorporates the 2-D interpolation technique.

To facilitate 2-D interpolation, 2-D geometric transformations must be carried out on the position of each sounding. This topic will be addressed in Section 4.2. A 2-D interpolation method designed to suppress undulations in the resulting surfaces will then be derived in Section 4.3. In Section 4.4, we discuss the filtering of impulsive noise. The application of the interpolation method to assess the accuracy of our 1-D results under the very-low resolution conditions will be illustrated in Section 4.5.

4.2 AFFINE TRANSFORMATIONS

The direction of a flight line is mainly dependent upon the geographical location of the surveyed area and, therefore, it varies in survey missions. When the aircraft is flying along the track in a particular direction, the sounding pattern generated on the surface of the ocean has an orientation which is related to the flight direction. Fig. 4.1 shows the sounding pattern of a particular flight path in one of the LARSEN survey missions. As shown in the figure, the position of each sounding can be represented by x and y coordinates. In order to provide a convenient way for performing 2-D interpolation and filtering in this chapter as well as 2-D processing in the next chapter affine transformations are usually carried out. There are three distinct transformations — translation, rotation, and scaling of coordinates applied in sequence. To illustrate this, we refer to Fig. 4.1 again. For the purpose of illustration, only ten sweeps of laser soundings projected along a single track are shown in the figure. Each sweep or arc shown

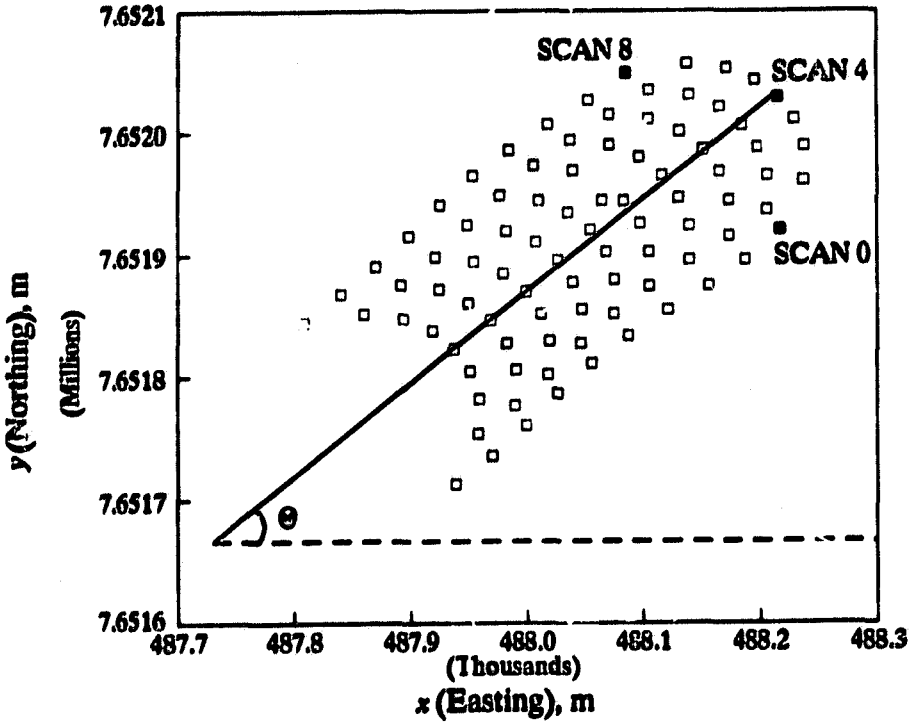

Fig. 4.1 Projections of laser soundings on the surface of the ocean.

consists of nine laser soundings which can be numbered from scan 0 to scan 8. In order to determine the direction of the flight line, a straight line is fitted through all soundings of a particular scan number in the least-squares sense (scan 4 was chosen in this figure). The slope of the least-squares line is then used to determine the angle θ as shown in the figure. With the angle θ known, we can define a translated and rotated Cartesian-coordinate system, say the $x'-y'$ system shown in Fig. 4.2. In this case, x' is the along-track coordinate and y' is the across-track coordinate. When the grid-point coordinates are specified in the (x', y') form, a rectangular grid can be generated from the irregularly spaced data using 2-D interpolation.

Different flight directions require different orientations of the coordinate system to be set up to generate rectangular grids. However, if we restrict ourselves to using only one orientation of the Cartesian-coordinate system regardless of flight directions, we can apply appropriate geometric rotation to the coordinates of the irregularly spaced data in Fig. 4.1 to obtain the same results. Fig. 4.3 shows the data with transformed coordinates using the transformation equation

$$[p'] = [p]\,[T(T_x, T_y)]\,[R(\alpha)]\,[S(S_f)] \tag{4.1}$$

where

$$[p'] = [x' \;\; y' \;\; 1]$$

represents the transformed sounding location expressed in the homogeneous-coordinate form [50],

$$[p] = [x \;\; y \;\; 1]$$

represents the original sounding location expressed in the same form, and

$$[T(T_x, T_y)] = \begin{bmatrix} 1 & 0 & 0 \\ 0 & 1 & 0 \\ -T_x & -T_y & 1 \end{bmatrix}$$

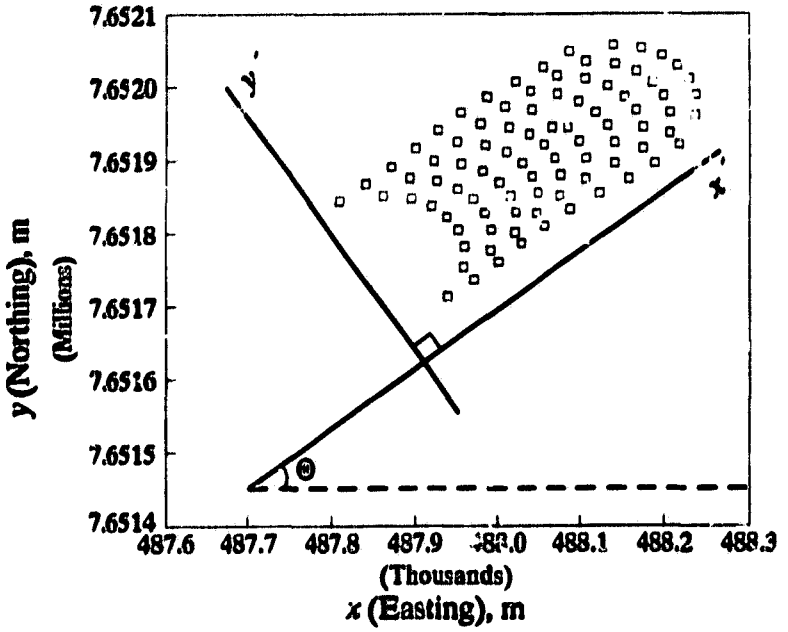

Fig. 4.2 Translation and rotation of the x-y coordinate system to form the x'-y' coordinate system.

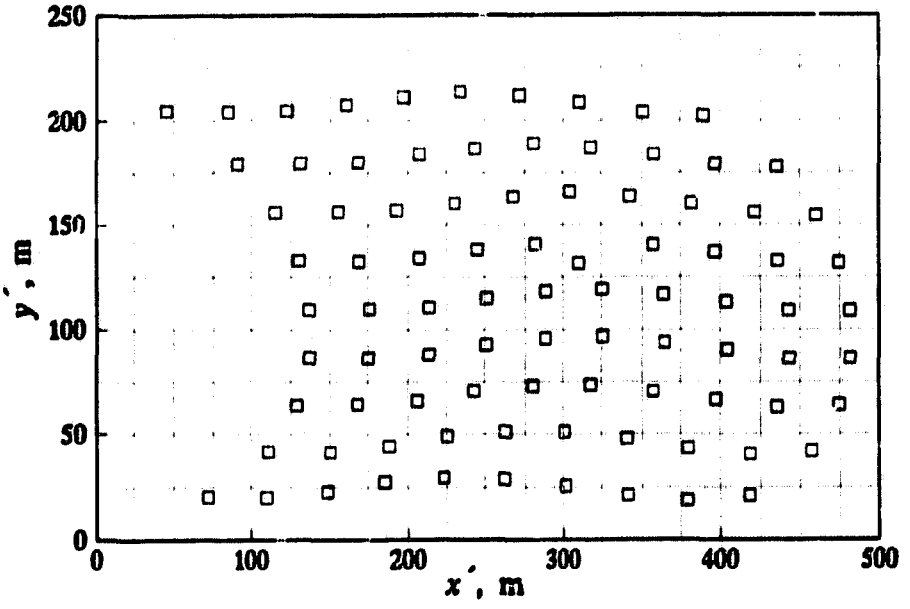

Fig. 4.3 Sounding locations after affine transformations.

represents the translation matrix with translation distances T_x and T_y in the x and y directions, respectively. The matrix

$$[R(\alpha)] = \begin{bmatrix} \cos\alpha & \sin\alpha & 0 \\ -\sin\alpha & \cos\alpha & 0 \\ X_R(1-\cos\alpha) + Y_R\sin\alpha & Y_R(1-\cos\alpha) - X_R\sin\alpha & 1 \end{bmatrix}$$

represents the matrix for rotation about (X_R, Y_R) and α is the angle of rotation determined from θ in Fig. 4.1. Since the rotation in this example is clockwise, $\alpha = -\theta$. The matrix

$$[S(S_f)] = \begin{bmatrix} S_f & 0 & 0 \\ 0 & S_f & 0 \\ 0 & 1 & 1 \end{bmatrix}$$

represents the transformation matrix for scaling with the scaling factor S_f. Note that the same scaling factor is applied to both the x and y coordinates so that the spatial relationship of the depth estimates can be preserved after transformations.

To generate a rectangular grid using the data points in Fig. 4.3, grid-point coordinates (x', y') must be specified. Moreover, a boundary must be set up to enclose the grid points so that the function values at the grid points are approximated from neighboring points through the use of 2-D interpolation, not 2-D extrapolation. Extrapolation is not used to approximate sea depths because it does not lead to a high degree of accuracy. If the interpolating function presented in the next section is used for extrapolation, unreliable estimates would be obtained especially when the grid points are away from the boundary.

4.3 2-D INTERPOLATION USING TRIANGULATED-IRREGULAR NETWORKS

Various 1-D interpolation techniques can be used for the estimation of 1-D function values at arbitrary points and by far the most common technique is polynomial interpolation. In some practical problems,

however, the use of polynomial interpolation gives unsatisfactory results and is, therefore, not suitable. For example, in order to interpolate tabular data, it may be necessary to use a fairly high-degree polynomial. Polynomials of high degree often have a very oscillatory behavior which is undesirable in estimating function values that are smooth in nature.

An alternative approach is to use piecewise polynomial interpolation. Here, several lower-degree polynomials are joined together in a continuous fashion so that the resulting piecewise polynomial interpolates the data. Unfortunately, the resulting curve often suffers from a lack of smoothness and has discontinuous derivatives if no continuity conditions are imposed at the endpoints. Thus, piecewise polynomial interpolation is not well-suited for approximating most of the functions which arise in physical problems, since such functions are usually fairly smooth. To overcome the oscillatory behavior of polynomials and still provide a smooth approximation, an interpolation technique using splines has been used extensively. The resulting curve traced out by the spline has the property that it interpolates the function at each data point and, furthermore, it smooths out as much as possible between the points. Thus, the oscillatory behavior of the approximation is minimized.

Like polynomial interpolation, spline functions can be easily extended to two-dimensional form to perform 2-D interpolation. However, 2-D interpolation using these techniques is usually performed at the vertices of a rectangular grid. The problem of interpolating on a mesh that is not Cartesian, i.e., one that has tabulated function values at "random" points in 2-D space, is not often addressed.

To overcome this difficulty, triangle-based interpolation has gained widespread use particularly in describing the topography of the terrain. Early computer algorithms for 2-D interpolation over a triangular mesh were direct implementation of methods used by surveyors for the hand mapping of topography [51]. In these algorithms, data points are first connected by straight lines to form a mesh of

triangles and the resulting surface is modeled as a combination of a series of flat, triangular planes. There are two major shortcomings of using this type of algorithms in 2-D interpolation. First, the triangles thus formed may be "thin", i.e., the length of one side can be very different from that of the other two sides. Thin triangles generally are not preferred because they usually give rise to fairly inaccurate interpolation results. Secondly, the approximation of a surface, particularly for representing the ocean bathymetric data, by a combination of flat planes is a very crude approximation.

Various algorithms have been developed to improve the triangulation procedure [52]-[56] and attempts have been made to construct a unique, "optimal" set of triangles from the scattered data. An optimal set of triangles implies that the individual triangles should be as close to equiangular as possible, or that the longest side of each triangle should be as short as possible. It has been shown that by using the local optimization procedure introduced by Lawson [57] in triangulation, the resulting triangulation becomes a Delaunay triangulation [58], indicating that the triangles formed are as nearly equiangular as possible [59]-[60]. As a result of this desirable property, this procedure has been adopted for the triangulation of the scattered laser soundings.

The procedure described in [57] utilizes a criterion, known as the max-min angle criterion, to triangulate a quadrilateral. Specifically, let Q be a strictly convex quadrilateral made up of four data points so that each of its four interior angles is less than 180 degrees. In such a case, precisely two different triangulations, denoted by Γ and Γ', respectively, can be performed on Q. Let T denote a triangle and $a(T)$ be the minimum angle in T. Further, let $a(\Gamma) = \min \{a(T): T \in \Gamma\}$ be the minimum angle of the two triangles in the triangulation Γ. The max-min angle criterion states that the triangulation Γ should be selected if

$$a(\Gamma) > a(\Gamma')$$

In other words, Q should be triangulated in such a way that the final triangulation maximizes the minimum interior angle of the two resulting triangles.

To construct a triangular network that satisfies the max-min angle criterion, one can first quickly construct an initial triangulation and then swap triangles whenever necessary [52]. A more efficient approach that is adopted here is to start with one triangle and then add one data point at a time so as to maintain that the current network is locally optimal [58].

Although interpolation by fitting planar facets to each triangle is a fast and economical method, the interpolated surface has an undesirable jagged appearance and can misrepresent the bathymetric surface to a very large extent. A better approximation to the surface can be achieved by using curved or bent triangular plates, i.e., fitting a smooth curved surface over each triangle by using a low-order bivariate polynomial. For instance, one of the earliest methods involves finding three closest neighbors of each triangle and then fitting a second-order bivariate polynomial to these three data points and to the three vertices of the triangle. The resulting polynomial will pass through all these six data points and it may then be used to evaluate the elevation at a series of locations within the triangle. The surface constructed in such a way usually has abrupt changes across the boundaries of the triangles and, therefore, gradient information is generally used in formulating the polynomial so that the slope also changes smoothly from one triangle to the next, i.e., to provide C^1 continuity in the triangular mesh.

A more sophisticated approach is to perform interpolation on the basis of the finite-element method (FEM). One procedure is to model the surface over each triangle as a "tricubic polynomial" as defined in [61]. There are nine coefficients in the polynomial and the values of these coefficients are determined not only from the values but also from the first-order partial derivatives at the vertices of a triangle. The derivatives are estimated by using a least-squares procedure. With the use of this

interpolation method, C^1 continuity can be achieved in the resulting surface [62]. Another triangular-based interpolation that is based on an FEM is discussed in [57]. This method involves the partitioning of each triangle into three subtriangles by drawing internal boundaries from the centroid to each vertex of the triangle, a cubic polynomial in both x and y is then used to model the surface within each subtriangle [63]. By using this method, C^1 continuity is assured across internal and external boundaries of the triangle.

A different approach to applying the FEM in approximating the surface over a triangular region is discussed by Zlámal [64]. In this approach, a bivariate 5th-degree polynomial is constructed over each triangular cell. The coefficients of the polynomial are uniquely defined by the given z values of the data, as well as the first- and second-order partial derivatives at certain points, called nodes, on the boundary of the triangular cell. It was proved by Zlámal that by using this method in constructing a surface over the triangulated domain, C^1 continuity can be assured. In addition, the polynomials have piecewise continuous second-order derivatives. The procedure can be briefly described as follows.

For each triangular cell T, let P_l, $l = 1, 2, 3$ be the vertices of T and Q_l, $l = 1, 2, 3$ be the midpoints of the sides of T. To estimate the function value $z(x,y)$ at any point $P(x,y)$ in T, a 5th-degree polynomial in both x and y is used, i.e.,

$$z(x,y) = \sum_{j=0}^{5} \sum_{k=0}^{5-j} q_{jk} x^j y^k \tag{4.2}$$

where q_{jk} are the coefficients of the polynomial to be determined using the z values and $\partial z/\partial x$, $\partial z/\partial y$, $\partial^2 z/\partial x^2$, $\partial^2 z/\partial y^2$, and $\partial^2 z/\partial x\,\partial y$ (or denoted as z_x, z_y, z_{xx}, z_{yy}, and z_{xy} respectively) at P_l. In addition, three normal derivatives $\partial z(Q_l)/\partial v$ are also required in determining q_{jk} where v is the normal to the side of T. The theory was generalized by Ženíšek [65] to $(4m+1)$th-degree

polynomials. Conditions uniquely determining a polynomial of the degree $4m+1$ are given in [65]. These conditions are set up so that functions generated are m-times continuously differentiable on a triangulated closed domain.

The approximation procedure discussed by Zlámal will now be adopted for 2-D interpolation of scattered sea-depth estimates. Since the resulting representative surface formed will be based on a collection of local parametric surfaces, which are represented by the bivariate 5th-degree polynomials, the local details of the topography can be expressed. In effect, the resulting bathymetric surface will be dominated by local trends in the data. Since both the first- and second-order derivatives are utilized in evaluating the parametric surface, the local slope, convexity, and concavity of local topography will be accurately revealed and, thereby, giving a clear indication of the pronounced trends and anomalies in the data.

In the following sections, we will describe the 2-D interpolation procedure. Conditions set up to ensure the smoothness of the interpolated values are first examined. Next, a method for the estimation of partial derivatives at the vertex of each triangle is described. Procedures for determining the coefficients of the fifth-degree polynomials are then presented and interpolation results are provided.

4.3.1 Continuity considerations in 2-D interpolation

In this section, the continuity of the interpolating function is discussed. It is shown that if certain conditions are satisfied, the interpolating surface along the side of the triangle is smooth.

The interpolating function is a smooth function when the interpolating function and its first-order partial derivatives are continuous on the boundaries of the triangular cells. To demonstrate this, a rotated Cartesian-coordinate system, namely, the s-t system is introduced [66]. In the s-t system, the s axis is parallel to one side of the triangle. Since the coordinate transformation between the x-y system

and the s-t system is linear, the partial derivatives z_x, z_y, z_{xx}, z_{yy}, and z_{xy} at each vertex of the triangle uniquely determine the values of z_s, z_t, z_{ss}, z_{tt}, and z_{st} at the corresponding vertex. As the s axis is parallel to one side, say side P_jP_k, of the triangle, the values of z, z_s, and z_{ss} at the two ends of P_jP_k uniquely determine a fifth-degree polynomial in s on the side P_jP_k.

Since P_jP_k is the common side shared by two adjacent triangles, the two fifth-degree polynomials determined from z, z_s, and z_{ss} at the ends of P_jP_k coincide. The interpolated values along the side P_jP_k given by the two polynomials are therefore the same and this proves the continuity of the interpolating function along a side of a triangle.

In order to maintain the continuity of the first derivative along each side of a triangle Akima [66] has imposed a condition that the first-order partial derivatives of the interpolating function in a direction normal to each side of a triangle is a polynomial of degree three at most in the variable measured in the direction of the side of the triangle. In other words, z_t is a polynomial of degree three at most in s. Equivalently, the condition

$$z_{tssss} = 0 \tag{4.3}$$

must be satisfied at each side of the triangle.

The proof of the continuity of z_t along the side of the triangle is similar to the proof of the continuity of the interpolated values as mentioned earlier. Here, the values of z_t and z_{ts} at the ends of a side, say side P_jP_k, uniquely determine a polynomial z_t of degree three in s on P_jP_k. Again, since P_jP_k is the common side shared by the two triangles, the two polynomials of degree three in s determined from z_t and z_{ts} at the ends of P_jP_k coincide. This proves the continuity of z_t along a side of a triangle. Since the interpolating function has continuous derivatives at the boundaries of each triangle, smoothness of the resulting surface is assured.

4.3.2 Estimation of partial derivatives

This section deals with the estimation of partial derivatives locally at the vertex of each triangle. The partial derivatives estimated are not unique and the accuracy of the estimation generally varies from method to method. One method which is formulated as a local least-squares problem is described in [57]. In this method, a bivariate quadratic polynomial which consists of six coefficients is fitted to the z value at a vertex P_0 and the z values of its 16 immediate neighbors. The polynomial is forced to interpolate the z value at P_0 and it fits the remaining points in a weighted least-squares sense. The first-order partial derivatives of the polynomial evaluated at P_0 then give $\partial z/\partial x$ and $\partial z/\partial y$ at P_0. The amount of computation required by this method is large and it provides only the first-order derivatives. Furthermore, the approach is somewhat ad hoc.

A preferred method which is adopted in our case for the estimation of partial derivatives in the scattered data points is described in [66]. First, the method is applied to the z values to estimate z_x and z_y at each data point and the same method is then applied to the first derivatives obtained to estimate z_{xx}, z_{yy}, and z_{xy}.

Let the projections of the data points D_i, $i = 0, 1, 2, .., n$ be P_i, $i = 0, 1, 2, .., n$ in the x-y plane. In order to estimate z_x and z_y, we first construct vectors D_0D_j and D_0D_k, $j, k = 1, 2, .., n$ and form cross products of D_0D_j and D_0D_k $(j \neq k)$ in such a way that the z component of the cross product is always positive. Then we take a vector sum S of all the vector products. Lastly, we construct a plane normal to S and estimate z_x and z_y of the data point D_0 at P_0 by differentiating the function representing the plane.

To estimate z_{xx} and $(z_x)_y$ at P_0, we apply the same procedure as previously described except that the estimated z_x values instead of the z values of the data points are used in constructing the

vectors D_0D_j and D_0D_k. Similarly, to estimate z_{yy} and $(z_y)_x$ at P_0, we replace the z values with the z_y values when constructing vectors D_0D_j and D_0D_k. The average of $(z_x)_y$ and $(z_y)_x$ previously computed becomes the estimate of z_{xy} at P_0.

The number of closest neighboring points of P_0 is chosen to be four, which is within the preferred range as suggested in [66], in the estimation of partial derivatives at P_0. The procedure described above involves the use of the direction of the cross product of two vectors D_0D_j and D_0D_k and, therefore, it fails when the data points are collinear. Should this happen, the data point D_n which has the projection P_n furthest from P_0 can be replaced by another data point which is not collinear with the present data and has the projection next closest to P_0.

4.3.3 Determination of coefficients of the bivariate polynomial

The function value $z(x, y)$ at any point $P(x, y)$ in a triangle can be interpolated by the bivariate fifth-degree polynomial of Eq. (4.2). In this section, the required twenty-one coefficients q_{jk} will be determined. To determine these coefficients, twenty-one independent conditions must be set up. In Section 4.3.1, the condition in Eq. (4.3) must be satisfied at each side of the triangle. Since a triangle has three sides, three conditions can be set up. In Section 4.3.2, we estimated the five partial derivatives z_x, z_y, z_{xx}, z_{yy}, and z_{xy} at each vertex of the triangle. As a result, fifteen conditions can be set up at the three vertices of the triangle. The remaining three conditions can be set up using the z values of the data at the three vertices of the triangle.

To facilitate the determination of the coefficients, a procedure given in [67] is adopted. First, a new coordinate system, the u-v system, is set up to simplify the representation of a triangular cell. From the relationship between the x-y system and the u-v system, the five partial derivatives z_u, z_v, z_{uu}, z_{vv} and z_{uv} at each vertex of the triangle can be obtained. The polynomial in Eq. (4.2) is then

expressed in terms of u and v. The condition set up in Section 4.3.1 for each side of the triangle is first used to set up relationships among the coefficients of this newly-formed polynomial. With the remaining eighteen conditions, the coefficients of the polynomial can finally be determined.

The u-v coordinate system is set up as shown in Fig. 4.4(a) and the vertices P_l, $l = 1, 2, 3$ of the triangle are located at points $(0,0)$, $(1,0)$ and $(0,1)$. Fig. 4.4(b) shows the corresponding description in the Cartesian-coordinate system. The coordinate transformation between the two systems is determined by the relationships

$$\begin{aligned} x &= au + bv + x_1 \\ y &= cu + dv + y_1 \end{aligned} \tag{4.4}$$

where

$$\begin{aligned} a &= x_2 - x_1 \\ b &= x_3 - x_1 \\ c &= y_2 - y_1 \\ d &= y_3 - y_1 \end{aligned} \tag{4.5}$$

Using Eq. (4.4), u and v can be expressed in terms of x and y as

$$\begin{aligned} u &= \frac{d(x - x_1) - b(y - y_1)}{(ad - bc)} \\ v &= \frac{-c(x - x_1) + a(y - y_1)}{(ad - bc)} \end{aligned} \tag{4.6}$$

Using the same equation, the partial derivatives in the x-y system can be transformed to those in the u-v system. For example, z_u can be expressed as

$$\frac{\partial z}{\partial u} = \frac{\partial z}{\partial x}\frac{\partial x}{\partial u} + \frac{\partial z}{\partial y}\frac{\partial y}{\partial u}$$

or

$$z_u = az_x + cz_y$$

Similarly, other first- and second-order derivatives are obtained as

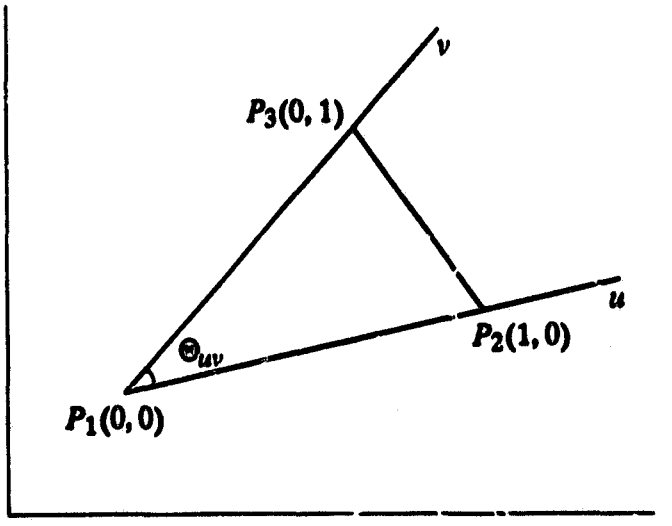

(a)

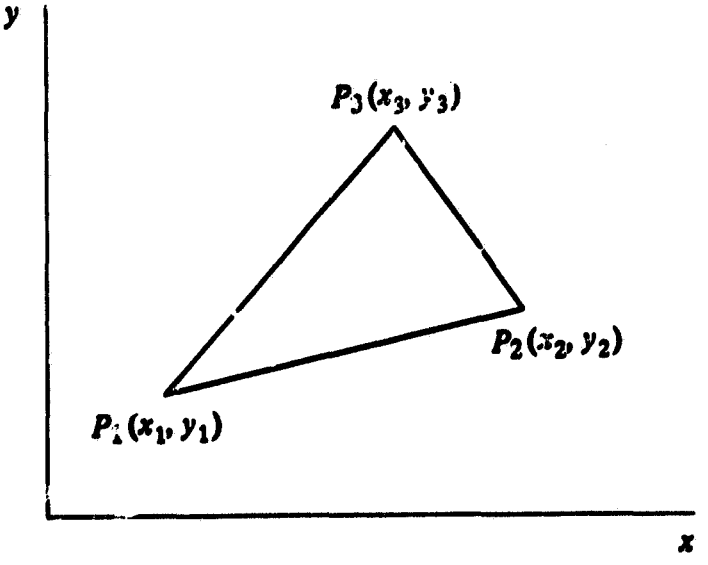

(b)

Fig. 4.4 Geometric description of a triangle: (a) the u–v coordinate system; (b) the x–y Cartesian-coordinate system.

$$
\begin{aligned}
z_v &= bz_x + dz_y \\
z_{uu} &= a^2 z_{xx} + 2ac\, z_{xy} + c^2 z_{yy} \\
z_{vv} &= b^2 z_{xx} + 2bd\, z_{xy} + d^2 z_{yy} \\
z_{uv} &= ab\, z_{xx} + (ad + bc)\, z_{xy} + cd\, z_{yy}
\end{aligned}
$$

Since z_x, z_y, z_{xx}, z_{yy}, and z_{xy} can be determined using the method described in Section 4.3.2, we can readily solve for z_u, z_v, z_{uu}, z_{vv}, and z_{uv} using the above equations.

To express the fifth-degree polynomial $z(x,y)$ in Eq. (4.2) in terms of u and v, we can write

$$
z(u,v) = \sum_{j=0}^{5} \sum_{k=0}^{5-j} p_{jk}\, u^j v^k \tag{4.7}
$$

Note that Eq. (4.7) is also a fifth-degree polynomial as the coordinate transformation between the x-y and u-v coordinate systems is linear. As a result of this transformation, the 21 coefficients p_{jk} of Eq. (4.7) can be determined.

First, we consider the smoothness condition as expressed by Eq. (4.3). To utilize this condition, we rotate the s-t system as discussed in Section 4.3.1 in such a way that the s axis is parallel to each side of the triangle. Fig. 4.5(a), (b), and (c) refer to cases where the s axis is parallel to the sides P_1P_2, P_1P_3, and P_2P_3, respectively. Consider the case where the s axis is parallel to the side P_1P_2. In this case, the coordinate transformation between the s-t system and the u-v system is given by

$$
\begin{aligned}
u &= \frac{\sin\theta_{uv}\,(s - s_0) - \cos\theta_{uv}\,(t - t_0)}{L_u \sin\theta_{uv}} \\
v &= \frac{t - t_0}{L_v \sin\theta_{uv}}
\end{aligned} \tag{4.8}
$$

where (s_0, t_0) is the vertex position of P_1,

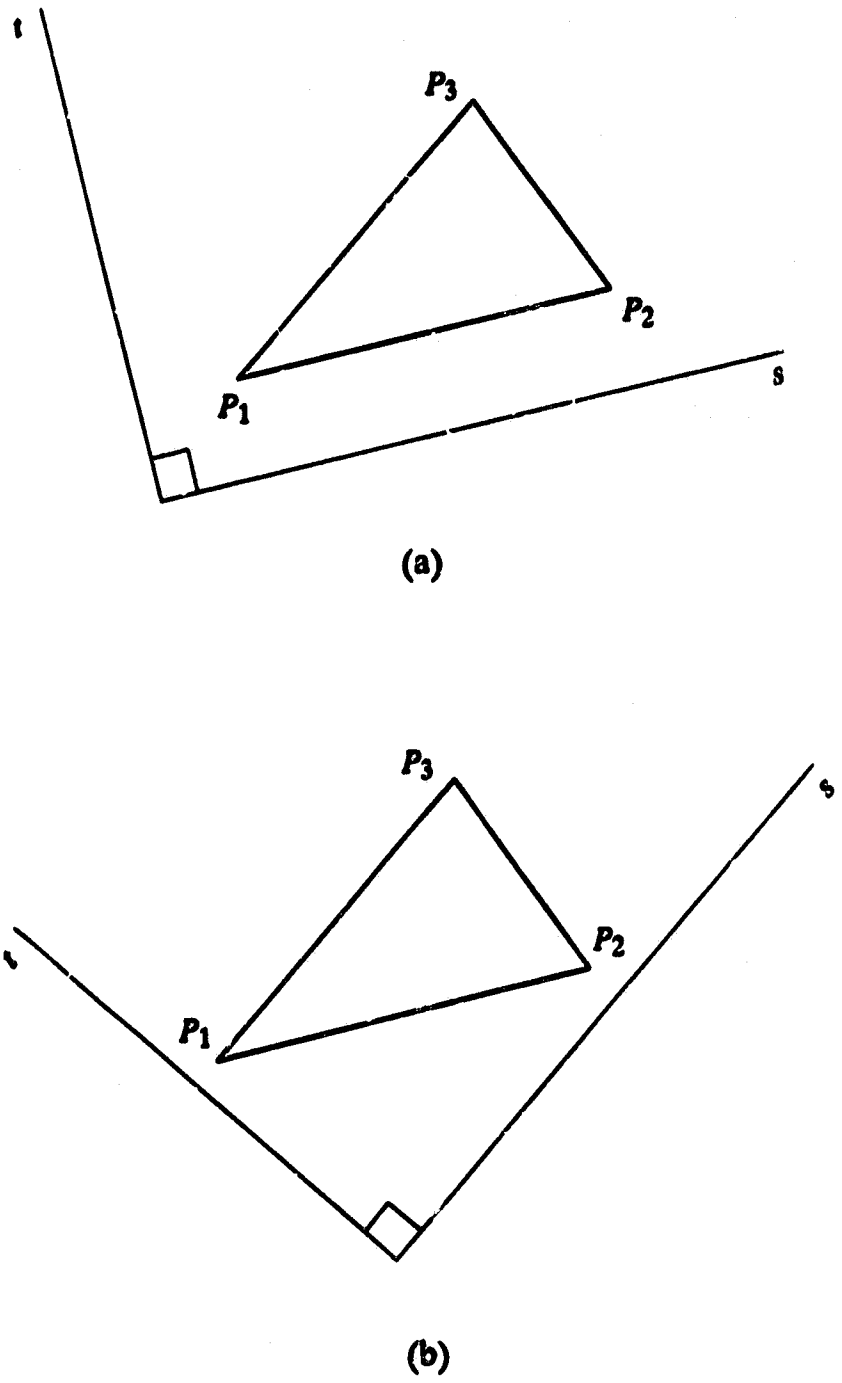

Fig. 4.5 Geometric rotation of the s-t system: (a) the s axis is parallel to the side P_1P_2; (b) the s axis is parallel to the side P_1P_3.

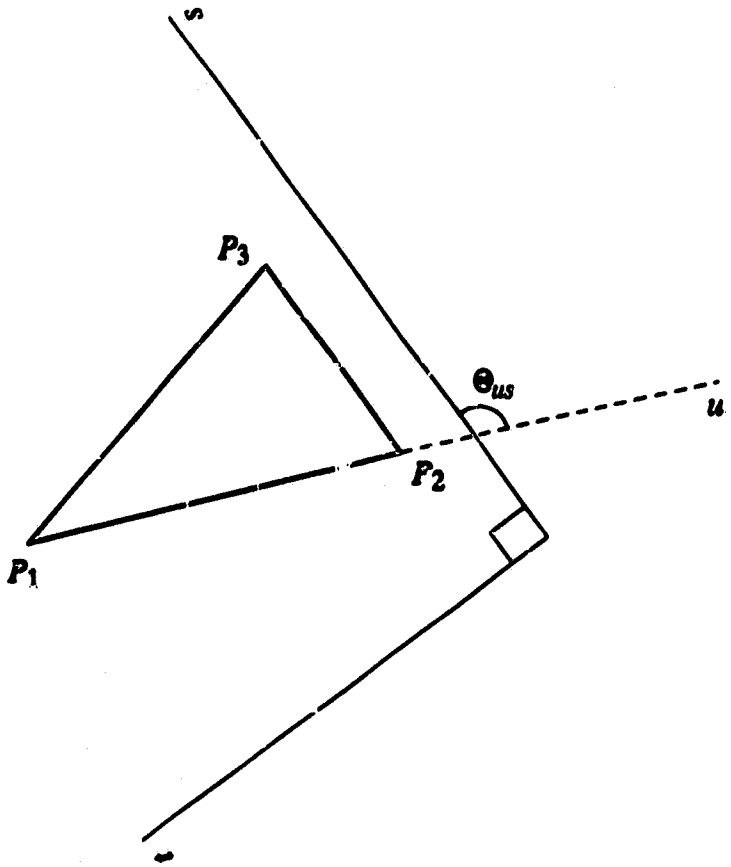

(c)

Fig. 4.5 Geometric rotation of the $s-t$ system: (c) the s axis is parallel to the side P_2P_3, θ_{us} is the angle between the u axis and the s axis.

$$L_u = \sqrt{a^2 + c^2}$$

$$L_v = \sqrt{b^2 + d^2}$$

$$\theta_{uv} = \tan^{-1}\left(\frac{d}{b}\right) - \tan^{-1}\left(\frac{c}{a}\right)$$

and a, b, c, and d are the geometrical constants given in Eq. (4.5). Using Eq. (4.8), partial differentiation of $z = z(u, v)$ in Eq. (4.7) with respect to t gives

$$\begin{aligned}\frac{\partial z}{\partial t} &= \frac{\partial z}{\partial u}\frac{\partial u}{\partial t} + \frac{\partial z}{\partial v}\frac{\partial v}{\partial t} \\ &= -\frac{\cos\theta_{uv}}{L_u \sin\theta_{uv}} z_u + \frac{1}{L_v \sin\theta_{uv}} z_v\end{aligned} \tag{4.9}$$

The partial derivative with respect to s using Eq. (4.8) is given by

$$\begin{aligned}\frac{\partial z}{\partial s} &= \frac{\partial z}{\partial u}\frac{\partial u}{\partial s} + \frac{\partial z}{\partial v}\frac{\partial v}{\partial s} \\ &= \frac{1}{L_u}\frac{\partial z}{\partial u}\end{aligned} \tag{4.10}$$

If we partially differentiate Eq. (4.9) four times with respect to s using Eq. (4.10), we obtain

$$z_{tssss} = \frac{1}{L_u^4}\left(\frac{-\cos\theta_{uv}}{L_u \sin\theta_{uv}} z_{uuuuu} + \frac{1}{L_v \sin\theta_{uv}} z_{vuuuu}\right) \tag{4.11}$$

Two derivatives, namely, z_{uuuuu} and z_{vuuuu}, can be obtained by partially differentiating the polynomial z_{uv} in Eq. (4.7) with respect to u and v and their values are

$$\begin{aligned}z_{uuuuu} &= 120 p_{50} \\ z_{vuuuu} &= 24 p_{41}\end{aligned} \tag{4.12}$$

Substituting Eq. (4.12) into Eq. (4.11) and letting $z_{tssss} = 0$, we get

$$L_u p_{41} - 5 L_v \cos\theta_{uv}\, p_{50} = 0 \tag{4.13}$$

In effect, a relation between polynomial coefficients p_{41} and p_{50} is obtained.

The result obtained for the case when the s axis is parallel to the side P_1P_3 can be similarly derived. In this case,

$$z_{tssss} = \frac{1}{L_v^4}\left(\frac{-1}{L_u \sin\theta_{uv}} z_{uvvvv} + \frac{\cos\zeta_{uv}}{L_v \sin\theta_{uv}} z_{vvvvv}\right) \tag{4.14}$$

and the derivatives are obtained as

$$\begin{aligned} z_{uvvvv} &= 24 p_{14} \\ z_{vvvvv} &= 120 p_{05} \end{aligned} \tag{4.15}$$

After substituting Eq. (4.15) into Eq. (4.14) and letting $z_{tssss} = 0$, we get

$$L_v p_{14} - 5 L_u \cos\theta_{uv}\, p_{05} = 0 \tag{4.16}$$

The result obtained for the case where the s axis is parallel to the side P_2P_3 is slightly more complex and is given by

$$\begin{aligned} &5A^4 B p_{50} + A^3(4BC + AD) p_{41} + A^2 C(3BC + 2AD) p_{32} \\ &+ AC^2(2BC + 3AD) p_{23} + C^3(BC + 4AD) p_{14} \\ &+ 5C^4 D p_{05} = 0 \end{aligned} \tag{4.17}$$

where

$$\begin{aligned} A &= \frac{\sin(\theta_{uv} - \theta_{us})}{L_u \sin\theta_{uv}} \\ B &= -\frac{\cos(\theta_{uv} - \theta_{us})}{L_u \sin\theta_{uv}} \\ C &= \frac{\sin\theta_{us}}{L_v \sin\theta_{uv}} \\ D &= \frac{\cos\theta_{us}}{L_v \sin\theta_{uv}} \\ \theta_{us} &= \tan^{-1}\left(\frac{d-c}{b-a}\right) - \tan^{-1}\left(\frac{c}{a}\right) \end{aligned} \tag{4.18}$$

with constants a, b, c, and d defined in Eq. (4.5).

Some of the coefficients of z_{uv} are interrelated by Eq. (4.13), (4.16), and (4.17). In order to determine their actual values as well as the values of the remaining coefficients, we proceed as follows.

First, we partially differentiate $z(u,v)$ in Eq. (4.7) with respect to u and v. The five partial derivatives are then obtained as

$$
\begin{aligned}
z_u(u,v) &= \sum_{j=1}^{5} \sum_{k=0}^{5-j} j\, p_{jk}\, u^{(j-1)} v^k \\
z_v(u,v) &= \sum_{j=0}^{4} \sum_{k=1}^{5-j} k\, p_{jk}\, u^j v^{(k-1)} \\
z_{uu}(u,v) &= \sum_{j=2}^{5} \sum_{k=0}^{5-j} j(j-1)\, p_{jk}\, u^{(j-2)} v^k \\
z_{vv}(u,v) &= \sum_{j=0}^{3} \sum_{k=2}^{5-j} k(k-1)\, p_{jk}\, u^j v^{(k-2)} \\
z_{uv}(u,v) &= \sum_{j=1}^{4} \sum_{k=1}^{5-j} jk\, p_{jk}\, u^{(j-1)} v^{(k-1)}
\end{aligned}
\tag{4.19}
$$

Next we evaluate z_{uv} in Eq. (4.7) and its partial derivatives in Eq. (4.19) at the three vertices of the triangle. In other words, we substitute $(u,v) = (0,0), (0,1), (1,0)$ in turn into Eqs. (4.7) and (4.19). Since the values at the left-hand side of Eqs. (4.7) and (4.19) are known quantities, we obtain a set of algebraic equations involving the unknown coefficients p_{jk}. From Eqs. (4.13), (4.16) and (4.17) together with this set of equations, we can, therefore, solve for all p_{jk} in Eq. (4.7). Since the procedure is noniterative, the coefficients can be found quite efficiently.

4.3.4 Interpolation results

In order to test the performance of the 2-D interpolation technique described in this chapter, we will apply it to three cases corresponding to bathymetric information obtained in three different areas. In case (i), we apply the technique to one hundred irregularly spaced data points collected from an area where the depth of the ocean ranges from 26 m to 34 m. In cases (ii) and (iii), we apply the technique to the same number of data points collected from areas where depths vary from 7.2 m to 8.6 m and

2 m to 12 m, respectively. The 3-D surface and contour plots of the interpolated results are given in each case.

As mentioned earlier, in order to perform 2-D interpolation, the x-y plane consisting of the sounding positions must be partitioned into a number of triangles. Fig. 4.6 shows the results of the triangular grid constructed on the x-y plane in Fig. 4.3. There are 144 triangles constructed in Fig. 4.6 and many of them are approximately equilateral. Equilateral triangles are preferable because more accurate results can be obtained in the 2-D interpolation.

To generate 2-D depth profiles, all rectangular grid points are located and interpolation is performed at all grid points. Fig. 4.7(a) shows a 3-D surface plot representing the sea-bed topography of a surveyed area and Fig. 4.7(b) shows the corresponding contour plot. The depth in this area ranges from 25 m to 34 m and we can see that the resulting surface appears smooth and natural.

When the depth of the ocean is more or less constant over a large area, reasonable results can still be maintained after interpolation. Fig. 4.8(a) shows the surface plot resulting from data collected in the area where the depth ranges from 7.2 m to 8.6 m. As can be seen, the oscillatory behavior of the approximation is minimized. Fig. 4.8(b) depicts the contour plot of the resulting surface.

Fig. 4.9(a) shows the results of a surveyed area where the depth ranges from 2 m to 12 m. The resulting surface is continuous and smooth as can be seen in the corresponding contour plot in Fig. 4.9(b).

4.4 2-D FILTERING OF IMPULSIVE NOISE

A sea-depth estimate can be regarded as an unreliable or a rogue measurement if its value is not supported by its neighboring points, i.e., if it is significantly different from those in its neighborhood in a local region of a 2-D sea-depth profile. Rogue measurements appear as sharp spikes in the profile,

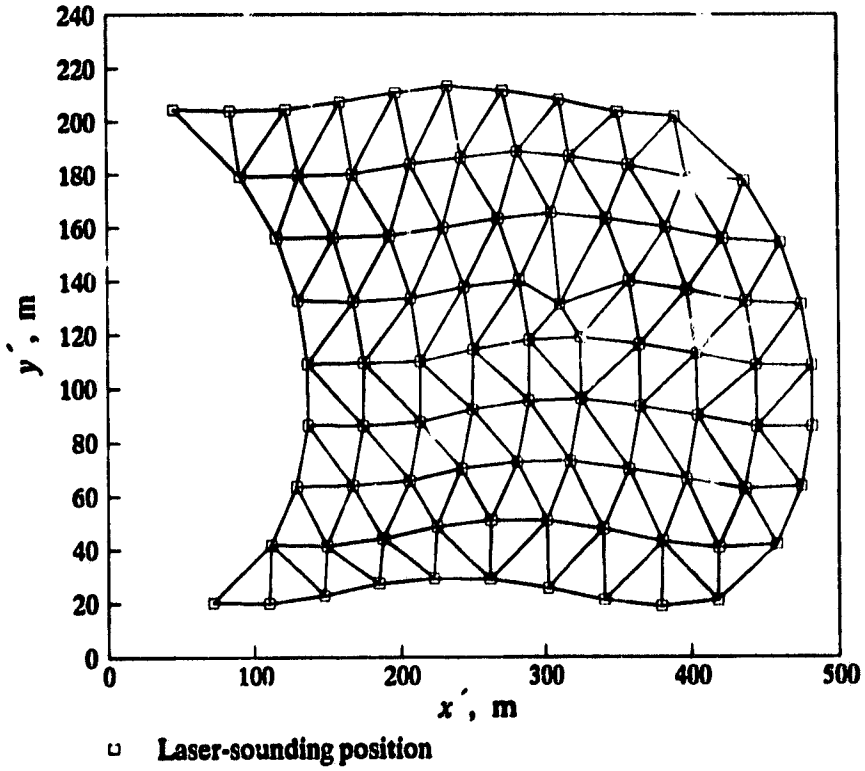

Fig. 4.6 Construction of a triangular grid from irregularly spaced data.

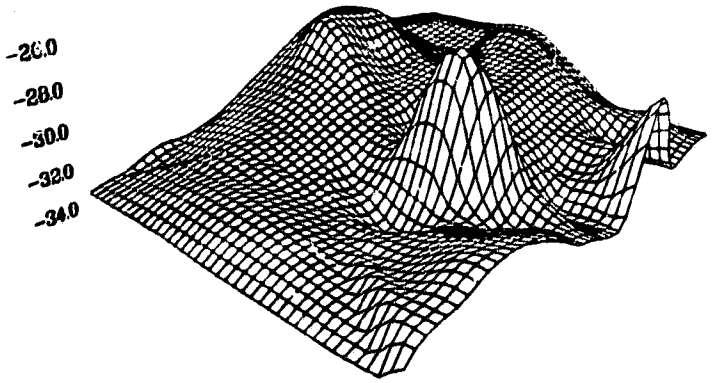

(a)

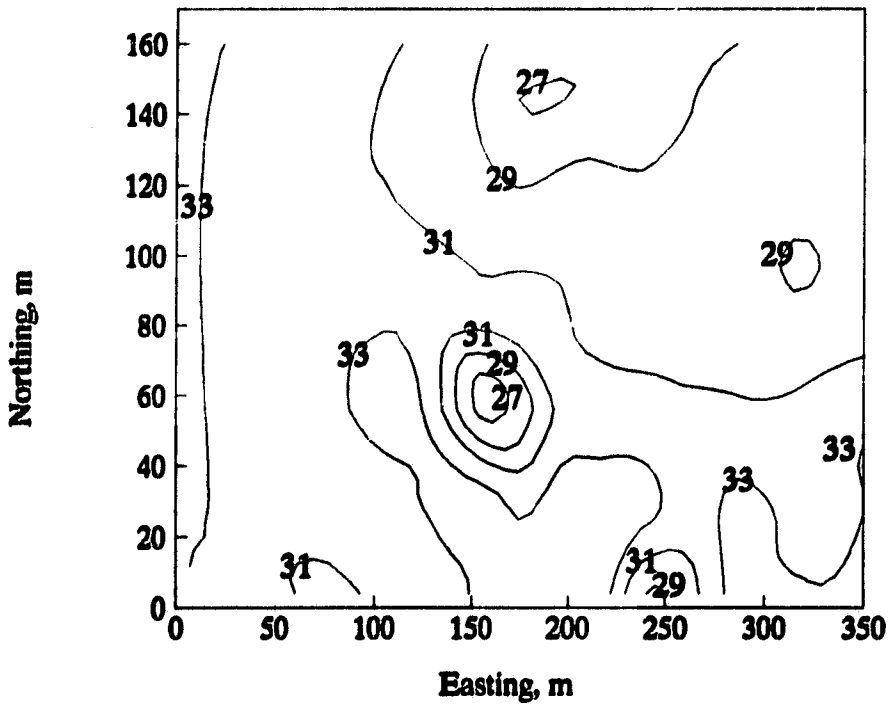

(b)

Fig. 4.7 Sea-bed topography (depth range: 26 m to 34 m): (a) 3-D surface plot; (b) contour plot.

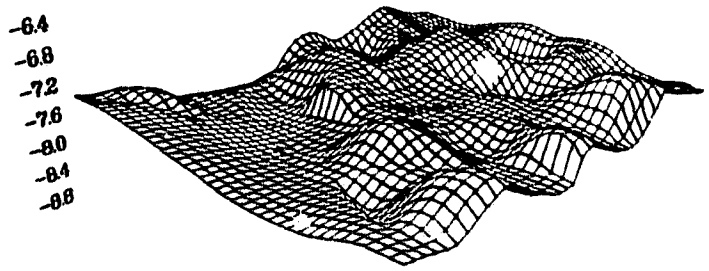

(a)

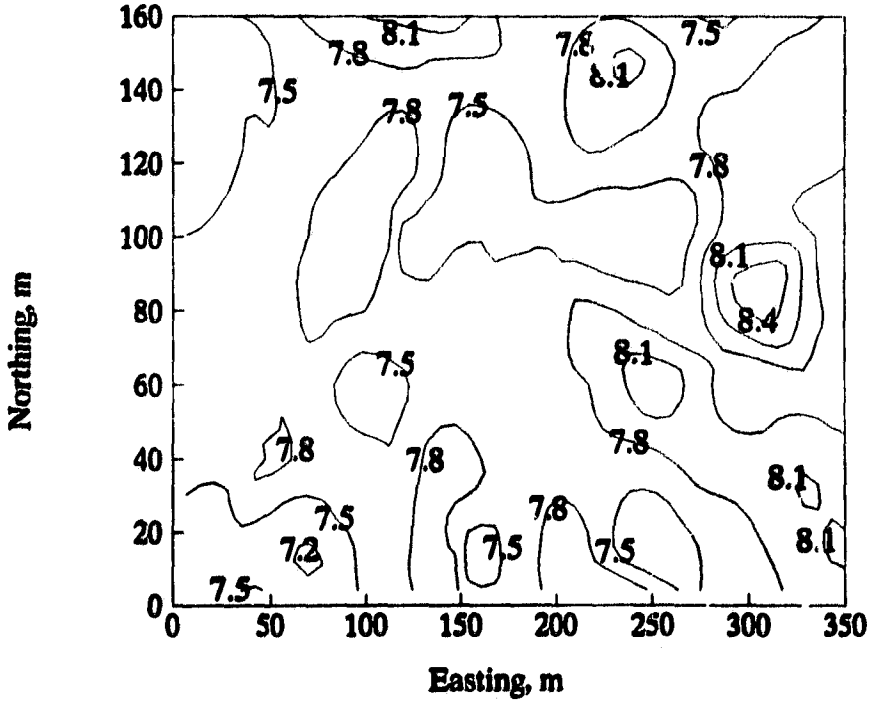

(b)

Fig. 4.8 Sea-bed topography (depth range: 7.2 m to 8.6 m): (a) 3-D surface plot; (b) contour plot.

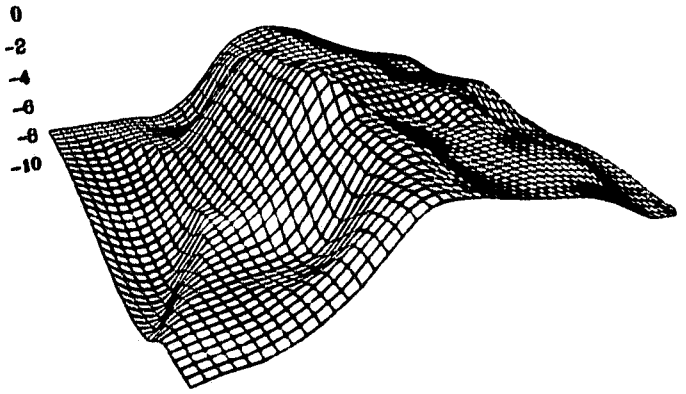

(a)

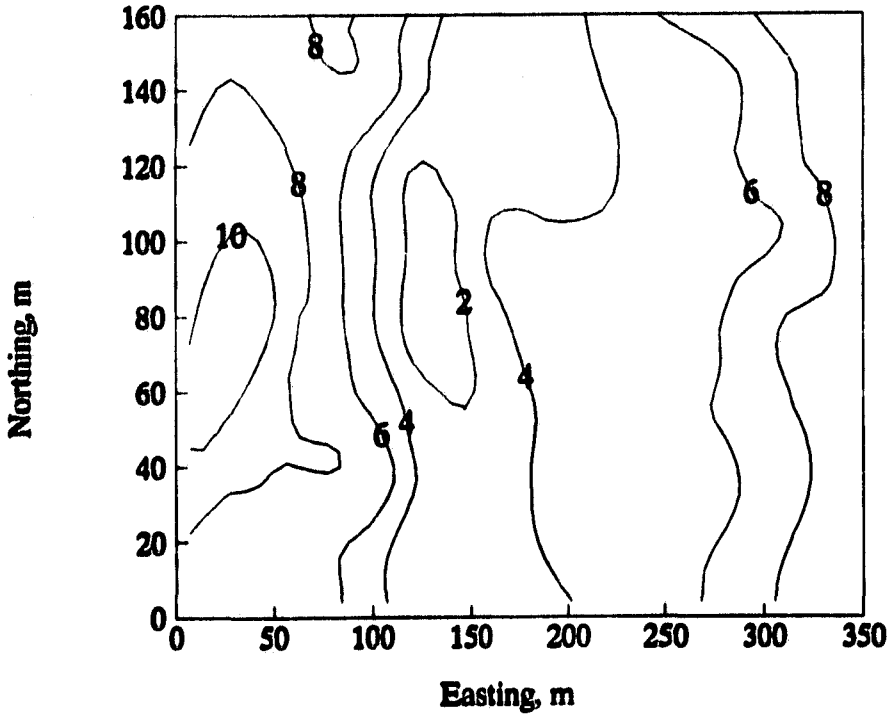

(b)

Fig. 4.9 Sea-bed topography (depth range: 2 m to 12 m): (a) 3-D surface plot; (b) contour plot.

which do not represent geological features of the ocean floor and their occurrence is often due to errors in measurement as indicated in Section 4.1. Since spikes appear as impulses in a profile, they are referred to as impulsive noise.

In this section, we introduce one type of 2-D interpolating filters for removing impulsive noise from the scattered sea-depth estimates. In filtering impulsive noise, we have two objectives in mind. The first objective is to identify the rogue sea-depth estimates present in a profile so that further action can be undertaken. The second objective is to apply correction to these spikes or rogue estimates by assuming that spikes generally do not represent geological features. Obviously, the first objective is independent of the second one and, as a result, one may need not to attain both simultaneously. We assume that spikes are due to noise present in a profile and, therefore, appropriate correction will be applied to these estimates after they have been detected.

In order to suppress impulsive noise and eliminate its effects on surrounding depth estimates, it is desirable to have some mechanism to operate only on the impulsive noise components and leave the rest of the signal intact. And, to be applicable to laser bathymetry, the technique developed should handle data points that do not fall on a regular grid and, further, the correction applied to the impulsive value must be reasonable so that the corrected value will conform to the trend and slope in the local region and relate naturally to its neighbors. To achieve this, a nonlinear scheme which involves two stages, has been developed. The first stage is concerned with the search for samples with impulsive values while the second stage deals with the correction of these values.

4.4.1 Identification of impulsive values based on order-statistics filters

In order to identify impulsive values, a method based on the principle of a type of nonlinear filtering known as order-statistics filtering [68] is developed. In a one-dimensional order-statistics filter (OSF),

the output at a point is given by a linear combination of the order statistics of a set of data located on the left and right of that point. Specifically, if y_k is the kth output sample of an OSF with window size $2N + 1$, then for an input sequence $\{x\}$, y_k is given by

$$y_k = \sum_{j=1}^{2N+1} w_j x_{(j)} \tag{4.20}$$

where $x_{(j)}$ is the jth smallest sample among the $2N + 1$ samples inside the window centred at k and w_j is a constant weight applied to $x_{(j)}$. Note that when $w_{N+1} = 1$ and the rest of the weights are set to zero, the OSF becomes a median filter; when $w_{q+1} = w_{q+2} = \cdots = w_{2N+1-q} = 1/[2(N-q)+1]$ where $0 \le q \le N$ and the rest of the weights are set to zero, the OSF becomes an alpha-trimmed mean filter [69]. The median filter has been shown to be effective in suppressing impulsive noise [70]-[71] while the alpha-trimmed mean filter allows compromise between noise averaging and impulsive noise suppression [69], [72]. Thus by setting the weights in Eq. (4.20) appropriately, we can design filters for specific needs. Our objective is to extend the basic underlying principle in the OSF, namely, the ordering and weighting of input sequence, to the two-dimensional domain with scattered data points for effective detection of impulsive values.

Suppose that we have a set of depth estimates $D = \{d_i, i = 1, 2, ..., N\}$ scattered in a 2-D profile. In order to determine if d_i is an impulsive value, we can proceed as follows. First, we define a neighborhood of d_i and then utilize the spatial relationship among the data points within the neighborhood to predict the value of d_i. If d_i is different from the prediction by a significant amount, then this indicates that d_i is an isolated value which does not conform to its neighbors in a local region. Hence, d_i should be considered as an impulsive value. Note that this scheme works well if the neighbors of d_i do not contain impulsive noise components; otherwise, serious prediction error may result causing

d_i to be considered as an impulsive value when it is not, or vice versa. One alternative to alleviate this problem is to first rank all the data points in the neighborhood of d_i according to their values. Then, limit the influence of the data points which deviate substantially from the median of the ranked list on the prediction. By doing so, extreme values, both low and high, can no longer distort the prediction and, as a result, the prediction becomes more reliable. Hence, the accuracy in detecting impulsive values in a profile can be improved quite significantly.

Suppose that a depth estimate d_i is located at the sounding location $\mathbf{c}_i$ defined on an x-y Cartesian-coordinate system. To define a neighborhood of d_i, we search for its closest depth estimates $Z = \{z_j, j = 1, 2, ..., M\}$ at the corresponding sounding location $S = \{\mathbf{s}_j, j = 1, 2, ..., M\}$ within a predefined search range R. When Z is defined, we then sort the elements in Z into ascending order such that $z_{(1)} \leq z_{(2)} \leq \cdots \leq z_{(M)}$ where $z_{(j)}$ represents the jth item in the ordered array. To limit the influence of possible extreme values, we discard q_1 and q_2 samples from the low and high ends of the ordered array, respectively, to form

$$X = \{z_{(q_1+1)}, z_{(q_1+2)}, \cdots, z_{(M-q_2)}\}$$

In order to utilize the data points in X to predict the value at $\mathbf{c}_i$, we apply proportional weights to each $z_{(j)}$ in X to express the relative influence of each point on the prediction. Since, in general, the spatial correlation of a typical bathymetric surface decreases with increasing distance in a local region, the weights applied to the more distant points should be less than those applied to the nearby points. One suitable weighting function is the inverse distance-powered function given by

$$w_j = \frac{A}{l_j^b}$$

where l_j represents the Euclidean distance between $\bar{\mathbf{s}}_j$ and $\mathbf{c}_i$, $\bar{\mathbf{s}}_j$ denotes the sounding location of $z_{(j)}$, b controls the degree of influence of distance on the prediction, and A is a normalizing constant defined as

$$A = \frac{1}{\sum_{j=q_1+1}^{M-q_2} \frac{1}{l_j^b}}$$

such that

$$\sum_{j=q_1+1}^{M-q_2} w_j = 1$$

By applying w_j to $z_{(j)}$ in X for each j, the prediction at $\mathbf{c}_i$ can be obtained as

$$p = \sum_{j=q_1+1}^{M-q_2} w_j z_{(j)} \tag{4.21}$$

To determine whether d_i is an impulsive value, we compare d_i with p and if their absolute difference $|p - d_i|$ is greater than a threshold value, say T, then d_i is considered as an impulsive value. Fig. 4.10 depicts the block diagram illustrating the overall detection process. The process is represented as a cascade of a nonlinear operation, i.e., ranking, with a linear operation, i.e., weighted averaging, followed by a decision process.

4.4.2. Replacement of impulsive values by using 2-D interpolation

Suppose that the depth estimate d_i located at $\mathbf{c}_i$ has been identified as an impulsive value, in order to obtain a reasonable estimate $\hat{d}_i$ to replace d_i, we apply the 2-D interpolation method as discussed in Section 4.3 at $\mathbf{c}_i$. Specifically, we start by searching for a set of depth estimates $U = \{z_j, j = 1, 2, ..., L\}$ at the corresponding location $V = \{\mathbf{s}_j, j = 1, 2, ..., L\}$ in a neighborhood of d_i. By using V, a triangular grid is constructed according to the scheme as described in Section 4.3 such that the

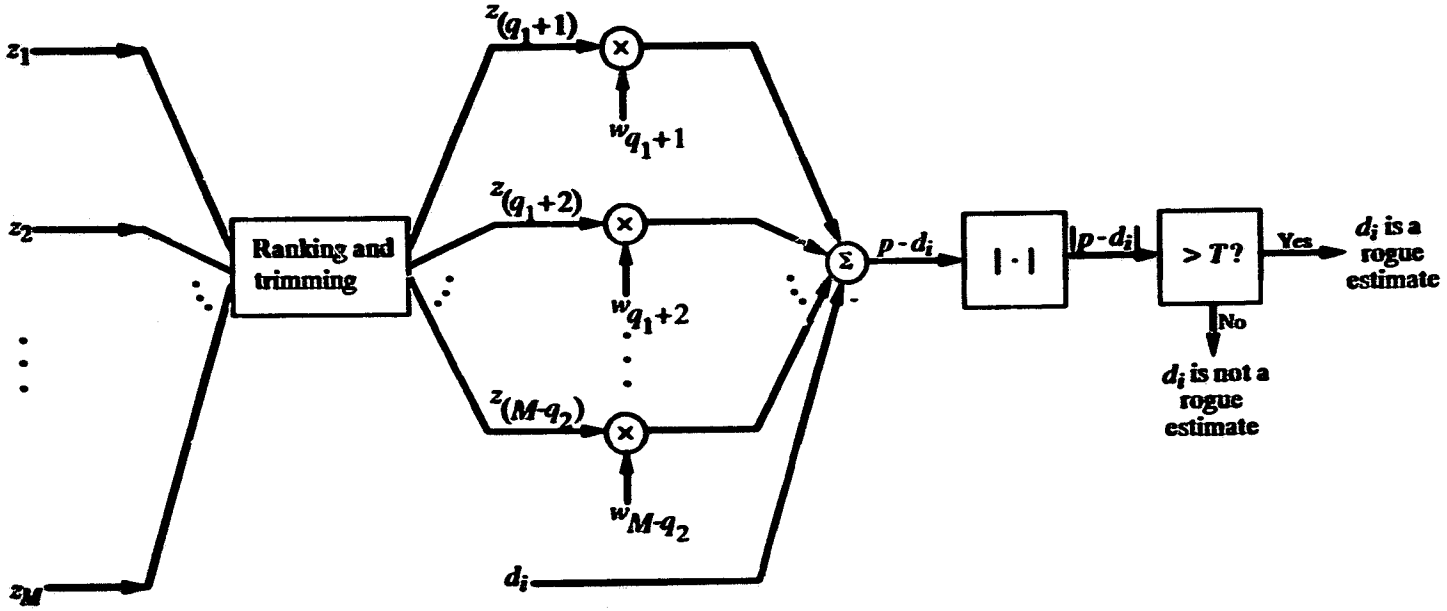

Fig. 4.10 Block diagram for the detecton of rogue sea-depth estimates.

vertex of each triangle represents the projection of each data point in U on the x-y plane. From the triangular grid, we then determine the particular triangular cell C within which d_i is located. Once C is determined, our next step is to estimate the first- and second-order partial derivatives with respect to x and y, respectively, using the procedure outlined in Section 4.3.2 at each vertex of C in order to obtain the gradient and curvature information at these three data points. Using this knowledge together with the depth information at the vertices of C, a representative surface, which is in the form of a bivariate 5th-degree interpolating polynomial as expressed in Eq. (4.7), is then constructed to describe the behavior of the topography over C. By evaluating the interpolating function explicitly at e_i, $\hat{d}_i$ is then obtained.

4.4.3. Filtering algorithm and results

The procedure developed in Sections 4.4.1 and 4.4.2 can be set up as an algorithm, Algorithm 4.1, as follows. The process for detecting rogue measurements in a profile is carried out in the first part of the algorithm while the second part deals with the correction procedure by using 2-D interpolation. The algorithm contains several important parameters and the following provides a guideline for choosing the values of these parameters.

In Step A1, the algorithm uses a predetermined search radius r to limit the search range. In order to automate the computation of r for a given M, the following procedure can be used.

1. Select an arbitrary data point from the profile and search for its M closest neighbors to form a set of $M + 1$ data points.
2. Compute the mean centre [73] $m_c = (x_c, y_c)$ from these $M + 1$ data by

$$x_c = \frac{1}{M+1}\sum_{i=1}^{M+1} x_i \quad \text{and} \quad y_c = \frac{1}{M+1}\sum_{i=1}^{M+1} y_i$$

where (x_i, y_i) represents the sounding location of the ith data.

Algorithm 4.1: 2-D filtering of impulsive noise

For each data point d_i, $i = 1, 2, ..., N$ in a profile do:

A1. Search for the laser sounding location s_j, $j = 1, 2, ..., M$ closest to c_i within a search radius r where c_i is the sounding location of d_i.

A2. Sort $Z = \{z_j, j = 1, 2, ..., M\}$ where z_j is the depth estimate at s_j into ascending order to form an ordered array Y.

A3. Remove q_1 and q_2 data samples from the low and high ends of Y, respectively, i.e., form $X = \{z(q_1 + 1), z(q_1 + 2), ..., z(M - q_2)\}$.

A4. Compute a weighted sum p from X by using Eq. (4.21).

A5. If $|p - d_i| > T$ then:

i. Report d_i is a rogue measurement.

ii. Record the location c_i.

iii. Increment the counter K where $K = 0$ initially.

For each rogue measurement d_i, $i = 1, 2, ..., K$ do:

B1. Search for the depth estimates $U = \{z_j, j = 1, 2, ..., L\}$ at the corresponding sounding location $V = \{s_j, j = 1, 2, ..., L\}$ which are closest to c_i where c_i is the location of the rogue measurement d_i, $s_j \neq c_i$, $i = 1, 2, ..., K$ for all j, and $L > M$.

B2. Construct a triangular grid by using V and identify the triangular cell C within which d_i is located.

B3. Estimate the first- and second-order partial derivatives at the three vertices of C by using the data points in U.

B4. Construct a 2-D interpolating function $z(x, y)$ over C by using Eq. (4.7). Evaluate the function at c_i to obtain $\hat{d}_i$.

3. Compute the standard distance [73] l_o by

$$l_o = \sqrt{\frac{1}{M+1}\sum_{i=1}^{M+1} l_i^2}$$

where l_i is the Euclidean distance between the ith data and m_c.

4. Repeat Steps 1 to 3 in different areas of the profile in order to compute an average of the standard distance $\bar{l}_o$.

5. Compute $r = \lambda \bar{l}_o$ where λ is a scaling constant typically in the range $1 < \lambda < 2$.

Since standard distance is a concise statistical measure of the spatial dispersion of data points, the use of this measure for the computation of r provides a convenient and reliable way to define r.

From Steps A1 to A4 of the algorithm, we assume that a total of M neighbors can be found within r for each d_i. When the actual number of neighbors found is less than M in particular areas, the ordering and computation involved in these steps should be modified accordingly.

The choice of M in Step A1 and the choice of q_1 and q_2 in Step A3 depend on the sounding density of the laser system, the computational time allowed, as well as the reliability of the depth estimates in the profile. Typically, $M \leq 8$ and $q_1, q_2 \leq 2$ can be used. Since rogue measurements are identified in Step A5 by means of thresholding, proper choice of T is essential. In shallow-water bathymetry using airborne laser system, sea depth that can be estimated typically ranges from 1.5 to 40 m. Therefore, the use of a large value of T, say 10 m, is effective in identifying appropriate rogue measurements.

In the second part of the algorithm, we use L neighbors of the rogue measurement to perform 2-D interpolation. To improve interpolation, depth estimates which have been identified as rogue measurements are not considered as neighbors, as indicated in Step B1. To simplify the implementation,

we perform the triangulation in Step B2 and estimate the partial derivatives in Step B3 by using the same L neighbors of d_i. In Step B2, the objective to perform triangulation is to obtain C which should be approximately equilateral to improve the interpolation result. To achieve this, besides using the immediate neighbors of d_i, a few more data points close to c_i are needed to improve the triangulation. As a result, L should not be small. In Step B3, we estimate the partial derivatives at each vertex of C locally. To achieve this, the number of closest neighbors chosen for each vertex is four. Therefore, in order to improve the estimation of $\hat{d}_i$, the L neighbors chosen should include the neighbors of each vertex. In order to satisfy the requirements in both Steps B2 and B3, $L = 16$ is chosen in our implementation.

Algorithm 4.1 has been applied to the depth profiles obtained in Lake Huron, Ontario, Canada during a survey in 1992 by using the LARSEN 500 airborne system. In the application, $M = 7$ and $q_1 = q_2 = 1$ were used to predict p. In addition, $b = 2$ was used in order to achieve inverse distance-squared weighting, i.e., the influence of a depth estimate at d_i is inversely proportional to its squared distance from d_i. The value $\overline{l}_o = 45.5$ m has been determined from the profiles according to the scheme presented in this section and with $\lambda = 1.5$, we obtained $r = 68.3$ m as the search radius. In order to reject only relatively large spikes while tolerate local fluctuations, $T = 10$ m was used. Fig. 4.11 illustrates an example of the application of Algorithm 4.1. In Fig. 4.11(a), the data point of interest d_i has a value of 17.58 m. In order to determine if it is an impulsive value, its seven closest neighbors, which are shown in Fig. 4.11(a), are first selected and then ranked to form an ordered array. After removing the first and last samples, namely, 4.61 m and 6.72 m, respectively, from the array, the remaining samples are weighted by using Eq. (4.21) to obtain $p = 5.81$ m. Since the absolute difference between d_i and p is greater than 10 m, d_i is detected as an impulsive value. To replace this value

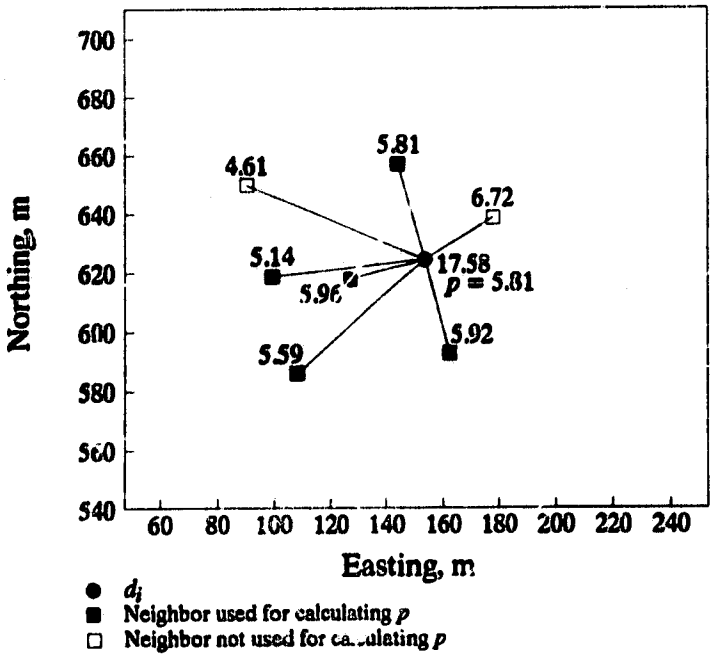

Fig. 4.11(a) Detection of an impulsive value (numbers shown are in meters).

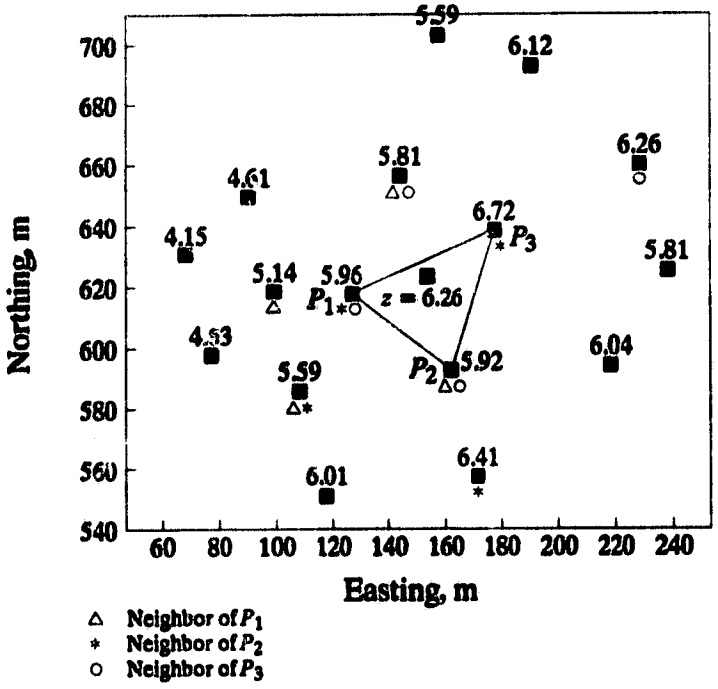

Fig. 4.11(b) Replacement of the impulsive value detected in Fig. 4.11(a) (numbers shown are in meters).

through the use of 2-D interpolation, we select its 16 closest neighbors from the profile as shown in Fig. 4.11(b). Based on the location of these data, we find that d_i is located within the triangle with vertices P_1, P_2, and P_3 as shown in the figure. In order to estimate the partial derivatives at each vertex, the four closest neighbors of each vertex are selected as indicated in Fig. 4.11(b). By using the values of the estimated partial derivatives together with the depth estimates at each vertex, the interpolating function in Eq. (4.7) is constructed and the interpolation value is found to be 6.26 m, which is more consistent with the surrounding samples as expected. Fig. 4.12 illustrates another example of the application of the algorithm. Fig. 4.12(a) shows that the depth estimate d_i = 25.12 m is different from p = 7.34 m by more than 10 m; as a result, d_i is considered as a rogue measurement. Fig. 4.12(b) illustrates that this measurement is replaced by a value of 7.04 m after 2-D interpolation. Since the depth in the area surrounding the impulsive value ranges from 6 to 8.5 m, the replacement provides a far better representation of the sea depth.

4.5 PERFORMANCE OF 1-D SIGNAL PROCESSING UNDER THE VERY-LOW RESOLUTION CONDITIONS

In Chapter 3, we have performed a detailed comparative study of the sea-depth estimates obtained from the 1-D processing algorithms with the results obtained by the surveying company. In this section, we complete the comparative study by considering the situation where the resolution between the laser reflections is very low, which may represent cases when the surface and bottom reflections strongly overlap or when the bottom reflection is embedded in the backscattered envelope. Under these circumstances, sea-depth estimates are not available from the surveying company. As a result, we assess the quality of the 1-D results by comparing them with some predictions. To make the comparison meaningful, the prediction made at a sounding location should in some way accurately express the

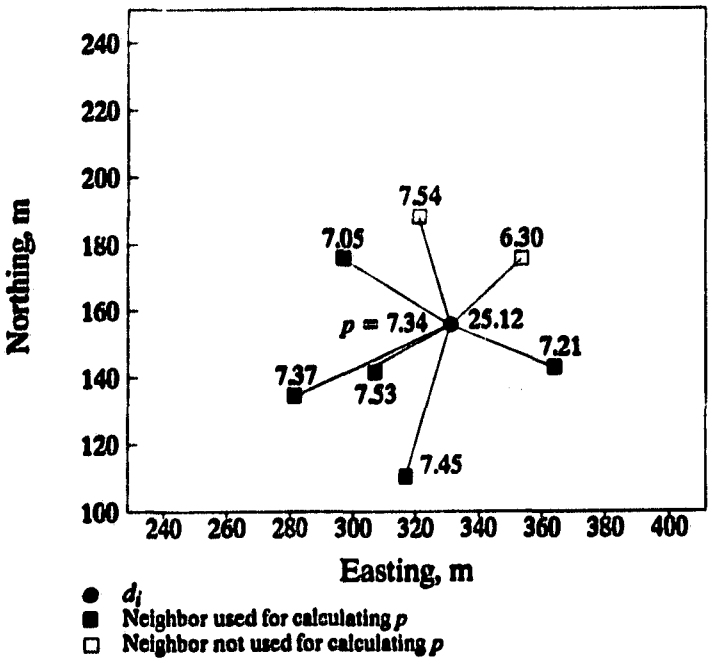

Fig. 4.12(a) Detection of an impulsive value (numbers shown are in meters).

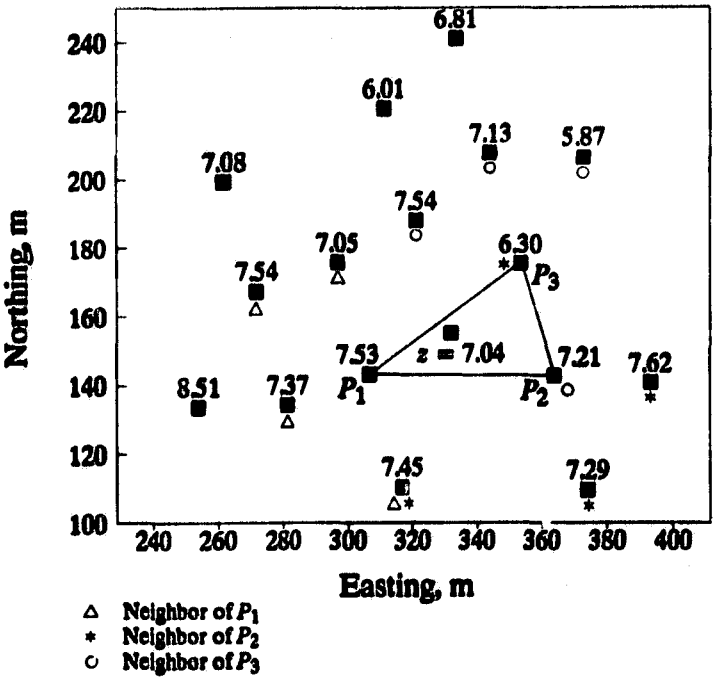

Fig. 4.12(b) Replacement of the impulsive value detected in Fig. 4.12(a) (numbers shown are in meters).

combined influences of the surrounding data. One approach to achieve this is to use the 2-D interpolation method described in Section 4.3. Suppose that we wish to obtain a predicted value $\tilde{d}_i$ at a sounding location $\mathbf{c}_i$, we can employ the interpolation procedure described in Section 4.4.2. Specifically, we first identify the sounding locations at which the depth estimate are not available from the company due to the fact that the resolution between the laser reflections is very low. If $\mathbf{c}_i$ is the identified sounding location, a set of 1-D results U can be searched in a neighborhood of $\mathbf{c}_i$. A triangular grid is then constructed from U and the particular triangular cell within which $\mathbf{c}_i$ is located can be identified. Subsequently, 2-D interpolation is performed at $\mathbf{c}_i$ to obtain $\tilde{d}_i$. The predicted value $\tilde{d}_i$ is then compared with the waveform-decomposition result obtained at $\mathbf{c}_i$. Fig. 4.13 provides an example of the comparison. The predicted value obtained from interpolation is based on the 16 neighbors of $\mathbf{c}_i$, which are also shown in Fig. 4.13. In the example, we observe that there is a 0.05-m difference between the interpolation and decomposition results. If the interpolated value is treated as a reasonable prediction, which is valid particularly when the sea bottom is not rough, then the 1-D result estimated from the waveform can be considered as a satisfactory result. The overall comparison is illustrated in Fig. 4.14.

The scattered plot depicted in Fig. 4.14(a) shows the comparison of the two results at the sounding locations where depth estimates are unavailable from the surveying company. These locations are chosen at random from different areas in Lake Huron, Ont. and the sample collected contains about 130 laser soundings. From Fig. 4.14(a), it is interesting to see that although the two results are obtained from different means, they are quite consistent with each other. Some outliers can also be found from the figure indicating that the discrepancy between the two results can be large at some sounding locations, although the number of outliers is relatively small.

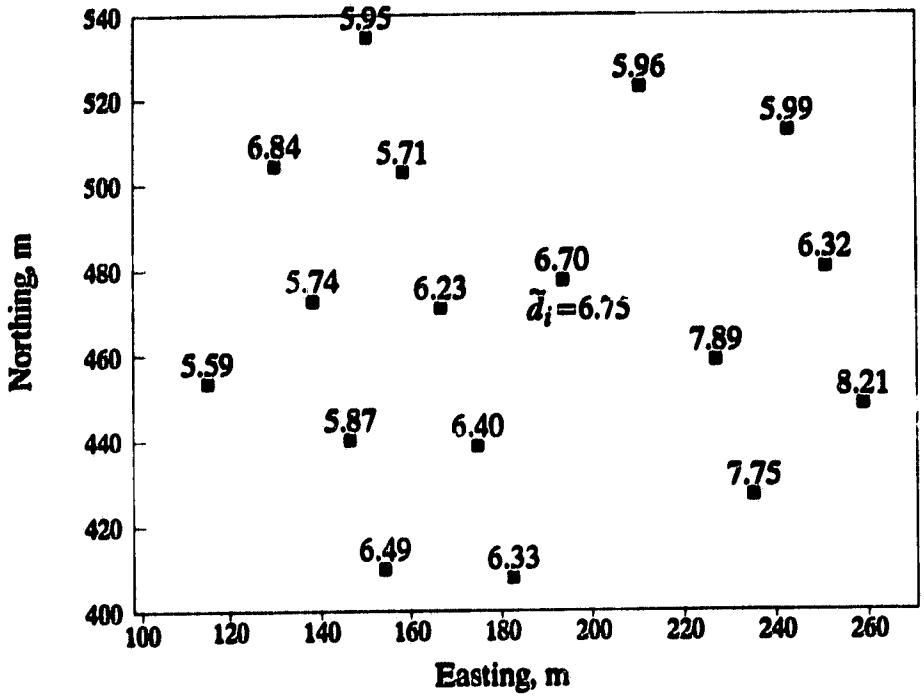

Fig. 4.13 Comparison of the 1-D result with a predicted value based on interpolation.

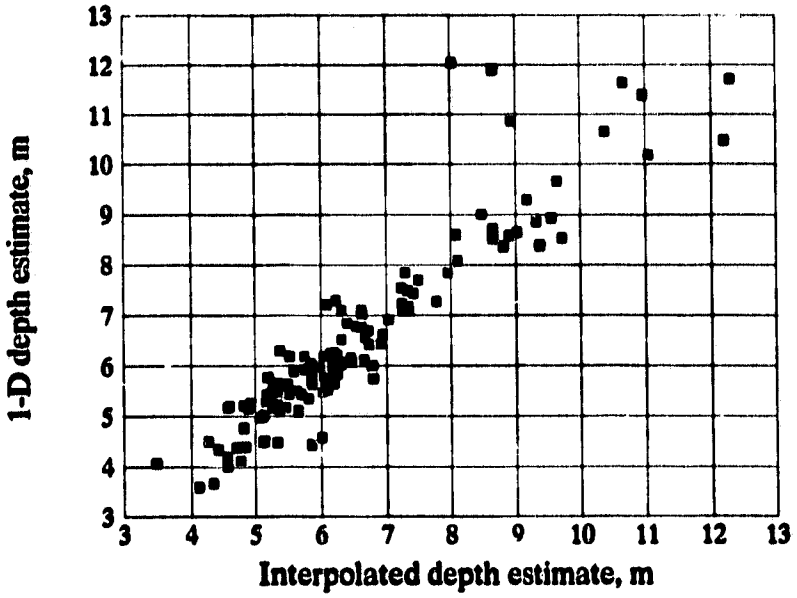

(a)

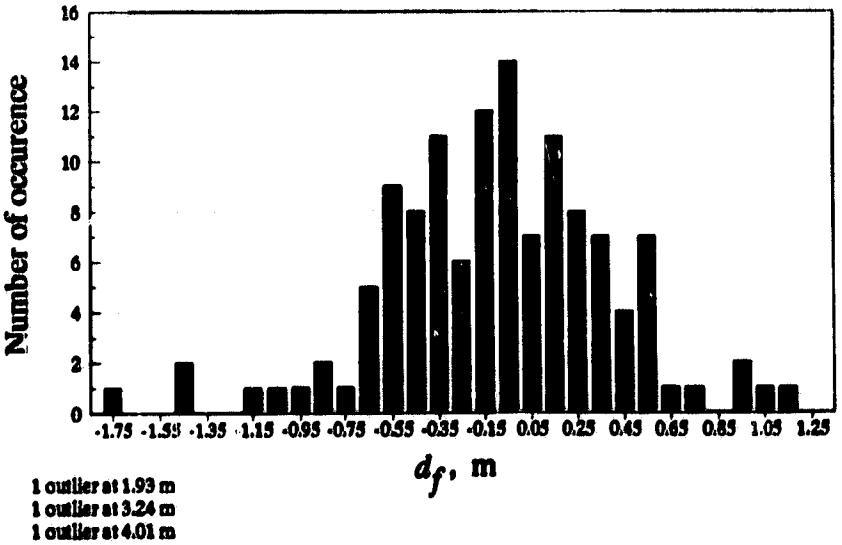

(b)

Fig. 4.14 Comparison of 1-D results with interpolation results: (a) scatter plot; (b) histogram of differences of the two results.

Fig. 4.14(b) shows a histogram of the differences d_f between the two results where $d_f = d_{WD} - \hat{d}_i$ for all i which are plotted in Fig. 4.14(a). Three of the outliers found in Fig. 4.14(a) are not shown in the histogram but their values are displayed below the plot. By examining the histogram, we find that approximately 80 % of d_f are within ± 0.5 m and 92 % of d_f are within ± 1 m. These results show that a large proportion of the waveform-decomposition results are fairly close to the predictions based on 2-D interpolation. This suggests that the application of decomposition can offer significant potential in recovering "lost" sea depths due to the lost of resolution between the laser reflections which occurs frequently in areas with turbid waters.

4.6 CONCLUSIONS

A sophisticated 2-D interpolation technique has been described for the reconstruction of 3-D sea-bed topography from the scattered sea-depth estimates. The technique has been applied to typical laser bathymetric data and, as expected, the interpolated depth profiles obtained are free of oscillations and appear natural.

A type of 2-D interpolating filter has been introduced for the filtering of impulsive noise. Based on the concept of order-statistics filtering, the interpolating filter has been found to be effective in identifying rogue measurements from the 2-D irregularly spaced sea-depth estimates. When the rogue measurements are unwanted signal, the interpolating filter can be applied to provide reasonable approximation to sea depths so that the approximations can conform to the slope and trend of the local topography.

The quality of 1-D results obtained under the very-low resolution conditions has been assessed through a comparison with the predictions obtained from 2-D interpolation. Comparison results

indicated that "lost" sea depths due to a loss of resolution can be restored from the received waveforms through the use of waveform decomposition.

CHAPTER FIVE
TWO-DIMENSIONAL SIGNAL PROCESSING OF INTERPOLATED SEA-DEPTH ESTIMATES

5.1 INTRODUCTION

In Chapter 4, we have discussed a type of 2-D interpolating filter that can be used to filter impulsive noise present in the scattered bathymetric data. After the impulsive noise is removed by using this type of filter, 2-D interpolation can be applied to the scattered data to form a rectangular grid of data points. In this chapter, we focus our attention on the removal of wideband noise present in the 2-D interpolated profiles.

As detailed in Section 4.1, a number of sources may give rise to random errors in the scattered depth estimates which constitute wideband noise in a 2-D profile. To eliminate wideband noise, we suggest two adaptive 2-D filtering procedures. The first procedure involves 2-D power spectral analysis of sea-bed topography on a block-by-block basis. By examining the estimated power spectrum in each block, we can determine the appropriate type of 2-D digital filter to be designed and the values of the corresponding filter parameters. The second procedure involves the estimation of the bathymetric data from the interpolated data based on a 2-D space-variant filter. In this procedure, we perform filtering on a point-by-point basis so that noise smoothing can be adapted to each data point in a profile.

5.2 2-D FILTERING BASED ON POWER SPECTRAL ANALYSIS

Bathymetric profiles can be analyzed in the frequency domain for a number of purposes. For example, one can utilize the frequency-domain representation to provide an objective quantitative characterization of the ocean floor. Different characteristics of the ocean floor give rise to distinguished patterns in the spatial-frequency domain and when these patterns are carefully analyzed in relation to the morphology

of the sea floor, elaborate geophysical studies with regard to the relief-forming geological processes can be carried out.

Another purpose in processing bathymetric profiles in the frequency domain is for noise reduction. Here, we examine the frequency contents of both the signal and the noise. With the knowledge of the corresponding frequency contents, we can then design appropriate 2-D digital filters that can remove noise from the measured profile. After filtering, the data obtained are an improved and more reliable representation of the sea-bed topography.

In this section, we explore the use of 2-D digital filtering in bathymetric profiles. In order to preserve the integrity of the signal in the filtering, we will formulate an adaptive approach.

Let R be the region of interest, which may represent the surveyed area. To process the profile in R, we first divide R into a number of blocks. At the kth block, we let $f_k(n_1, n_2)$ be the true bathymetric data. If the block size chosen is large enough, say, 500 m × 500 m, then $f_k(n_1, n_2)$ can be decomposed into two components as

$$f_k(n_1, n_2) = t_k(n_1, n_2) + l_k(n_1, n_2) \tag{5.1}$$

where $t_k(n_1, n_2)$ denotes the trend of the data at the kth block and $l_k(n_1, n_2)$ denotes the local variations about this trend. Further, we let $v_k(n_1, n_2)$ be the wideband noise present in this block of data. Under these circumstances, the measured depth can be represented as

$$\begin{aligned} g_k(n_1, n_2) &= f_k(n_1, n_2) + v_k(n_1, n_2) \\ &= t_k(n_1, n_2) + l_k(n_1, n_2) + v_k(n_1, n_2) \end{aligned} \tag{5.2}$$

by using Eq. (5.1). In our problem, $g_k(n_1, n_2)$ is the profile obtained after 2-D interpolation.

Suppose that $t_k(n_1, n_2)$ can be identified, we can obtain a detrended profile as

$$x_k(n_1, n_2) = g_k(n_1, n_2) - t_k(n_1, n_2) \tag{5.3}$$

and by using Eq. (5.2)

$$x_k(n_1, n_2) = l_k(n_1, n_2) + v_k(n_1, n_2) \tag{5.4}$$

As a result, $x_k(n_1, n_2)$ represents the local variations which are corrupted by noise. Our objective is to smooth $x_k(n_1, n_2)$ in Eq. (5.4) such that $v_k(n_1, n_2)$ can be reduced while preserving $l_k(n_1, n_2)$. To achieve this we need to examine the power spectrum of $x_k(n_1, n_2)$.

The advantage of separating the trend component from the profile before performing spectral analysis is that the frequency components associated with the trend are mainly concentrated in the region close to the zero frequency. This component will dominate the power-spectrum estimate, obscuring other low-frequency components which have smaller amplitude. Subtracting the trend from the profile often leads to better estimate of the spectrum in the low-frequency region. As a result, we can then focus our attention on the frequency components of $l_k(n_1, n_2)$ in the spectrum. By doing so, the wideband noise can be eliminated more effectively.

5.2.1 Estimation of 2-D power spectrum

There are various methods to estimate the power spectrum of a 2-D depth profile. One approach is known as the periodogram method [74], which is based on the direct Fourier transformation of finite-length segments of the signal. Another approach is known as the correlation-windowing method [74], which is also referred to as the smoothed-periodogram method [75]. In this method, we first estimate the 2-D autocorrelation function from the data sequence. Then a suitable 2-D window is applied to the autocorrelation estimate. The resulting sequence is subsequently transformed to obtain an estimate of the power spectrum.

Both the periodogram and correlation-windowing methods are based on the use of the discrete Fourier transform (DFT); therefore, the estimate of the power spectrum can be computed by exploiting the computational efficiency of fast Fourier transform (FFT) algorithms. In the periodogram method,

the variance of the spectrum estimate can be quite large. However, by choosing an appropriate 2-D window in the correlation-windowing method, we can include only those autocorrelation estimates for which the variance is low. As a result, the variance of the estimated power spectrum can be reduced.

To simplify the notation, we use $x(n_1, n_2)$ to denote $x_k(n_1, n_2)$ since the following description is applicable to any block of data. Let $x(n_1, n_2)$ be a 2-D stationary random process and $x(n_1, n_2)$ be a sample of $x(n_1, n_2)$. Our spectral-estimation problem is to estimate the 2-D power spectrum of $x(n_1, n_2)$, which is defined as

$$P_x(\omega_1, \omega_2) = \sum_{m_1=-\infty}^{\infty} \sum_{m_2=-\infty}^{\infty} R_x(m_1, m_2)\, e^{-j\omega_1 m_1} e^{-j\omega_2 m_2} \tag{5.5}$$

where $R_x(m_1, m_2)$ denotes the 2-D autocorrelation function of $x(n_1, n_2)$. Assuming that $x(n_1, n_2)$ is ergodic, $R_x(m_1, m_2)$ can be estimated from $x(n_1, n_2)$ as

$$\hat{R}_x(m_1, m_2) = \frac{1}{N_1 N_2} \sum_{n_1=0}^{N_1-|m_1|-1} \sum_{n_2=0}^{N_2-|m_2|-1} x(n_1, n_2)x(n_1+m_1, n_2+m_2) \tag{5.6}$$

where $|m_1| \le N_1 - 1$, $|m_2| \le N_2 - 1$, $\hat{R}_x(m_1, m_2) = \hat{R}_x(-m_1, -m_2)$, and $N_1 \times N_2$ is the size of $x(n_1, n_2)$. Eq. (5.6) can be implemented by using the DFT method in order to take advantage of its associated fast FFT algorithms. Specifically, $\hat{R}_x(m_1, m_2)$ can be computed as

$$\hat{R}_x(m_1, m_2) = \frac{1}{N_1 N_2} \text{IDFT}\left[\,|X(k_1, k_2)|^2\right] \tag{5.7}$$

where $X(k_1, k_2) = \text{DFT}[x(n_1, n_2)]$, and DFT $[\cdot]$ and IDFT $[\cdot]$ represent the DFT and inverse DFT of $[\cdot]$, respectively.

In Eq. (5.6), we see that when $|m_1|$ is close to $N_1 - 1$ and/or $|m_2|$ is close to $N_2 - 1$, fewer samples of $x(n_1, n_2)$ are used in the computation of $\hat{R}_x(m_1, m_2)$ and, therefore, the variance of $\hat{R}_x(m_1, m_2)$ is expected to increase with increasing $|m_1|$ and/or $|m_2|$. In order to reduce the

variance of $\hat{R}_x(m_1, m_2)$, we can apply an appropriate 2-D window to $\hat{R}_x(m_1, m_2)$ to reduce the contribution of the correlation estimates when $|m_1|$ and $|m_2|$ are large. By doing so, we can improve the estimate of the power spectrum.

To obtain an estimate of the power spectrum by using the correlation-windowing method, we can express

$$\hat{P}_x(\omega_1, \omega_2) = \sum_{m_1=-(M_1-1)}^{M_1-1} \sum_{m_2=-(M_2-1)}^{M_2-1} \hat{R}_x(m_1, m_2) w(m_1, m_2) e^{-j\omega_1 m_1} e^{-j\omega_2 m_2} \tag{5.8}$$

where $w(n_1, n_2)$ represents a 2-D window function of size $(2M_1 - 1) \times (2M_2 - 1)$. Note that $M_1 < N_1$ and $M_2 < N_2$ so that unreliable values of $\hat{R}_x(m_1, m_2)$ are excluded in computing $\hat{P}_x(\omega_1, \omega_2)$.

The window used in estimating the power spectrum of 2-D profiles is a separable 2-D Kaiser window expressed as

$$w(n_1, n_2) = \begin{cases} w(n_1)w(n_2) & \text{for } |n_1| \le M_1 - 1, \ |n_2| \le M_2 - 1 \\ 0 & \text{otherwise} \end{cases} \tag{5.9}$$

where $w(n)$ represents the 1-D Kaiser window function [39]. Since the power spectrum is nonnegative by definition, $\hat{P}_x(\omega_1, \omega_2)$ obtained from Eq. (5.8) should also have this property. However, the nonnegativity of $\hat{P}_x(\omega_1, \omega_2)$ may not be guaranteed if $w(n)$ in Eq. (5.9) is a Kaiser, Hamming, von Hann, or rectangular window. A sufficient condition to guarantee $\hat{P}_x(\omega_1, \omega_2)$ to be nonnegative for all ω_1 and ω_2 is that

$$W(\omega) \ge 0 \qquad \text{for } -\pi < \omega \le \pi \tag{5.10}$$

where $W(\omega)$ is the frequency spectrum of $w(n)$. Eq. (5.10) is satisfied when $w(n)$ is a triangular

window. Therefore, this window function can be used in Eq. (5.9) when $\hat{P}_x(\omega_1, \omega_2)$ is found to have negative values.

The power spectrum estimation method is illustrated in Figs. 5.1, 5.2, and 5.3. Fig. 5.1 shows the measured data $g_k(n_1, n_2)$ which is constructed by using 32×32 interpolated data points. The 3-D perspective plot of $g_k(n_1, n_2)$ is shown in Fig. 5.1(a) and the corresponding contour plot is depicted in Fig. 5.1(b). To simplify matters, we assume that the trend of a block of profile can be approximated by a linear trend surface given by

$$t_k(n_1, n_2) = a_0 + a_1 n_1 + a_2 n_2 \tag{5.11}$$

where a_0, a_1, and a_2 are constant coefficients of this first-order bivariate polynomial. In order to estimate these coefficients, $t_k(n_1, n_2)$ was fitted to $g_k(n_1, n_2)$ in the least-squares sense, and the values $a_0 = 7.37$, $a_1 = 8.41 \times 10^{-2}$, and $a_2 = 1.03 \times 10^{-1}$ were obtained. By using Eq. (5.3), $x_k(n_1, n_2)$ can be determined. Fig. 5.2(a) shows a 3-D perspective plot of $x_k(n_1, n_2)$ and Fig. 5.2(b) shows the corresponding contour plot.

To obtain $\hat{P}_x(\omega_1, \omega_2)$, we first estimated the 2-D autocorrelation sequence by using Eq. (5.7). A 2-D Kaiser window of size 53×53 ($M_1 = M_2 = 27$) was then applied to $\hat{R}_x(m_1, m_2)$. The shape parameter α of the Kaiser window was chosen to be 4. The 2-D discrete-time Fourier transform in Eq. (5.8) was then implemented to obtain $\hat{P}_x(\omega_1, \omega_2)$ and the result is shown in Fig. 5.3. Fig. 5.3(a) shows the power spectrum with values ranging from 0 to -50 dB, Fig. 5.3(b) shows the upper part of the spectrum with values ranging from 0 to -20 dB, and Fig. 5.3(c) illustrates the contour plot of the spectrum shown in Fig. 5.3(a).

The x- and y-axes variables ν_1 and ν_2 shown in Fig. 5.1(c) represent normalized spatial frequencies in the east and north directions, respectively, which are defined as $\nu_1 = \omega_1 L_1/\pi$ and

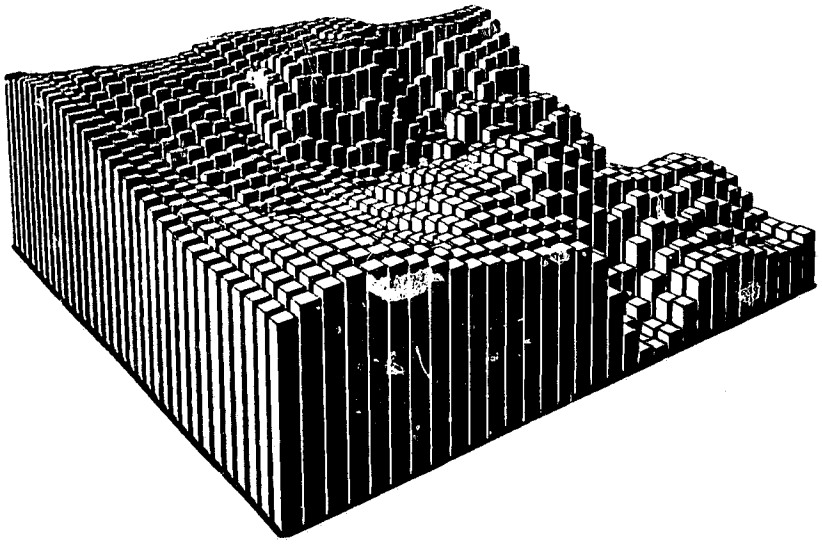

(a)

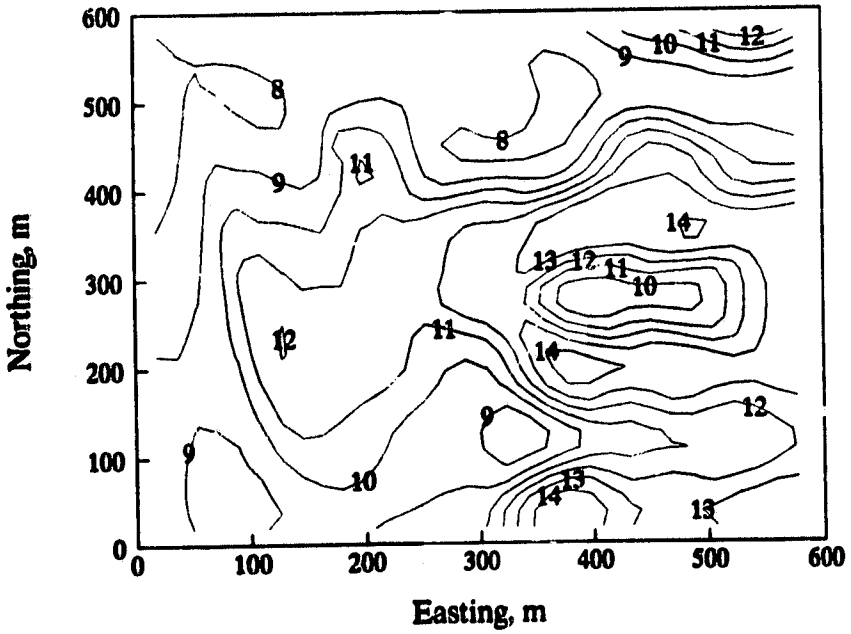

(b)

Fig. 5.1 Measured profile $g_k(n_1, n_2)$: (a) 3-D perspective plot; (b) contour plot (numbers shown are in meters).

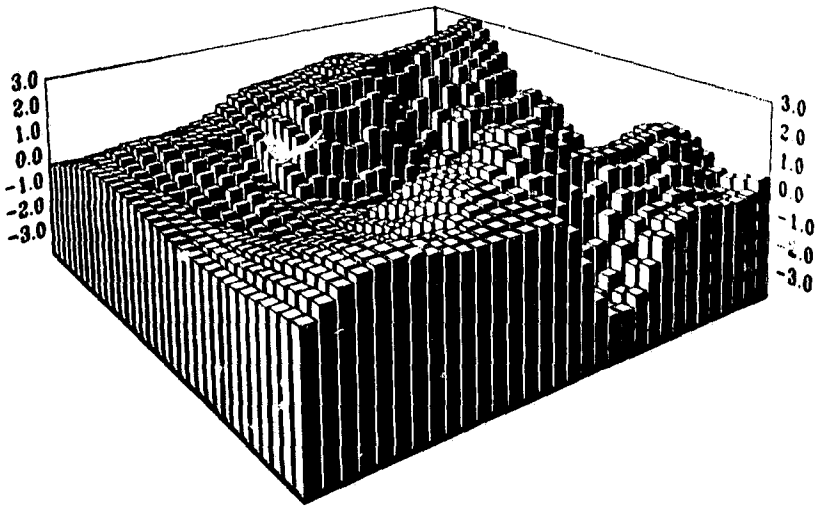

(a)

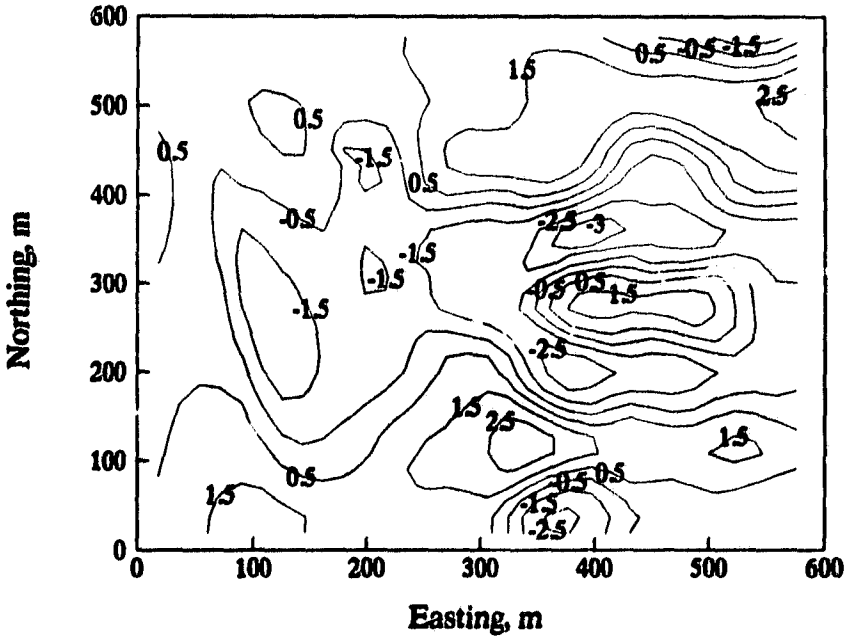

(b)

Fig. 5.2 Detrended profile $x_k(n_1, n_2)$: (a) 3-D perspective plot; (b) contour plot (numbers shown are in meters).

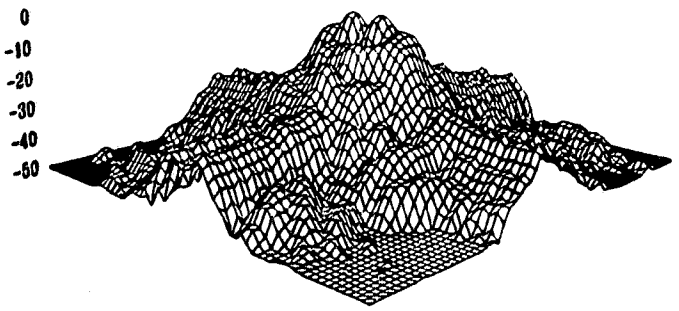

(a)

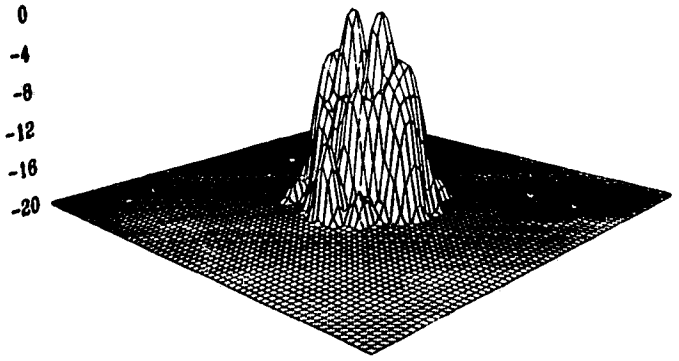

(b)

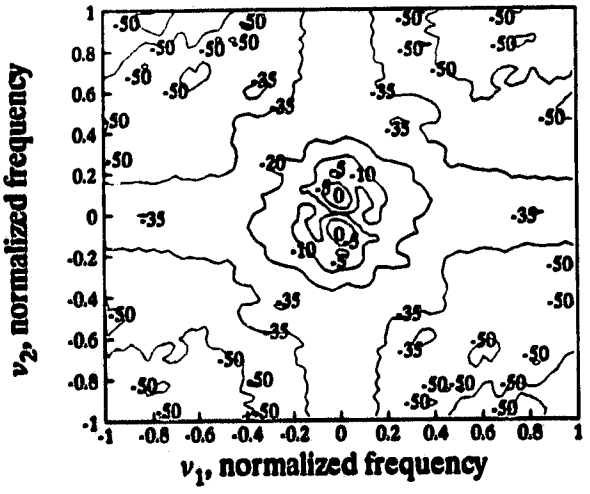

(c)

Fig. 5.3 2-D power-spectrum estimate $\hat{P}_x(\nu_1, \nu_2)$: (a) 3-D surface plot (0 to −50 dB); (b) 3-D surface plot (0 to −20 dB); and (c) contour plot (0 to −50 dB).

$\nu_2 = \omega_2 L_2/\pi$. The spatial frequencies ω_1 and ω_2 are in rad/m and L_1 and L_2, which denote the spatial distances between the interpolated points in the east and north directions, respectively, are in meters. In the example, both $L_1 = L_2 = 18$ m. In Fig. 5.3, we see that the energy of $x(n_1, n_2)$ is concentrated in the low-frequency region and slowly decreases as ν_1 and ν_2 increase. From our experimental study, we find that this is typical for $x(n_1, n_2)$ when $t_k(n_1, n_2)$ is represented by a first-order polynomial expressed in Eq. (5.11). Based on this observation, we conclude that 2-D lowpass filters should be used to reduce wideband noise in $x(n_1, n_2)$.

5.2.2 Filtering procedure, results, and discussions

Finite-duration impulse response (FIR) filters have been chosen in our implementation since they are always stable and can have zero phase response. If our objective is to place the same emphasis on each spatial direction in filtering, the frequency response should approximate a circularly symmetric function. Consider the desired frequency response of a circularly symmetric lowpass filter defined by

$$H_d(\omega_1, \omega_2) = \begin{cases} 1 & \text{for } \sqrt{\omega_1^2 + \omega_2^2} \le \omega_c \\ 0 & \text{for } \sqrt{\omega_1^2 + \omega_2^2} > \omega_c,\ |\omega_1|, |\omega_2| < \pi \end{cases} \tag{5.12}$$

where ω_c is the cutoff frequency of the digital filter. Applying the 2-D Fourier series to $H_d(\omega_1, \omega_2)$ in Eq. (5.12) yields the desired impulse response

$$h_d(n_1, n_2) = \frac{\omega_c}{2\pi\sqrt{n_1^2 + n_2^2}} J_1(\omega_c \sqrt{n_1^2 + n_2^2}) \tag{5.13}$$

where $J_1(\cdot)$ represents the Bessel function of the first kind and the first order. To obtain an FIR filter of finite order, a 2-D window function should be applied to $h_d(n_1, n_2)$ in Eq. (5.13) as

$$h(n_1, n_2) = h_d(n_1, n_2)w(n_1, n_2) \tag{5.14}$$

For a zero-phase 2-D digital filter with real impulse response, $h_d(n_1, n_2)$ and $w(n_1, n_2)$ must be symmetric with respect to the origin, i.e.,

$$h_d(n_1, n_2) = h_d(-n_1, -n_2)$$
$$w(n_1, n_2) = w(-n_1, -n_2)$$

Let **C** represent the region of support of $h(n_1, n_2)$. If we choose **C** to be the set of samples

$$\mathbf{C} = \{(n_1, n_2): -5 \le n_1, n_2 \le 5\} \tag{5.15}$$

the resulting filter is an (11×11)-point FIR filter. In general, a lowpass filter with a larger support region has better characteristics in terms of smaller transition width and smaller deviation from the desired frequency response. However, in our case, the results have shown that the size of **C** in Eq. (5.15) is sufficient for the application at hand.

The 2-D window used in the design of the lowpass filter is a circularly symmetric Kaiser window [76] which has the region of support **C** defined in Eq. (5.15). The shape parameter of the Kaiser window α was chosen as 1.5 and the resulting filter has at least 25-dB attenuation in the stopband.

Referring to Eq. (5.4), $x(n_1, n_2)$ at the kth block is composed of the signal $l_k(n_1, n_2)$ and the wideband noise $v_k(n_1, n_2)$. In order to reduce a large amount of noise at the expense of reducing a small amount of signal, the cutoff frequency of the lowpass filter should be chosen as the frequency at which the signal power decreases to a level which is close to the noise-power level. By using this value of cutoff frequency in lowpass filtering, high-frequency components which are mainly due to noise will be largely attenuated and low-frequency components which are mainly due to signal will be preserved. In order to determine such a cutoff frequency, we assume that the noise level of $v_k(n_1, n_2)$ is 20 dB below the maximum signal level of $l_k(n_1, n_2)$ in the power spectrum. In other words, if we normalize $\hat{P}_x(v_1, v_2)$ so that the maximum value has 0 dB, then v_c is the frequency at which $\hat{P}_x(v_1, v_2) =$

= −20 dB where $\nu_c = \omega_c L/\pi$ represents the normalized cutoff frequency and $L = L_1 = L_2$ represents the spatial distance. Since $\hat{P}_x(\nu_1, \nu_2)$ is a 2-D spectrum estimate, the frequencies at which $\hat{P}_x(\nu_1, \nu_2) = -20$ dB constitute a contour in the (ν_1, ν_2) plane. Therefore, in order to determine ν_c, we first estimate the contour with the value of −20 dB in $\hat{P}_x(\nu_1, \nu_2)$. Next, a circle is fitted to this contour in the least-squares sense and the radius of this circle then provides an estimate of ν_c. Fig. 5.4(a) illustrates the −20-dB contour of $\hat{P}_x(\nu_1, \nu_2)$ obtained from Fig. 5.3(c). By determining the radius of the best-fit circle, we found that $\nu_c = 0.36$. Fig. 5.4(b) shows the frequency response of the designed 2-D lowpass filter.

Note that there may be more than one −20-dB contour estimated from $\hat{P}_x(\nu_1, \nu_2)$ for a particular block of profile. Should this happen, our criterion is to select the outermost −20-dB contour that surrounds the origin of the (ν_1, ν_2) plane. We select the outermost contour because our interest is to preserve as much signal as possible in the noise-reduction process. We choose the contour that surrounds the origin of the (ν_1, ν_2) plane in order to ensure that fluctuations in the spectrum estimate will not affect the procedure in determining the cutoff frequency.

Let

$$y(n_1, n_2) = h(n_1, n_2) * x(n_1, n_2) \tag{5.16}$$

be the output of the lowpass filter where $h(n_1, n_2)$ represents the impulse response of the filter with $\nu_c = 0.36$. The smoothed version of the profile can be obtained by combining the trend component $t(n_1, n_2) = t_k(n_1, n_2)$ in Eq. (5.11) with $y(n_1, n_2)$ in Eq. (5.16) as

$$s(n_1, n_2) = t(n_1, n_2) + y(n_1, n_2) \tag{5.17}$$

The smoothed profile in Eq. (5.17) is shown in Fig. 5.5(a). To facilitate comparison, the measured data $g(n_1, n_2) = g_k(n_1, n_2)$ is also shown in the figure. We observe that, as a result of lowpass filtering,

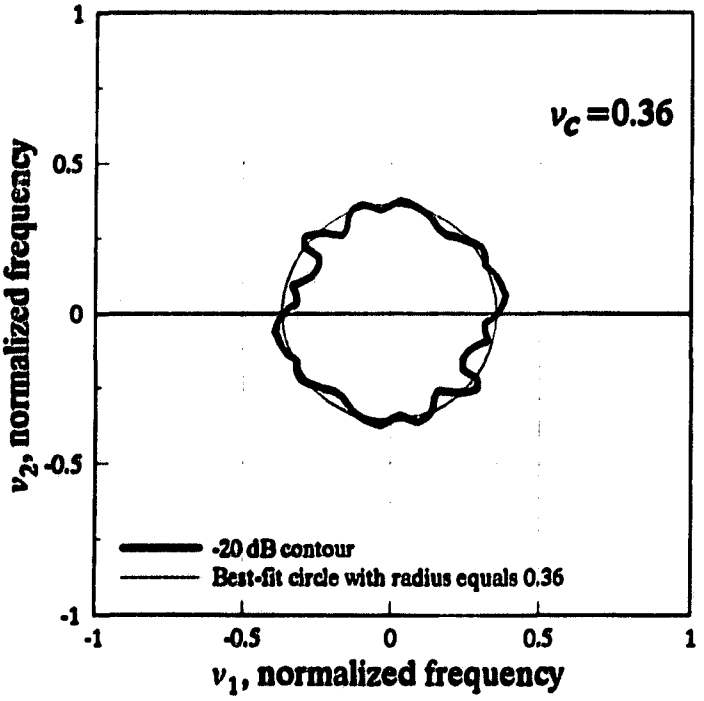

(a)

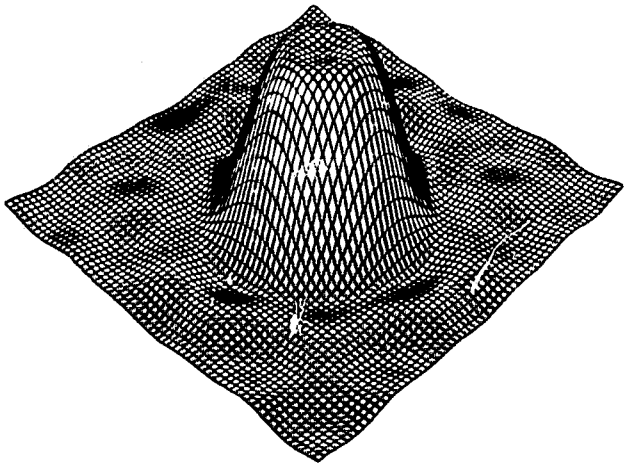

(b)

Fig. 5.4 Design of 2-D lowpass filters: (a) method to determine the cutoff frequency of a lowpass filter; (b) frequency response of the lowpass filter designed with ν_c = 0.36.

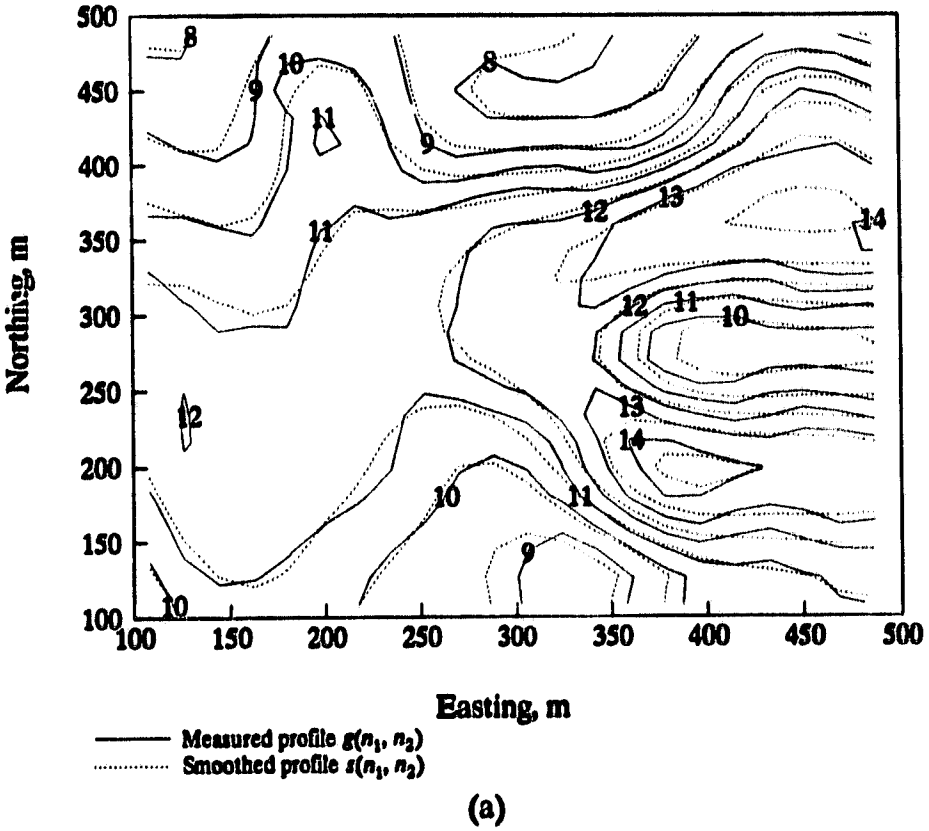

Fig. 5.5 Filtering of wideband noise: (a) comparison of the smoothed profile $s(n_1, n_2)$ with the measured profile $g(n_1, n_2)$.

the contour lines correspond to $s(n_1, n_2)$ appear to be smoother than those corresponding to $g(n_1, n_2)$. On the other hand, since the cutoff frequency is chosen specific to this block of data, the underlying structure of the profile is maintained after filtering.

To reconstruct the topography, we have applied 2-D interpolation to $s(n_1, n_2)$ to increase the definition of the profile. Fig. 5.5(b) shows the data $g(n_1, n_2)$ according to the x- and y-ranges as defined in Fig. 5.5(a). Fig. 5.5(c) shows the high-definition profile of $s(n_1, n_2)$ in the same area.

5.3 2-D FILTERING BASED ON MINIMUM MEAN-SQUARED ERROR ESTIMATION

In Section 5.2, we have developed a method to filter bathymetric profiles on a block-by-block basis. Within a block, we assume that the profile is widesense stationary so that Eq. (5.5) can be used to compute the power spectrum. Using a larger block size generally reduces the variance of the power-spectrum estimate and hence the cutoff frequency determined from the spectrum estimate for this block of profile would be more appropriate. On the other hand, since the same filter will be applied to this larger block, the preservation of signal in the filtering may be less effective in areas where the signal characteristics vary rapidly. Our objective in this section is to discuss a 2-D filtering technique whereby filtering is carried out on a point-by-point basis so that noise reduction can be adapted to each data point. In terms of signal preservation, this type of filtering can be more effective compared to the method described in Section 5.2.

To begin with, we assume that (1) a 2-D measured profile is a sample of a 2-D random process, (2) the noise is white and additive, and (3) the sea-floor relief is a nonstationary random process. As in Section 5.2, let R be the region of interest and

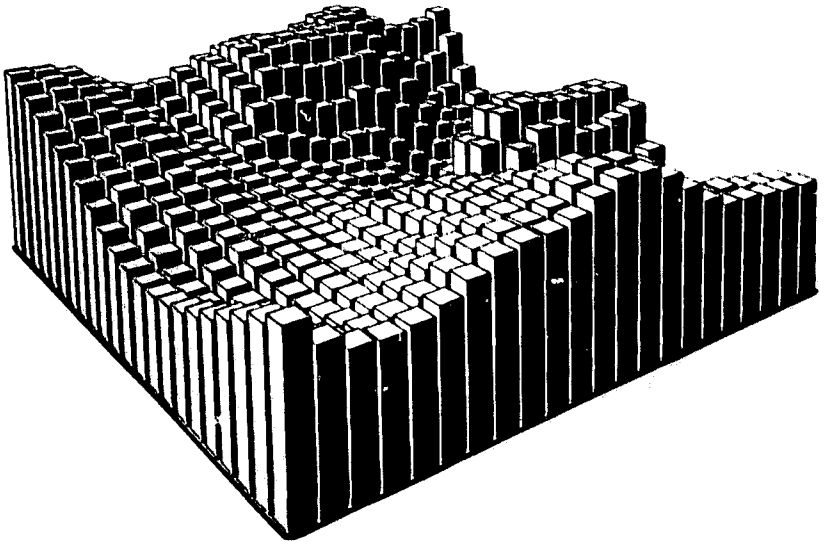

(b)

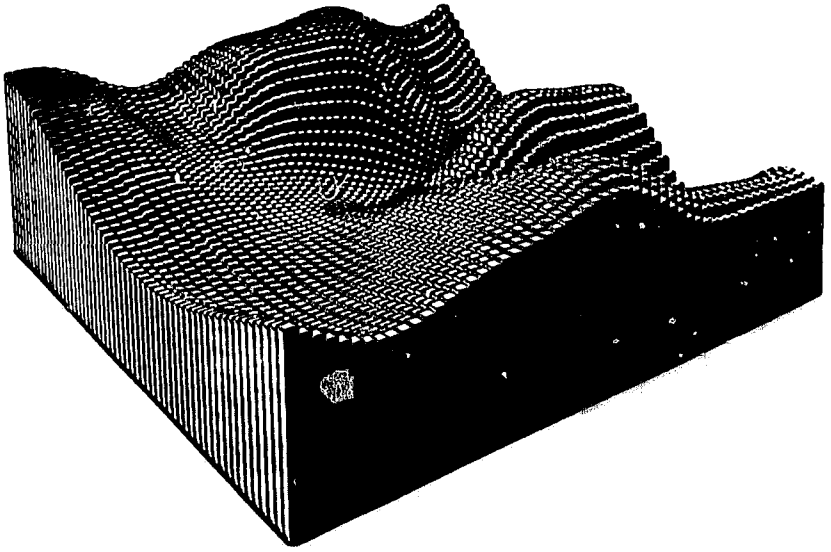

(c)

Fig. 5.5 Filtering of wideband noise: (b) measured profile $g(n_1, n_2)$; (c) high-definition profile of $s(n_1, n_2)$.

$$g(n_1, n_2) = f(n_1, n_2) + v(n_1, n_2) \tag{5.18}$$

for $n_1, n_2 \in R$ be the measured data, which is again the interpolated profile in our problem. Eq. (5.18) can be written in a compact form by using lexicographic ordering [77]. For example, $g(n_1, n_2)$ for $n_1 = 1, 2, \ldots, N_1$ and $n_2 = 1, 2, \ldots, N_2$ can be converted to a column vector of length $N_1 \times N_2$ as

$$\mathbf{g} = [g_1, g_2, \ldots, g_{N_1}]^T$$

where

$$g_i = [g_{i1} \; g_{i2} \; \cdots \; g_{iN_2}]$$

By using this notation, Eq. (5.18) can be written as

$$\mathbf{g} = \mathbf{f} + \mathbf{v} \tag{5.19}$$

The goal is to estimate $\mathbf{f}$ based on $\mathbf{g}$ by using a linear estimator such that the estimated profile $\hat{\mathbf{f}}$ is as close to $\mathbf{f}$ as possible. Many objective criteria exist to evaluate $\hat{\mathbf{f}}$ and the criterion that minimizes the mean-squared error between $\hat{\mathbf{f}}$ and $\mathbf{f}$ is used in our problem. Mathematically, $\hat{\mathbf{f}}$ should be derived such that $E[(\hat{\mathbf{f}} - \mathbf{f})^2]$ is the minimum.

The derived linear minimum mean-squared error estimator depends only on the first and second-order statistics, which can be expressed as [78]

$$\hat{\mathbf{f}} = E[\mathbf{f}] + \mathbf{C}_{fg}\mathbf{C}_g^{-1}(\mathbf{g} - E[\mathbf{g}]) \tag{5.20}$$

where $E[\cdot]$ is the expectation of $[\cdot]$,

$$\mathbf{C}_{fg} = E[(\mathbf{f} - E[\mathbf{f}])(\mathbf{g} - E[\mathbf{g}])^T]$$

is the cross-covariance matrix between $\mathbf{f}$ and $\mathbf{g}$, and

$$\mathbf{C}_g = E[(\mathbf{g} - E[\mathbf{g}])(\mathbf{g} - E[\mathbf{g}])^T]$$

is the covariance matrix of $\mathbf{g}$.

As mentioned in Section 4.1, the noise in a 2-D profile mainly arises from three sources: the LIDAR system, the sea state, and the geographical positioning of laser soundings. Since these sources have no direct relationship with the ocean topography, we assume that the noise is independent of the signal. With this assumption and the assumption that noise has zero mean, we can write

$$\mathbf{C}_{fg} = \mathbf{C}_f \qquad \text{and} \qquad \mathbf{C}_g = \mathbf{C}_f + \mathbf{C}_v \tag{5.21}$$

where $\mathbf{C}_f$ and $\mathbf{C}_v$ are the covariance matrices of $\mathbf{f}$ and $\mathbf{v}$, respectively. Substituting Eq. (5.21) into Eq. (5.20) yields

$$\hat{\mathbf{f}} = E[\mathbf{f}] + \mathbf{C}_f (\mathbf{C}_f + \mathbf{C}_v)^{-1} (\mathbf{g} - E[\mathbf{g}]) \tag{5.22}$$

As a result, a nonstationary-mean, nonstationary-covariance model for $\mathbf{f}$ and $\mathbf{v}$ must be specified in order to obtain $\hat{\mathbf{f}}$. While this model serves our purpose, rapid computation of $\hat{\mathbf{f}}$ is unlikely to be achieved since Eq. (5.22) involves computations of large matrices. Furthermore, the underlying models for the distribution of $\mathbf{f}$ and $\mathbf{v}$ must be specified.

One way to reduce the complexity of $\hat{\mathbf{f}}$ is to assume that $\mathbf{C}_f$ is diagonal so that the original model can be reduced to a nonstationary-mean, nonstationary-variance model, which was first established in [79]. When this model is applied to sea-bed topography, we can say that the gross structure of the topography is carried by the nonstationary mean of $\mathbf{f}$, whereas the nonstationary variance of $\mathbf{f}$ provides a statistical measure of the local roughness of the sea floor, which, in turn, provides information on the local fluctuations of the relief. While the characterization may not provide a sufficient description of the behavior of the ocean floor, we will show that its use in Eq. (5.22) will lead to a workable 2-D filter that does not require computations of large matrices and, more importantly, can give rise to reasonable and useful results.

According to Eq. (5.22), the sea-depth estimate at location (n_1, n_2) can be expressed as

$$\hat{f}(n_1, n_2) = E[f(n_1, n_2)] + \frac{\text{VAR}[f(n_1, n_2)]}{\text{VAR}[f(n_1, n_2)] + \text{VAR}[v(n_1, n_2)]} (g(n_1, n_2) - E[g(n_1, n_2)]) \tag{5.23}$$

where $E[g(n_1, n_2)] = E[f(n_1, n_2)]$ since noise is assumed to have zero mean. When the *a priori* statistics $E[f(n_1, n_2)]$, $\text{VAR}[f(n_1, n_2)]$, and $\text{VAR}[v(n_1, n_2)]$ are known, Eq. (5.23) says that $\hat{f}(n_1, n_2)$ can be obtained spatially on a point-by-point basis from the measurement $g(n_1, n_2)$.

To see the effects of the *a priori* statistics and measurement on $\hat{f}(n_1, n_2)$ more clearly, we can rearrange Eq. (5.23) as

$$\hat{f}(n_1, n_2) = \alpha g(n_1, n_2) + (1 - \alpha) E[f(n_1, n_2)] \tag{5.24}$$

where

$$\alpha = \frac{\text{VAR}[f(n_1, n_2)]}{\text{VAR}[f(n_1, n_2)] + \text{VAR}[v(n_1, n_2)]} \tag{5.25}$$

Clearly, Eq. (5.24) shows that $\hat{f}(n_1, n_2)$ is a weighted sum of the sea-depth measurement and the mean of the true bathymetric data, and the weight is determined from the variances of the true data and noise.

As in Section 2.4-C, we define the signal-to-noise (SNR) ratio as the ratio between the variance of signal and the variance of noise. In this case,

$$\text{SNR} = \frac{\text{VAR}[f(n_1, n_2)]}{\text{VAR}[v(n_1, n_2)]} \tag{5.26}$$

where SNR is now expressed in linear scale. With Eq. (5.26), we can express α in Eq. (5.25) in terms of SNR as

$$\alpha = \frac{\text{SNR}}{\text{SNR} + 1} \tag{5.27}$$

Substituting α in Eq. (5.27) into Eq. (5.24) yields

$$\hat{f}(n_1, n_2) = \frac{1}{\text{SNR} + 1} \left(\text{SNR} g(n_1, n_2) + E[f(n_1, n_2)] \right) \tag{5.28}$$

Eq. (5.28) says that when the SNR is low, i.e., SNR $\ll 1$, indicating that the noise dominates the fluctuations in the profile, then $\hat{f}(n_1, n_2) \approx E[f(n_1, n_2)]$, which means that the estimated value conforms to the gross structure of the topography rather than the noisy measurement. In effect, noise filtering is carried out. When the SNR is high, i.e., SNR $\gg 1$, indicating that the local variations are due mainly to the roughness of the ocean bottom, then $\hat{f}(n_1, n_2) \approx g(n_1, n_2)$ in Eq. (5.28), which means that the characteristics of the ocean topography are preserved in filtering. Hence, the application of Eq. (5.28) to R provides a compromise between noise reduction and preservation of detailed ocean-bottom characteristics.

5.3.1 Implementation of 2-D filtering

In ocean bathymetry, the *a priori* statistics $E[f(n_1, n_2)]$, VAR $[f(n_1, n_2)]$, and VAR $[v(n_1, n_2)]$ are not known in advance and, therefore, they must be estimated from the bathymetric profile. When we assume that the ensemble statistics in Eqs. (5.26) and (5.28) can be replaced by local spatial statistics of the profile, then

$$\begin{aligned} E[f(n_1, n_2)] &= m_f(n_1, n_2) \\ \text{VAR}[f(n_1, n_2)] &= q_f(n_1, n_2) \\ \text{VAR}[v(n_1, n_2)] &= q_v(n_1, n_2) = q_v \end{aligned} \tag{5.29}$$

where the variance of noise is assumed to be constant. By using Eq. (5.29) in Eqs. (5.26) and (5.28), we get

$$\text{SNR} = \frac{q_f(n_1, n_2)}{q_v} \tag{5.30}$$

and

$$\hat{f}(n_1, n_2) = \frac{1}{\text{SNR} + 1}\left(\text{SNR}\, g(n_1, n_2) + m_f(n_1, n_2)\right) \tag{5.31}$$

In order to provide an estimate for $m_f(n_1, n_2)$ in Eq. (5.31), we use the sample mean, i.e.,

$$\hat{m}_f(n_1, n_2) = \frac{1}{(2K+1)^2} \sum_{k_1=-(n_1-K)}^{n_1+K} \sum_{k_2=-(n_2-K)}^{n_2+K} g(k_1, k_2) \tag{5.32}$$

where $(2K+1) \times (2K+1)$ is the size of the region used in the estimation.

The variance $q_f(n_1, n_2)$ in Eq. (5.30) can be estimated from the variance of the data $g(n_1, n_2)$ as

$$\hat{q}_f(n_1, n_2) = \begin{cases} \hat{q}_g(n_1, n_2) - q_v & \text{for } \hat{q}_g(n_1, n_2) > q_v \\ 0 & \text{for } \hat{q}_g(n_1, n_2) \le q_v \end{cases} \tag{5.33}$$

where

$$\hat{q}_g(n_1, n_2) = \frac{1}{(2K+1)^2} \sum_{k_1=-(n_1-K)}^{n_1+K} \sum_{k_2=-(n_2-K)}^{n_2+K} (g(k_1, k_2) - \hat{m}_f(k_1, k_2))^2 \tag{5.34}$$

is the sample variance of $g(n_1, n_2)$ computed using a local region of size $(2K+1) \times (2K+1)$. The estimate $\hat{m}_f(n_1, n_2)$ in Eq. (5.34) can be obtained from Eq. (5.32) and q_v is assumed known.

In order to estimate q_v in our problem, we need to examine each component that constitutes the noise. Besides the three error components mentioned previously, approximation errors of 2-D interpolation may also be introduced. The approximation error of interpolation depends on the interpolation technique used. If we assume that the error introduced by the interpolation technique described in Chapter 4 is fairly small compared to other three errors then the total noise variance can be derived from each of the three individual noise variance. By using the fact that these three error sources are independent of each other, we can express

$$\hat{q}_v = \hat{q}_l + \hat{q}_s + \hat{q}_p$$

where $\hat{q}_l$ represents the variance of the measurement error in the LIDAR system, $\hat{q}_s$ the variance of the error due to sea state, and $\hat{q}_p$ the variance of the error due to the imprecision of the laser-sounding

position. Based on the findings in [80], it can be shown that

$$\hat{q}_l = 0.07 \text{ m}^2, \quad \hat{q}_s = 0.09 \text{ m}^2, \quad \text{and} \quad \hat{q}_p = 0.02 \text{ m}^2$$

for the LARSEN 500 airborne system. As a result, $\hat{q}_v = 0.18$ m^2. By substituting this value of $\hat{q}_v$ as q_v into Eq. (5.33), $\hat{q}_f(n_1, n_2)$ can be obtained. With $\hat{q}_f(n_1, n_2)$ and $\hat{q}_v$ known, an estimate of SNR can be computed from Eq. (5.31). Using this value of SNR and the estimate $\hat{m}_f(n_1, n_2)$ obtained from Eq. (5.32), we can then determine $\hat{f}(n_1, n_2)$ from Eq. (5.30). When the space-variant filter in Eq. (5.30) is applied to the whole bathymetric region, adaptive noise reduction can be achieved.

5.3.2 Filtering results and discussions

Figs. 5.6 and 5.7 illustrate an example of the application of this type of filtering to signal $g(n_1, n_2) = g_k(n_1, n_2)$ shown in Fig. 5.1. Fig. 5.6(a) and (b) show the 3-D and contour plots of the estimated variance $\hat{q}_f(n_1, n_2)$ obtained from using Eq. (5.33). The window size used for computing $\hat{m}_f(n_1, n_2)$ in Eq. (5.32) and $\hat{q}_g(n_1, n_2)$ in Eq. (5.34) was 5×5. Since both sides of the ridge at locations approximately (400 m, 320 m) and (400 m, 240 m) are relatively steep, we observe that $\hat{q}_f(n_1, n_2)$ is relatively large at these locations. In addition, since relatively steep slopes can be found at locations (360 m, 60 m) and (360 m, 400 m), $\hat{q}_f(n_1, n_2)$ at these locations are found to be quite large, which are approximately 4 m^2 and 3.5 m^2, respectively. Since the topography is relatively gentle when easting is between 160 and 240 m, $\hat{q}_f(n_1, n_2)$ is below 0.5 m^2 and the corresponding contour lines are not shown in Fig. 5.6 (b).

Fig. 5.7(a) compares the filtered profile obtained by using Eq. (5.30) with the measurement $g(n_1, n_2)$. Since the shape of the ocean bottom varies, the amount of filtering applied varies. Specifically, noise smoothing is minimal on both sides of the ridge and in sloping regions. On the other hand, smoothing is effective in areas with gentle topography as can be seen by comparing the two sets

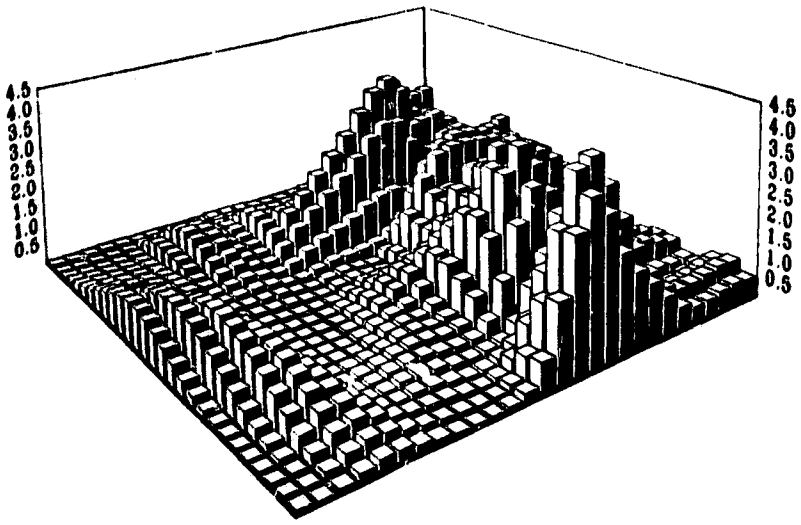

(a)

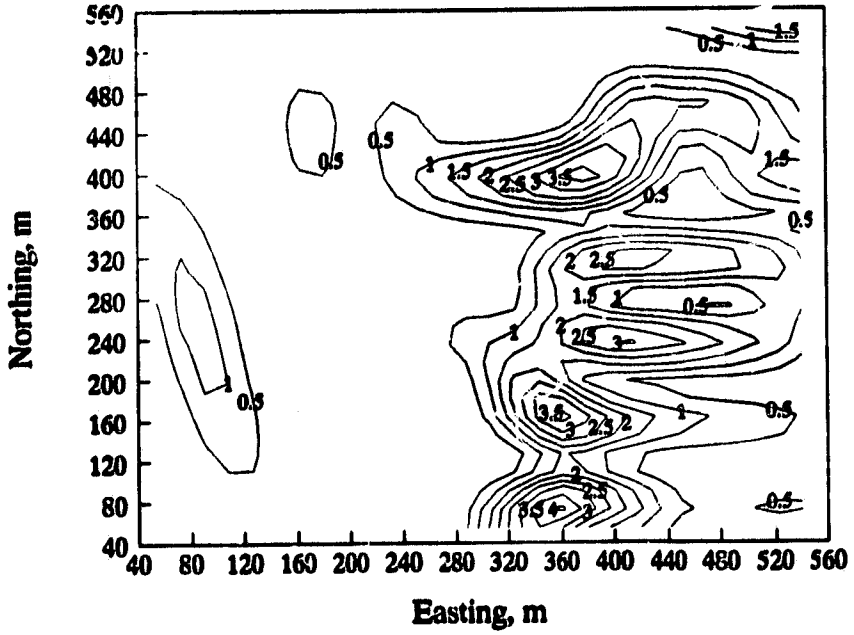

(b)

Fig. 5.6 Estimated variance $\hat{q}_f(n_1, n_2)$ (numbers shown are in square meters): (a) 3-D perspective plot; (b) contour plot.

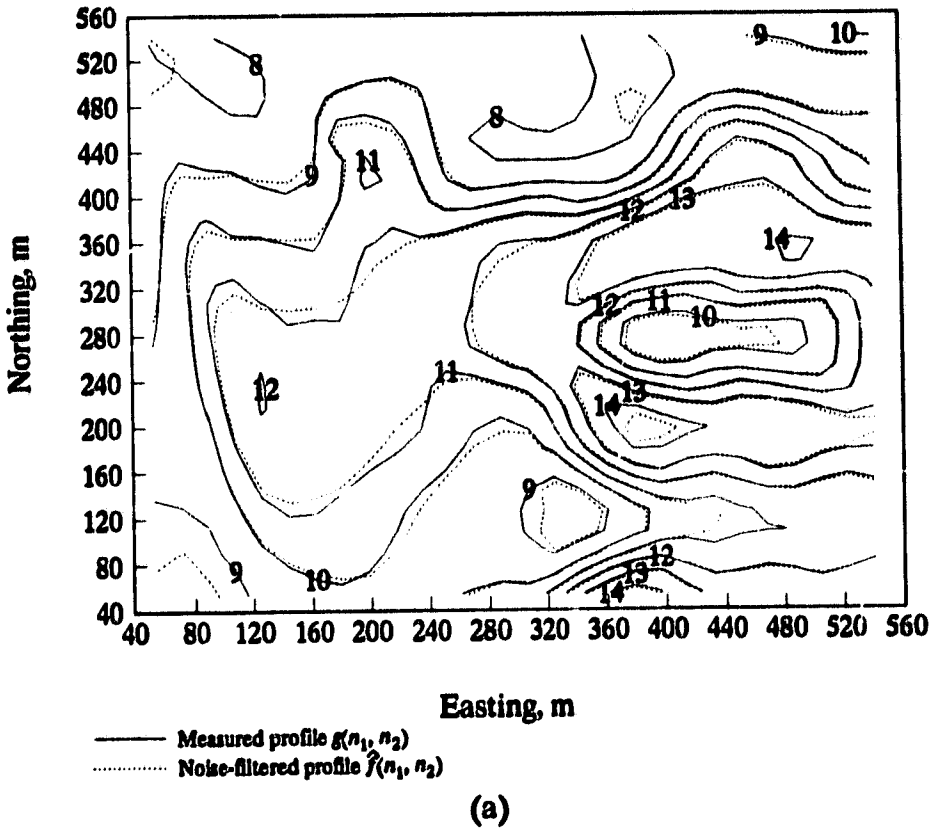

Fig. 5.7 Filtering of wideband noise: (a) comparison of the noise-filtered profile $\hat{f}(n_1, n_2)$ with the measured profile $g(n_1, n_2)$.

of contour lines at locations approximately (200 m, 160 m), (160 m, 320 m), and (280 m, 280 m). Fig. 5.7(b) shows the 3-D plot of $g(n_1, n_2)$ corresponding to the data shown in Fig. 5.7(a). Fig. 5.7(c) shows the result of applying 2-D interpolation to increase the definition of the profile $\hat{f}(n_1, n_2)$ in the same area.

To illustrate the effects of filtering more clearly, we refer to Fig. 5.8. In this figure, the residual profile

$$r(n_1, n_2) = g(n_1, n_2) - \hat{f}(n_1, n_2)$$

is plotted with the variance $\hat{q}_f(n_1, n_2)$ on the same graph. To improve readability, the contour labels for $\hat{q}_f(n_1, n_2)$ are not shown. In Fig. 5.8, we observe that $|r(n_1, n_2)| \leq 0.2$ m when $\hat{q}_f(n_1, n_2) \geq 0.5$ m^2, i.e., the amount of filtering is small in areas with high-detail features. On the other hand, we observe that when $\hat{q}_f(n_1, n_2) < 0.5$ m^2, i.e., in areas where the contour lines of $\hat{q}_f(n_1, n_2)$ are not shown, indicating that the topography is gentle, $|r(n_1, n_2)| \leq 0.4$ m is found. The amount of filtering is, therefore, larger in these areas.

5.4 CONCLUSIONS

An adaptive 2-D filtering procedure applicable to bathymetry, in particular, to airborne laser bathymetry, for the removal of wideband noise has been developed. This procedure deals with 2-D power spectral analysis of laser bathymetric profiles and the application of 2-D nonrecursive lowpass filtering with adaptive cutoff frequency. Since the filtering is carried out on a block-by-block basis, most of the signal content can be preserved while the wideband noise reduced. As the power spectral information is now available in each block of profile, one can therefore explore the use of this information to analyze the relief of the ocean, e.g., to determine the ruggedness of the ocean or to classify different features in the ocean.

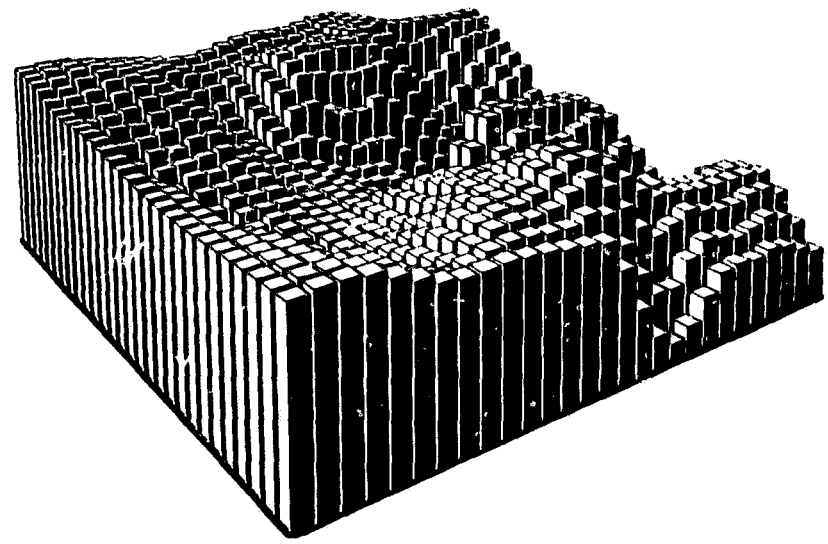

(b)

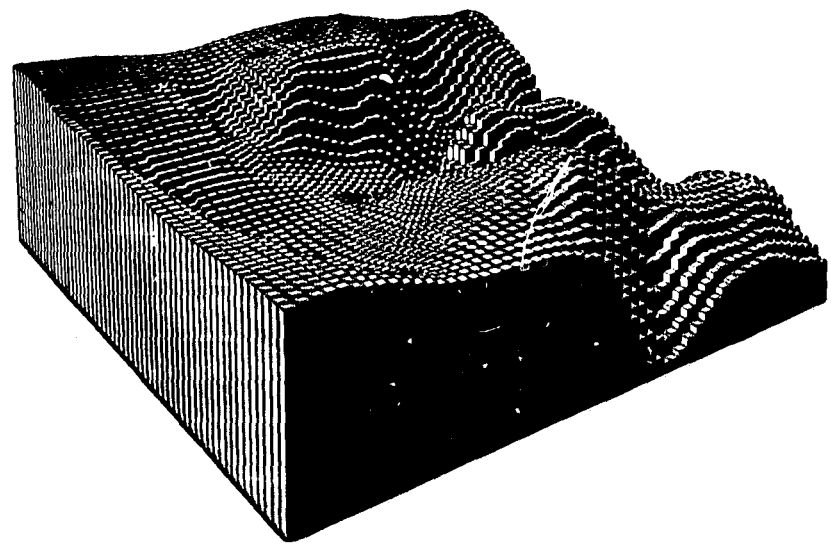

(c)

Fig. 5.7 Filtering of wideband noise: (b) measured profile $g(n_1, n_2)$; (c) high-definition profile of $\hat{f}(n_1, n_2)$.

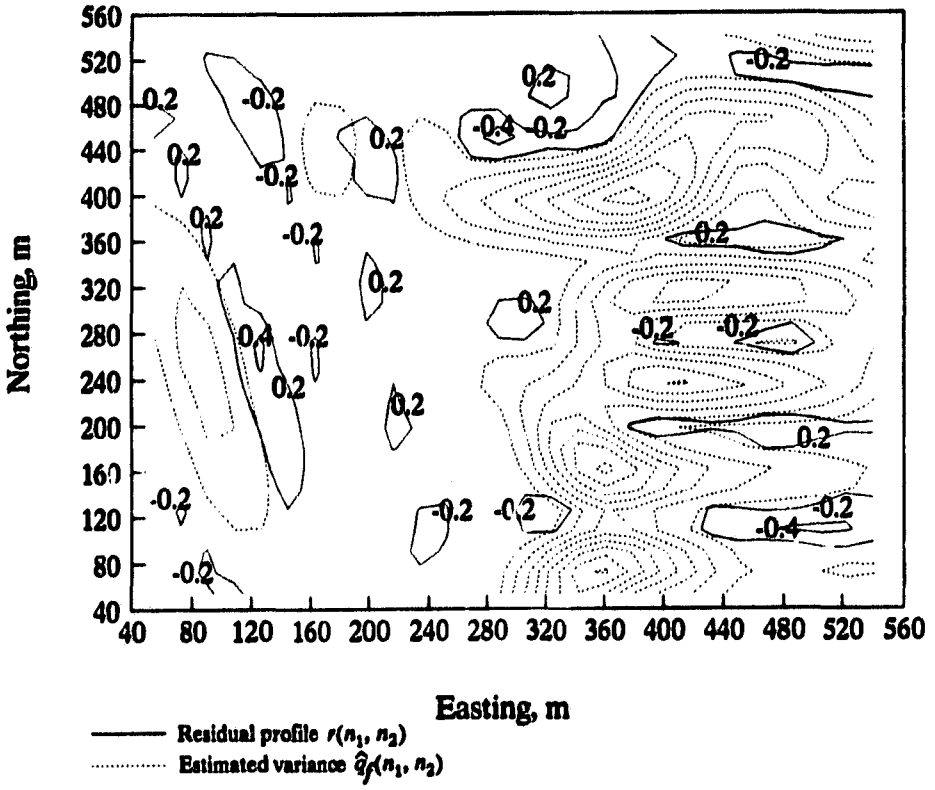

Fig. 5.8 Residual profile $r(n_1, n_2)$ overlaid with $\hat{q}_f(n_1, n_2)$ for $\hat{q}_f(n_1, n_2) \geq 0.5$ m^2 (numbers shown are in meters).

In order to remove noise and preserve rapid-changing ocean characteristics, laser bathymetric profiles have been filtered adaptively on a point-by-point basis. To do this, a nonstationary-mean, nonstationary-variance model has been adopted to characterize the sea-floor relief. It has been shown that if the noise in bathymetric profiles can be estimated accurately, a high-degree of signal preservation can be achieved in noise reduction.

CHAPTER SIX
CONCLUSIONS

We have developed a set of signal-processing algorithms which can lead to significant improvements in the reliability and efficiency of airborne laser ranging systems, in particular, the LARSEN 500 airborne system.

The thesis starts by considering the raw laser waveforms received at each sounding location and concludes by providing an accurate representation of the 3-D ocean-bottom topography. The processing involved is carried out in two phases. In phase I, 1-D processing techniques are used to process laser waveforms individually to obtain improved estimates of sea depth. These depth estimates are then improved further in phase II by employing 2-D signal processing techniques. After the application of 1-D and 2-D processing, the resulting depth profiles are considered to be accurate representations of the true sea-bed topography. Throughout the thesis, emphasis has been placed on techniques that can be automated.

The results achieved are summarized in Section 6.1 and recommendations for further research are presented in Section 6.2.

6.1 RESULTS OF THE THESIS

In Chapter 2, we have interpreted the reflections of the laser pulse from the sea as distribution curves of photons received at each time instant. We have shown that if we can preserve the moments of the reflections, we can preserve the important characteristics such as the peak position and pulse shape of the reflections. In order to preserve these characteristics and remove noise, we have applied a special class of digital smoothing filters to the received waveforms to preserve the moments up to the third

order while minimizing the variance of white noise. As a result, distortion of the original signal can be minimized in the noise-reduction process.

Next, we have examined the mathematical characterization of the smoothed laser waveforms. To characterize the waveforms received under diverse circumstances, we have established a mathematical model function that depends on seven model parameters. By varying the values of these parameters, we can vary the characteristics of the function to give a variety of profiles to resemble the received waveforms obtained from different areas. The model function can be computed numerically and by analyzing the simulated waveforms using this model function, we have shown that the resolution between the surface and bottom peaks is largely dependent on the asymmetry of the surface reflection, the pulse width of bottom reflection, and the separation between the peaks.

In Chapter 2, we have also developed two algorithms to identify the surface and bottom peaks in the LARSEN waveforms. The surface peak is detected by using a simple thresholding technique and the bottom peak is detected through the application of lowpass digital differentiation. The algorithm that incorporates the lowpass differentiation technique detects the bottom reflection and rejects noise pulses and pulses that may arise from turbid layers. Experimental results have shown the algorithm to be effective in locating the peak of the correct pulse in the presence of varying degrees of noise.

In Chapter 3, we have formulated an approach to perform the decomposition of each waveform into separate components representing the surface and bottom reflections. The decomposition is implemented by using the Levenberg-Marquardt optimization method. In order to assure convergence from almost any starting point, we have used the trust-region approach to update the search direction and step length in each iteration. We have also developed an initialization scheme that can provide good initial estimates to the model parameters; as a result, the amount of computation required in the

optimization has been reduced quite significantly. Results have shown that accurate decomposition of the LARSEN waveforms is possible, which can lead to significant improvement in the accuracy of the depth information.

In the second part of Chapter 3, we have performed a detailed comparative study of sea-depth estimates obtained from the waveform decomposition with corresponding estimates obtained by a surveying company. From the statistical analysis, we have observed a high degree of agreement between the two sets of results. When the resolution between the surface and bottom reflections is low, which is typical when the sea water is turbid and/or when the water is shallow, we have found that the proposed decomposition technique offers a significant improvement in the sea-depth estimates. The chapter concludes with a number of suggestions of the other applications of the optimization results.

In Chapter 4, we have developed a type of 2-D interpolating filter to filter impulsive noise present in the scattered depth estimates. The filtering is performed in two stages. In the first stage, we have extended the concept of order-statistics filtering to detect rogue sea-depth measurements that are irregularly spaced in a 2-D domain. In the second stage, we have replaced rogue measurements by more reasonable values that conform to the local topographical structure of the sea floor through the application of a sophisticated 2-D interpolation technique. As a result of the filtering, the representation of the sea-bed topography, which can be in the form of 2-D contour maps or 3-D surface plots, becomes more consistent with the nature of the ocean bottom.

In order to reconstruct the 2-D depth profiles representing the sea floor, we have applied a triangle-based 2-D interpolation technique to the scattered measurements by first constructing an optimal triangulated-irregular network from these measurements. The depth profiles are generated with respect to various sizes of the regularly spaced grids so that maps of higher resolution can be obtained.

This interpolation technique has been applied to typical bathymetric data to estimate sea depths and has been shown to yield accurate results.

In Chapter 4, we have utilized the interpolation technique to assess the accuracy of the decomposition results when the corresponding results are not available from the surveying company, due to poor resolution between the laser reflections.

In Chapter 5, we have enhanced the reconstructed profiles by applying two adaptive 2-D filtering procedures to the bathymetric profiles. In the first approach, we filter the data on a block-by-block basis by examining the 2-D power spectrum estimated in each block. With the knowledge that the energy of the depth profiles is mainly concentrated in the low-frequency region, we have formulated an approach to filter wideband noise by using 2-D lowpass filtering with adaptive cutoff frequency. In the second approach, we filter the depth profiles based on minimum mean-squared error estimation. We have shown that the derived filter is a space-variant filter and the filtering can be performed on a point-by-point basis so that noise reduction can be adapted to each data point. Results obtained show that these two filtering procedures are effective in eliminating wideband noise inherent in the 2-D bathymetric data which is difficult to detect and eliminate in 1-D processing.

6.2 RECOMMENDATIONS FOR FURTHER RESEARCH

In order to achieve the ultimate goal of real-time bathymetric charting, it is desirable to implement the developed algorithms in hardware, for example, in the form of customized VLSI chips. Mapping VLSI into bathymetric signal-processing applications offers inexpensive computing power as well as enables the use of massive parallelism inherent in the developed signal-processing algorithms. To achieve this, one may first conduct studies to determine the exact data throughput and storage requirements of the processing algorithms. One can then evaluate current VLSI-oriented architectures such as systolic arrays

and wavefront arrays and investigate the appropriate architecture for the implementation. In order to take full advantage of the parallel-processing capabilities of the VLSI architecture, one may also adapt the developed algorithms to the parallel-computing environment and evaluate the effects of the architecture on the algorithm efficiency.

Another research area is to investigate a mathematical characterization of the topographic configuration of the ocean bottom by taking the morphology of the sea floor into account. Depending on the application needs, the topography can be characterized in a deterministic or stochastic fashion. The deterministic characterization can be useful for studying many aspects of ocean dynamics, e.g., the propagation of ocean waves in coastal areas. In addition, it may also be useful to study the nature of the geologic processes acting to form the sea floor. On the other hand, the stochastic characterization can be useful for investigating the morphology of the small-scale bathymetric features, which can be important to coastal and ocean engineering.

As discussed in Chapter 3, the shape of the backscatter envelope in a waveform varies closely with the optical properties of the sea, which are, in turn, mainly determined by the sea-water turbidity. Since the laser signature has been quantified in 1-D processing, one may wish to conduct a study to systematically investigate the changes of the laser signature, essentially in the backscatter envelope, as a result of the changes of the optical properties of the sea. Research results of this study may provide a fundamental linkage between optical properties and laser signature and by using this linkage, the feasibility of direct measurement of water turbidity using airborne LIDAR systems can be ascertained.

To reduce the massive amount of data that is typically collected in airborne bathymetric surveys, two data-reduction methods can be suggested. One is to estimate sea depth in real time so that only the depth estimates, instead of the entire laser waveforms, are stored. The second method is to perform

real-time waveform decomposition so that both the sea-depth estimates and the model parameters that provide information about each waveform are stored. Nevertheless, in some occasions, it may be necessary to collect raw laser waveforms for post-mission processing in order to evaluate, for example, the performance of the LIDAR system and the quality of the laser waveforms received during surveys, and explore other potential uses of the waveforms such as in turbidity measurement. The laser data obtained on board the aircraft can be significantly reduced in size without affecting the original information through the application of advanced data compression. In view of this, one may wish to develop appropriate data-compression algorithms for bathymetry and implement the algorithms in the form of dedicated integrated-circuit chips so that real-time bathymetric data compression can be achieved.

In estimating sea depths by means of the waveform-decomposition technique, a deterministic approach is used to estimate the parameters of the established model function. To explore this further, one may wish to consider the statistical aspects of this data-modeling problem. For instance, one may estimate the uncertainties involved in the data measurements and incorporate this estimation in the optimization process. One can also establish confidence limits on each estimated parameter and utilize this information in 2-D interpolation so as to provide a quantitative assessment of the bathymetric surface in a statistical sense.

REFERENCES

[1] R. J. Urick, *Principles of Underwater Sound*, McGraw-Hill, New York, 1967.

[2] G. Haines, *Sound Underwater*, Crane Russak, New York, 1974.

[3] D. G. Tucker and B. K. Gazey, *Applied Underwater Acoustics*, Pergamon Press, Oxford, 1966.

[4] D. W. Colvin, L. D. Ward, M. J. Purches and W. Q. B. Monkhouse, "Performance evaluation of an advanced sonar in hydrographic surveying and offshore operations," *Proc. Offshore Tech. Conf.*, pp. 459-473, May 1982.

[5] K. Muirhead and A. P. Cracknell, "Airborne lidar bathymetry: review article," *Int. J. Remote Sensing*, vol. 7, no. 5, pp. 597-614, 1986.

[6] A. H. Benny and G. J. Dawson, "Satellite imagery as an aid to bathymetric charting in the Red Sea," *The Cartogr. J.*, vol. 20, no. 1, pp. 5-10, 1983.

[7] G. D. Hickman and J. E. Hogg, "Application of an airborne pulsed laser for near shore bathymetry measurements," *Remote Sensing Environ.*, vol. 1, pp. 47-58, 1969.

[8] S. Q. Duntley, "Light in the sea," *J. Opt. Soc. Amer.*, vol. 53, no. 2, pp. 214-233, 1963.

[9] W. Rattman and T. Smith, "Lasers for depth sounding and underwater viewing," Hydrospace, pp. 57-59, Feb. 1972.

[10] C. Bressel, I. Itzkan, J. E. Nunes, and F. Hoge, "Airborne oceanographic lidar system," *Proc. 11th Int. Symp. Remote Sensing Environ.*, vol. II, pp. 1259-1269, 1977.

[11] F. E. Hoge, R. N. Swift, and E. B. Frederick, "Water depth measurement using an airborne pulsed neon laser system," *Appl. Opt.*, vol. 19, pp. 871-883, March 1980.

[12] S. P. Haimbach, H. C. Mesick, H. J. Byrnes, and G. D. Hickman, "Optical bathymetry for the U. S. Navy: A field measurement program," *Proc. Ocean Optics IX*, pp. 46-51, 1988.

[13] J. E. Clegg and M. F. Penny, "Depth sounding from the air by laser beam," *J. Navig.*, vol. 31, no. 52, pp. 52-61, 1978.

[14] M. F. Penny, R. H. Abbot, D. M. Philips, B. Billard, D. Rees, and D. W. Faulkner, "Airborne laser hydrography in Australia," *Appl. Opt.*, vol. 25, pp. 2046-2058, July 1986.

[15] M. F. Penny, B. Billard, and R. H. Abbot, "LADS — the Australian laser airborne depth sounder," *Int. J. Remote Sensing*, vol. 10, pp. 1463-1479, 1989.

[16] H. S. Lee and N. T. O'Neill, "LIDAR return pulse profile and its relationship to water optical parameters," *Proc. 7th SPIE Conf. Ocean Opt.*, pp. 297-305, June 1984.

[17] R. A. O'Neil, "Field trials of a lidar bathymeter in the Magdalen Islands," *Proc. 4th Laser Hydrography Symp.*, pp. 56-84, Sept.-Oct. 1980.

[18] M. J. Casey, "Deploying the lidar on hydrographic surveys," *Proc. 9th Canadian Symp. Remote Sensing*, pp. 165-175, 1984.

[19] A. K. Malone, M. J. Casey, and D. Monahan, "Scanning LIDAR bathymeter (1) deployment strategies," *Lighthouse*, no. 27, pp. 2-6, 1983.

[20] M. J. Casey, D. Monahan, and A. K. Malone, "Scanning LIDAR bathymeter (2) data processing," *Lighthouse*, no. 27, pp. 8-12, 1983.

[21] J. Banic, S. Sizgoric, and R. O'Neil, "Scanning lidar bathymeter for water depth measurement," *Proc. SPIE, Laser Radar Technology and Applications*, vol. 663, pp.187-195, 1986.

[22] S. Svanberg, "Lasers as probes for air and sea," *Contemp. Phys.*, vol. 21, pp. 541-577, 1981.

[23] D. M. Phillips and B. W. Koerber, "A theoretical study of an airborne laser technique for determining sea water turbidity," *Australian J. Phys.*, vol. 37, no. 35, pp. 2046-2058, 1984.

[24] G. C. Guenther and R. W. L. Thomas, "Effects of propagation-induced pulse stretching in airborne laser hydrography," *Proc. SPIE, Ocean Optics VII*, vol. 489, pp. 287-296, 1984.

[25] G. C. Guenther and R. W. I. Thomas, "Simulations of the impact of inhomogeneous water columns on the temporal stretching of laser bathymeter pulses," *Proc. 7th SPIE Conf. Ocean Opt.*, Monterey, California, pp. 287-296, June 1984.

[26] H. H. Kim, "Airborne bathymetric charting using blue-green lasers," *Appl. Opt.*, vol. 16, pp. 46-56, Jan. 1977.

[27] G. C. Guenther and H. C. Mesick, "Automated lidar waveform processing," *Proc. Ocean Optics IX*, pp. 52-59, 1988.

[28] B. Billard and P. J. Wilsen, "Sea surface and depth estimation in the WRELADS airborne depth sounder," *Appl. Opt.*, vol. 25, pp. 2059-2066, July 1986.

[29] G. A. Korn and T. M. Korn, *Mathematical Handbook for Scientists and Engineers*, McGraw-Hill, N.Y., 1961.

[30] H. Geiger and K. Scheel, eds., *Handbuch der Physik*, vol. III, J. Springer, Berlin, 1928.

[31] H. W. Schüssler and P. Steffen, "Some Advanced Topics in Filter Design," *Advanced Topics in Signal Processing*, J. S. Lim and A. V. Oppenheim, eds., Prentice-Hall, N.J., 1988.

[32] F. E. Hoge and R. N. Swift, "Airborne detection of oceanic turbidity cell structure using depth-resolved laser-induced water Raman backscattering," *Appl. Opt.*, vol. 22, no. 23, pp. 3778-3786, 1983.

[33] J. L. Bufton, F. E. Hoge, and R. N. Swift, "Airborne measurements of laser backscatter from the ocean surface," *Appl. Opt.*, vol. 22, no. 17, pp. 2603-2618, 1983.

[34] A. P. Ivanov, A. L. Skrelin, and I. D. Sherbaf, "Investigation of optical characteristics of aqueous media by the pulsed probing method," *J. Appl. Spectrosc. (USSR)*, vol. 17, pp. 1087-1092, 1974.

[35] M. Abramowitz and I. A. Stegun, eds., "*Handbook of mathematical functions*," Applied Mathematics Series, No. 55, National Bureau of Standards, Washington, D.C., pp. 299, 1964.

[36] T. Jurand, M. Kam, and R. Fischi, "Mathematical model of echoes in laser-based aerial bathymetric surveying," *Proc. 28th Conf. Decision and Control*, vol. 2, pp. 1779-1784, 1989.

[37] F. E. Hoge, C. W. Wright, W. B. Krabill, R. R. Buntzen, G. D. Gilbert, R. N. Swift, J. K. Yungel, and R. E. Berry, "Airborne lidar detection of subsurface oceanic scattering layers," *Appl. Optics*, vol. 27, pp. 3969-3977, Oct. 1988.

[38] J. F. Kaiser, "Nonrecursive digital filter design using the I_0-sinh window function," *Proc. 1974 IEEE Int. Symp. on Circuits and Systems*, San Francisco, pp. 20-23, April 1974.

[39] A. Antoniou, *Digital Filters: Analysis, Design, and Applications*, 2nd ed., McGraw-Hill, N.Y., 1993.

[40] J. P. Foley and J. G. Dorsey, "Equations for calculation of chromatographic figures of merit for ideal and skewed peaks," *Anal. Chem.*, vol. 55, no. 4, pp. 730-737, 1983.

[41] K. Levenberg, "A method for the solution of certain nonlinear problems in least squares," *J. Appl. Math.*, vol. 2, pp. 164-168, 1944.

[42] D. W. Marquardt, "An algorithm for least-squares estimation of nonlinear parameters," *J. SIAM*, vol. 11, no. 2, pp. 431-441, 1963.

[43] M. J. D. Powell, "Convergence properties of a class of minimization algorithms," *Nonlinear Programming*, vol. 2, O. L. Mangasarian, R. R. Meyor, and S. M. Robinson, eds., Academic Press, N.Y., pp. 1-27, 1975.

[44] M. R. Osborne, "Nonlinear least squares — the Levenberg algorithm revisited," *J. Austral. Math. Soc., Ser. B, Appl. math.*, vol. 19, pp. 343-357, 1976.

[45] J. J. Moŕe, "The Levenberg-Marquardt algorithm: implementation and theory," *Numerical Analysis*, G. A. Watson, ed., Lecture Notes in Math. vol. 630, Springer Verlag, Berlin, pp. 105-116, 1977.

[46] J. E. Dennis, Jr. and R. B. Schnabel, *Numerical Methods for Unconstrained Optimization and Nonlinear Equations*, Prentice-Hall, New Jersey, 1983.

[47] R. Fletcher, *Practical Methods for Optimization, Volume 1, Unconstrained Optimization*, Wiley, N.Y., 1980.

[48] M. J. D. Powell, "A hybrid method for nonlinear equations," *Numerical Methods for Nonlinear Algebraic Equations*, P. Rabinowitz, ed., Gordon and Breach, London, pp. 87-114, 1970.

[49] B. Billard, "Remote sensing of scattering coefficient for airborne laser hydrography," *Appl. Opt.*, vol. 25, no. 13, pp. 2099-2108, 1986.

[50] D. Hearn and M. P. Baker, *Computer Graphics*, Prentice-Hall, N.J., 1986.

[51] IBM, "Numerical surface techniques and contour map plotting," *International Business Machines, Data Processing Applications*, White Plains, N.Y., 1965.

[52] C. L. Lawson, "Generation of a triangular grid with application to contour plotting," JPL Sec. 914 Internal Tech. Memo. No. 299, 1972.

[53] E. R. Magnus, C. C. Joyce, and W. D. Scott, "A spiral procedure for selecting a triangular grid from random data," *J. Applied Mathematics and Physics*, vol. 34, pp. 231-235, 1983.

[54] D. F. Watson and G. M. Philip, "Systematic triangulations," *Computer Vision, Graphics and Image Processing*, vol. 26, pp. 217-223, 1984.

[55] S. W. Sloan, "A fast algorithm for constructing Delaunay triangulations in the plane," *Adv. Eng. Softw.*, vol. 9, no. 1, pp. 34-55, 1987.

[56] D. G. McKenna, "The inward spiral method: an improved TIN generation technique and data structure for land planning applications," *Proc. AUTOCARTO 8, Eighth Int. Sympo. Computer-Assisted Cartography*, Baltimore, M.D., pp. 670-679, 1987.

[57] C. L. Lawson, "Software for C^1 surface interpolation," *Mathematical Software III*, J. Rice, ed., Academic Press, N.Y., pp. 161-194, 1977.

[58] L. L. Schumaker, "Triangulation methods," *Topics in Multivariate Approximation*, C. K. Chui and L. L. Schumaker, eds., Academic Press, N.Y., 1987.

[59] M. J. McCullagh and C. G. Ross, "Delaunay triangulation of a random data set for isarithmic mapping," *Cartographic Journal*, vol 17, no. 2, pp. 93-99, 1980.

[60] R. Sibson, "Locally equiangular triangulations," *Computing Journal*, vol. 21, no. 3, pp. 243-245, 1978.

[61] G. Birkhoff and L. Mansfield, "Compatible triangular finite elements," *J. Mathematical Analysis and Applications*, vol. 47, no. 3, pp. 531-553, 1974.

[62] M. J. McCullagh, "Creation of smooth contours over irregularly distributed data using local surface patches," *Geographical Analysis*, vol 13, no. 1, pp. 51-63, 1981.

[63] R. W. Clough and J. L. Tocher, "Finite element stiffness matrices for analysis of plates in bending," *Proc. Matrix Methods in Struct. Mech.*, Air Force Inst. of Tech., Wright-Patterson A.F.B., Ohio, 1965.

[64] M. Zlámal, "On the finite element method," *Numer. Math*, vol. 12, pp. 394-409, 1968.

[65] A. Ženíšek, "Interpolation polynomials on the triangle," *Numer. Math*, vol. 15, pp. 283-296, 1970.

[66] H. Akima, "A method of bivariate interpolation and smooth surface fitting for irregularly distributed data points," *ACM Trans. Mathematical Software*, vol. 4, pp. 148-159, June 1978.

[67] H. Akima, "A method of bivariate interpolation and smooth surface fitting for values given at irregularly distributed points," OT Report 76-106, U.S. Govt. Printing Office, Washington, D.C., July 1976.

[68] A. C. Bovik, T. S. Huang, and D. C. Munson, Jr., "A generalization of median filtering using linear combinations of order statistics," *IEEE Trans. Acoust., Speech, and Signal Processing*, vol. ASSP-31, pp. 1342-1350, Dec. 1983.

[69] J. B. Bednar and T. L. Watt, "Alpha-trimmed means and their relationship to median filters," *IEEE Trans. Acoust., Speech, and Signal Processing*, vol. ASSP-32, pp. 145-153, Feb. 1984.

[70] S. G. Tyan, "Median filtering: deterministic properties," *Two-Dimensional Digital Signal Processing II: Transforms and Median Filters*, T. S. Huang, ed., Springer-Verlag, N.Y., 1981.

[71] B. I. Justusson, "Median filtering: statistical properties," *Two-Dimensional Digital Signal Processing II: Transforms and Median Filters*, T. S. Huang, ed., Springer-Verlag, N.Y., 1981.

[72] S. R. Peterson, Y. H. Lee, and S. A. Kassam, "Some statistical properties of alpha-trimmed mean and standard type M filters," *IEEE Trans. Acoust., Speech, and Signal Processing*, vol. ASSP-36, pp. 707-713, May 1988.

[73] B. J. L. Berry and D. F. Marble, *Spatial Analysis: A reader in Statistical Geographer*, Prentice-Hall, N.J., 1968.

[74] J. S. Lim, *Two-Dimensioanl Signal and Image Processing*, Prentice-Hall, N.J., 1990.

[75] D. E. Dudgeon and R. M. Mersereau, *Multidimensioanl Digital Signal Processing*, Prentice-Hall, N.J., 1984.

[76] W.-S. Lu and A. Antoniou, *Two-Dimensional Digital Filters*, Marcel Dekkar, N.Y., 1992.

[77] B. R. Hunt, "The application of constrained least squares estimation to image restoration by digital computer," *IEEE Trans. Computers*, vol. C-22, pp. 805-812, Sept. 1973.

[78] L. L. Scharf, *Statistical Signal Processing: Detection, Estimation, and Time Series Analysis*, Addision Wesley, Massachusetts, 1990.

[79] D. T. Kuan, A. A. Sawchuk, T. C. Strand, and P. Chavel, "Adaptive noise smoothing filter for images with signal-dependent noise," *IEEE Trans. Pattern Analysis and Machine Intelligence*, vol. PAMI-7, pp. 165-177, Mar. 1985.

[80] M. J. Casey, R. A. O'Neil, and P. Conrad, "The advent of LARSEN," *Proc. first Biennial Canadian Hydrographic Conf.*, pp. 7-12, Nova Scotia, 1985.

APPENDIX A-1
PSEUDO-CODE FOR THE DETECTION OF SURFACE PEAK

Let

loc_surface : location of surface peak
loc_bottom : location of bottom peak

loc_in1 : location where the first peak zone starts
loc_out1 : location where the first peak zone ends
loc_in2 : location where the second peak zone starts
loc_out2 : location where the second peak zone ends

in1 : the flag is set when *loc_in1* is determined
out1 : the flag is set when *loc_out1* is determined
in2 : the flag is set when *loc_in2* is determined
out2 : the flag is set when *loc_out2* is determined

loc_peak : location of the first peak found in the surface zone
loc_max1 : location of the maximum point in the first peak zone
loc_max2 : location of the maximum point in the second peak zone

big1 : current maximum amplitude found in the first peak zone
big2 : current maximum amplitude found in the second peak zone

$x[\cdot]$: independent variable of the waveform
$amp(x[\cdot])$: amplitude of the laser waveform

Remarks: *loc_in1* and *loc_out1* define the range of the first peak zone. *loc_in2* and *loc_out2* define the range of the second peak zone.

surface_detect()

For each waveform do

1. Initialize all location and amplitude parameters to zeros. Reset all flags.
2. For each of the data points in the surface zone do

   {Check location: Beginning of first peak zone}

   2.1 If (*in1* is not set and $amp(x[i]) >$ threshold)
      2.1.1 Assign this location to *loc_in1*.
      2.1.2 Set *in1*.

{Check location: End of first peak zone}

2.2 If (*in1* is set but *out1* is not set and *amp*(*x*[*i*]) < threshold)

2.2.1 Assign the previous location *x*[*i* - 1] to *loc_out1*.

2.2.2 Set *out1*.

{Check location: Beginning of the second peak zone}

2.3 If (*out1* is set but *in2* is not set and *amp*(*x*[*i*]) > threshold)

2.3.1 Assign this location to *loc_in2*.

2.3.2 Set *in2*.

{Check location: End of second peak zone}

2.4 If (*in2* is set but *out2* is not set and *amp*(*x*[*i*]) < threshold)

2.4.1 Assign the previous location *x*[*i* - 1] to *loc_out2*.

2.4.2 Set *out2*.

{Check location: First peak in the surface zone}

2.5 If (first peak is not located and *amp*(*x*[*i*]) > *amp*(*x*[*i* + 1]) and *amp*(*x*[*i* + 1]) > *amp*(*x*[*i* + 2]) and *amp*(*x*[*i* + 1]) > *amp*(*x*[*i* + 3]))

2.5.1 Retain current *i*.

2.5.2 Assign *x*[*i*] to the peak location *loc_peak*.

2.5.3 While (*amp*(*x*[*i* - 1]) = *amp*(*x*[*i*]))

2.5.3.1 Set *x*[*i* - 1] as the peak location *loc_peak*.

2.5.3.2 Decrease *i* by 1.

2.5.4 Restore current *i*.

2.5.5 Set flag indicating that the first peak has been located.

{Check location: Peak of maximum amplitude in the first peak zone}

2.6 If (*in1* is set but *out1* is not set and *amp*(*x*[*i*]) > *big1*)

2.6.1 Update *loc_max1* by assigning *x*[*i*] to it.

2.6.2 Update maximum amplitude *big1*.

{Check location: Peak of maximum amplitude in the secocnd peak zone}

2.7 If (*in2* is set but *out2* is not set and *amp*(*x*[*i*]) > *big2*)

2.7.1 Update *loc_max2* by assigning *x*[*i*] to it.

2.7.2 Update maximum amplitude *big2*.

END {for}

{Determine surface and bottom peak locations, if present}

3. If (*loc_peak* = *loc_max1*)
   3.1 Record *loc_surface* as *loc_peak*.

   else if (*in1* and *out1* are both set)
   3.2 If (*loc_in1* < *loc_peak* < *loc_out1*)
      3.2.1 Record *loc_surface* as *loc_peak*.
      3.2.2 Record *loc_bottom* as *loc_max1*.
      else
         Record *loc_surface* as *loc_max1*.

   else if (*in1* is set but *out1* is not set)
   3.3 If (*loc_peak* > *loc_in1*)
      3.3.1 Record *loc_surface* as *loc_peak*.
      3.3.2 Record *loc_bottom* as *loc_max1*.
      else
         Record *loc_surface* as *loc_max1*.

   else if (*in1* is never set)
   3.4 Record *loc_surface* as zero indicating that no surface reflection is present in the waveform.

4. If (*in2* and *out2* are both set)
   4.1 Record *loc_bottom* as *loc_max2*.

5. If (*in2* is set but *out2* is not set)
   5.1 If (*loc_max2* is not equal to the last location of the surface zone)
      5.1.1 Record *loc_bottom* as *loc_max2*.
      else
         Search for the bottom-peak location beyond the surface zone until the amplitude of the signal starts to decrease. Record that location as $x[tmp]$. Assign $x[tmp-1]$ to *loc_bottom*.

END {for}

APPENDIX A-2
PSEUDO-CODE FOR THE DETECTION OF BOTTOM PEAK

Let

loc_surface : location of surface peak
loc_bottom : location of bottom peak

loc_pos : location of a positive peak found in the differentiated waveform
loc_neg : location of a negative peak found in the differentiated waveform

max_neg : location of the maximum negative peak in the differentiated waveform
max_pos : location of the positive peak which corresponds to the maximum negative peak next to it in the differentiated waveform

loc_pos1 : location of positive peak found in the differentiated waveform if the first data in the search range is positive
loc_neg1 : location of negative peak found in the differentiated waveform if the first data in the search range is positive

loc_max : location of the maximum positive peak found in the differentiated waveform

surface : index *loc_surface*
pos1 : index *loc_pos1*
neg1 : index *loc_neg1*
max : index *loc_max*

rightmost : the rightmost location that has the same amplitude as the present location
leftmost : the leftmost location that has the same amplitude as the present location

bypass : the flag is set when the positive peak detected is not the desired one. This peak should be bypassed.

$x[\cdot]$: independent variable of the waveform
$diff(x[\cdot])$: amplitude of the differentiated waveform

bottom_detect_main()

For each waveform do

1. Read in *surface* from surface_detect().

2. If (surface reflection is detected in surface_detect())
   2.1 Read in the differentiated waveform *diff*.
   2.2 Call bottom_detect(*diff*, *surface*) and assign the returned value to *loc_bottom*.
   else
   Assign *loc_bottom* to zero.

END {for}

bottom_detect(*diff*, *surface*)

1. Initialize all location and amplitude parameters to zeros. Reset all flags.

2. Search for the location of the maximum positive peak in the differentiated waveform. Assign this location to *loc_max*.

{Search for a positive peak if first-searched data is positive}

3. If (*diff*(*x*[*surface*]) is positive)
   3.1 Update *surface* by adding 2 to it to give a correct starting point.
   3.2 Repeat

   3.2.1 If (*bypass* is set)
   3.2.1.1. Reset *bypass*.

   3.2.2 For each of the rest of the data points starting from *diff*(*x*[*surface*]) till the end of the differentiated waveform do
   3.2.2.1 If (*diff*(*x*[*i*]) is positive)
   {data is in the positive region}
   If (*diff*(*x*[*i*]) > *diff*(*x*[*i* -1]) and *diff*(*x*[*i* -1]) > *diff*(*x*[*i* -2]))
   Assign *i* to *pos1*.
   Assign *x*[*i*] to *loc_pos1*.
   Set flag indicating that a positive peak has been detected.
   else
   {data is in the negative region}
   If (a positive peak is detected and it is at least 2 samples before the end of the waveform)
   If (*diff*(*x*[*i*]) < *diff*(*x*[*i* +1]) and *diff*(*x*[*i* +1]) < *diff*(*x*[*i* +2]))
   Assign *i* to *neg1*.
   Assign *x*[*i*] to *loc_neg1*.
   End the for loop.
   else
   Assign *i* to *surface*.

End the for loop.

END {for}

3.2.3 If (positive peak is detected)
{Choose innermost locations}
3.2.3.1 Find rightmost of *loc_pos1*. Find leftmost of *loc_neg1*.
3.2.3.2 If (this positive peak is the maximum positive peak in the differentiated waveform)
Assign (*max*+1) to *surface*.
Set *bypass*.
Initialize location and amplitude parameters to zeros.
else
Record *loc_bottom* as (*loc_pos1* + *loc_neg1*)/2.
Set flag indicating that bottom peak has been detected.
End until (*bypass* is not set)

4. If (bottom peak is not detected)
4.1 Call bottom_search(*diff*, *surface*) and assign the returned value to *loc_bottom*.

bottom_search(*diff*, *surface*)

1. Initialize all location variables to zeros. Reset all flags.
2. For each of the data points in the bottom zone do
2.1 If (*diff*(*x*[*i*]) is positive)
2.1.1 If (*diff*(*x*[*i*]) > *diff*(*x*[*i*-1]) and *diff*(*x*[*i*-1]) > *diff*(*x*[*i*-2]))
2.1.1.1 Assign *x*[*i*] to *loc_pos*.
2.1.1.2 Set flag indicating that a postive peak has been detected.
2.2 If (positive peak is detected and negative peak is not detected and *diff*(*loc_pos*) > 1.0 and *diff*(*x*[*i*]) is negative)
2.2.1 If (*diff*(*x*[*i*]) < *diff*(*x*[*i*+1]) and *diff*(*x*[*i*+1]) < *diff*(*x*[*i*+2]))
2.2.1.1 Assign *x*[*i*] to *loc_neg*.
2.2.1.2 Set flag indicating that a negative peak has been detected.
2.3 If (both positive and negative peaks are detected)
{A bottom peak is present}
2.3.1 If (*diff*(*loc_neg*) < *diff*(max_*neg*))
{Choose innermost locations}
2.3.1.1 Find *leftmost* of *loc_neg*. Find rightmost of *loc_pos*.
2.3.1.2 Update *max_pos* and *max_neg*.
2.3.1.3 Reset all flags.
END {for}
3. Record *loc_bottom* as (*x*[*max_pos*] + *x*[*max_neg*])/2 and return this value.